Order Number 9325110

Investigation of the interfaces of silicon-silicon dioxide thin films and ball-milled tin-germanium (silicon) powders using x-ray techniques

Jayanetti, J. K. D. Sumedha, Ph.D.

City University of New York, 1993

U·M·I
300 N. Zeeb Rd.
Ann Arbor, MI 48106

INVESTIGATION OF THE INTERFACES OF SILICON-SILICON DIOXIDE THIN FILMS AND BALL-MILLED TIN-GERMANIUM (SILICON) POWDERS USING X-RAY TECHNIQUES

by

J.K.D. S. Jayanetti

A dissertation submitted to the Graduate Faculty in Physics in partial fulfillment of the requirements for the degree of Doctor of Philosophy, The City University of New York.

1993

Dedicated to

my parents

This manuscript has been read and accepted for the Graduate Faculty in Physics in satisfaction of the dissertation requirement for the degree of Doctor of Philosophy.

2/25/93
Date

Narciso Garcia
Chair of Examining Committee

3/2/93
Date

Joseph B. Krieger
Executive Officer

Arthur C. Damask

Steve M. Heald

Martin L. den Boer

Myron Strongin
Supervisory Committee

The City University of New York

Abstract

INVESTIGATION OF THE INTERFACES OF SILICON-SILICON DIOXIDE THIN FILMS AND BALL-MILLED TIN-GERMANIUM (SILICON) POWDERS USING X-RAY TECHNIQUES

by

J.K.D. S. Jayanetti

Advisor: Professor A. C. Damask

The Si/SiO_2 thin film interface and Sn/Ge(Si) interfaces in ball-milled Sn-Ge(Si) powders are investigated using x-ray reflectivity and EXAFS, respectively. X-ray reflectivity is used to compare the silicon dioxides grown on Si wafers, using conventional thermal oxidation and Plasma Enhanced Chemical Vapor Deposition (PECVD) processes. The aim was to determine the film morphology of PECV-deposited silicon dioxides, where a considerable decrease in deposition temperature is achieved. Macroscopic properties, such as film density, thickness, surface and interface roughness are probed. Analysis was carried out using several thermally grown and PECV-deposited oxides. Both techniques are found to produce silicon dioxides of good quality although the interface roughness of the PECV-deposited oxides was relatively higher. Sn K-edge EXAFS measurements were used to examine the Sn/Ge(Si) interface in ball-milled Sn-Ge(Si) powders. X-ray diffraction and Differential Scanning Calorimetry were also used as supporting techniques. Measurements made on samples of varying Sn concentrations showed systematic changes reflecting the fact that Sn appears in two different states, the metallic (β-Sn) phase, and a cubic SnGe(Si) alloy phase formed at the Sn/Ge(Si) interface. In the case

of the Sn-Ge system, where the Sn concentration is 20 vol.%, the alloy phase was dominant leaving essentially no Sn in the normal β-Sn phase. Alloying included several monolayers, and the bonding showed a strong covalent nature with stability above the bulk melting point of Sn. The results can be used to explain the previously observed reductions in melting enthalpy. Alloying at the Sn/Si interface is also strongly covalent, even though the reaction was less extensive. The thickness of the alloy phase is only about a monolayer. This difference was attributed to the higher lattice mismatch between Sn and Si.

ACKNOWLEDGEMENTS

I would like to express sincere gratitude to my mentor, Dr. Steve Heald, for his support throughout this work. Steve's professional approach and careful supervision of every aspect of this work provided me with a solid base in my research activities.

I thank Prof. A. Damask in his capacity as my advisor, for introducing me to the exciting research environment at Brookhaven, and also Prof. N. Garcia for the assistance he gave me as my graduate student advisor since I came to Queens, and for being the chair of my committee. I would also like to thank Dr. Myron Strongin and Dr. Marten den Boer, the other members of my thesis committee, for their direction.

Dr. C.K. Saw and his colleagues at Hoechst-Celanese assisted me with XRD measurements; Drs. S.S. Prasad, Durga Rani and T. Skotheim of Moltech helped me with glove box facilities; Dr. G.W. Rubloff and his colleagues of IBM provided the Si/SiO_2 thin film samples, and Bob Sabatini made TEM measurements. Their assistance was extremely beneficial to this work. I also acknowledge the various types of assistance I received from Drs. Ramesh Budhani, Jim McBreen, Bent Nielsen, Zhengquan Tan, Rick Barrera, Alison Davenport, Avril Woodhead, Heather Chen, Kumi Pandya, Gerry Lamble, Mark Ruckman and Don Dimarzio during this work. Over the past few years, the secretarial support I received from Maryann Larese; the technical support received from Larry Fareria and the rest of the technical staff in the Materials Science Division was invaluable. I appreciate their support very much. I will always remember the valuable assistance and discussions provided by Prasad, Rani, Tan, Rick, Kumi and Gerry.

Finally, I wish to express my gratitude to my wife Damayanthi for staying behind me patiently throughout this period, encouraging and helping me in every possible way, and to my parents who dedicated their lives for my well being.

This work is supported by the U.S.Department of Energy, Basic Energy Sciences, Division of Materials Sciences under contract Nos. DE-AS05-80-ER10742 and DE-AC02-76CH00016.

Contents

List of Tables

List of Figures

Chapter 1

Introduction

In this thesis, I discuss the application of x-ray reflectivity and x-ray absorption fine structure spectroscopy (EXAFS) to two interfaces of fundamental and applied interest, the Si/SiO_2 thin film interface and Sn/Ge(Si) interface of highly milled Sn-Ge(Si) powders. This chapter begins with a brief discussion about solid interfaces. Then, the interfaces of interest are discussed together with my objectives. The remaining chapters are divided as follows:

Chapter 2: Theoretical aspects of x-ray reflectivity and EXAFS

Chapter 3: Experimental details

Chapter 4: $Si-SiO_2$ system (Data analysis, results, and discussion)

Chapter 5: Sn-Ge System (Data analysis, results, and discussion)

Chapter 6: Sn-Si System (Data analysis, results, and discussion)

Chapter 7: Summary

1.1 Interfaces.

The importance of solid interfaces in recent developments in technology has made interfacial science an enormous area of study in both fundamental and applied research. Some of the most important properties of materials in high-technology applications are strongly influenced or controlled by the presence of these interfaces. In most of the cases, the fact that the properties at or near an interface differ dramatically from those of the bulk material, is the reason for the importance

associated with the interfaces. In magnetism, some interfaces have enhanced magnetic moments compared to the bulk, while in some cases the interface magnetic moment is lower than the bulk [1]. Some ultra-thin overlayers have magnetization perpendicular to the film. These interfacial magnetic effects are found to be very important in technical applications. For example, materials with perpendicular magnetic anisotropy are invaluable as high-density data-storage media. The entire electronic industry is based on the fascinating properties of semiconductor interfaces [2]. In bandgap engineering, semiconductor interfaces are exploited to obtain devices that have faster responses by carrier confinement. Thin film interfaces play a crucial role in VLSI metallization. Interfaces are the critical element in fiber-reinforced structural ceramics, conferring excellent mechanical properties. In surface modification techniques designed to enhance corrosion resistance or for catalytic applications, interfaces play an important role. The developments of deposition techniques, such as Molecular Beam Epitaxy (MBE), and Chemical Vapor Deposition (CVD) and substrate-cleaning methods, such as sputtering, and reactive ion etching are consequences of the need to use these interfacial properties effectively. To better understand these interfacial phenomenon, there are many analytical techniques which involve x-rays, electron microscopy, ion scattering, etc. The on-going research involves samples prepared in various forms, such as superlattices, thin films, and powders. Two of the interfaces which have been looked at recently are the Si/SiO_2 interface and the Sn/Ge interface of highly milled Sn-Ge powders. In this thesis, first x-ray reflectivity is used to study the interface of Si/SiO_2 system. The objective is to demonstrate the strength of x-ray reflectivity as a tool to extract information about the morphology of thin films or layered structures and to compare interfaces prepared by different oxidation methods. In the second study, the interesting physical and chemical

changes at the interfaces of Sn/Ge(Si) of highly milled Sn-Ge(Si) powders are investigated using EXAFS and x-ray diffraction.

1.2 Si/SiO_2 Interface

The Si/SiO_2 interface has drawn considerable scientific and technological interest during the past 10-20 years, due to its superior qualities in device applications. An important reason for the dominance of Si in the electronics industry is the quality of its oxide and the nature of the oxide/silicon interface. At the normal operating temperatures of the devices, the oxide is mechanically stable, electrically insulating, and chemically protective while the oxide/silicon interface is relatively smooth. These properties have made Si a dominant material in semiconductor device technology even though Ge and GaAs have superior inherent electrical properties.

The conventional technique of oxidation [3,4] of Si is thermal oxidation (furnace heating in an oxidizing atmosphere), where a polished, clean surface of a crystal of pure Si is exposed to oxygen at temperatures around 850-1100 °C at atmospheric pressure. Either 'dry' or 'wet' oxidation is used to control the rapidity of the oxide growth, which controls the thickness of the oxide film. For example, to form thick dielectric films one generally uses wet oxidation, that is, exposing the crystal surface to an oxidant gas containing water vapor. The quality of the film is maintained by controlling parameters such as layer thickness, stoichiometry, impurity content, density, adhesion, and dielectric properties.

However, recent research on these films has shown the necessity for further improving the growth techniques. For example, the high temperature involved in the oxidation process is found to induce lattice defects [3], such as stacking faults, which

are thought to arise from the thermal diffusion of silicon interstitials away from the oxide-silicon interface. These defects seriously affect the electrical properties of the devices. Lowering the oxidation temperature below 850° C causes enormous compressive stresses to develop in the oxide layer due to the large volume change on the oxidation. These stresses create point defects and dislocations in the Si substrates. Therefore, the growth temperature cannot be lowered further from this optimum temperature range without affecting the quality of the oxide layer.

To overcome the temperature effect, oxides have been grown using techniques such as thermal oxidation at high pressure [5] and deposition from the vapor phase [3]. Irene *et al.* [5] showed that good quality thermal oxides can be grown at lower temperature (800 °C) at high pressure (500 atm.). Vapor phase deposition can be accomplished at temperatures as low as 275-350 °C. Deposition from the vapor phase plays a more important role not only as a low temperature process, but also as to where the oxide layer is applied in the device. For example, when oxide layers are required at several places in a multi-level metallization scheme, especially between layers where there is no Si source, thermal oxidation has to be replaced by deposition from vapor phase. In addition, this method can be used to deposit silicon oxide on other semiconductors such as Ge and GaAs, which are at a disadvantage because of the inferior properties of their own oxides. The most popular vapor-phase deposition technique is chemical vapor deposition (CVD) [3].

The object of this study is to make a compare the properties of silicon dioxides grown on Si, using thermal oxidation and plasma enhanced chemical vapor deposition (PECVD), where an rf discharge supplies the additional energy required to promote the chemical reaction. Several workers have tried to grow oxides using the PECVD technique [6-8]. However, the first low temperature PECVD oxides with electrical

characteristics similar to those grown conventionally were reported by Batey and Tierney in 1986 [9]. The PECVD oxides characterized in this study were prepared using the process developed by Batey and Tierney.

The defect characteristics of these samples have been studied by the positron annihilation depth profiling technique [10]. The room temperature positron depth profiling measurements show that both types of oxides have similar defect characteristics [11,12]. However, upon annealing, the two oxides behave differently. Thermal oxides [11], when annealed at about 300 °C, show fewer open volume defects or trap sites at the interface: this is attributed to the passivation of interfacial trap sites by hydrogen diffusing from the oxide layer to the interface. Consequently, trap sites in the oxide layer become activated. The PECVD oxides [12] show increased defects, both at the interface and in the oxide layer upon annealing. This behavior is not clearly understood.

Our interest is to find out the important parameters such as density, thickness, surface roughness of the oxide films, and the roughness at the Si/SiO_2 interface using x-ray reflectivity. These parameters give a good measure of the quality of the film. Ellipsometry is a widely used tool to investigate the morphology of the thin films. However, this technique cannot measure the interface roughness in a straightforward fashion and the results have a higher uncertainty.

X-ray reflectivity has been increasingly used as a probe of the morphology of thin films and layered structures. Reflectivity is sensitive to the electronic density (or bulk density) distribution of a film normal to the surface. Therefore, with a multiparameter model involving density, and the thickness of each layer, these parameters can be determined with a relatively easy analysis. It is well suited to the measurement of interfacial roughness on subnanometer scale. Another key advantage is its

nondestructive nature. Therefore the measurements can be made either *ex situ* or *in situ* and can be used conveniently with the available synchrotron radiation facilities. Cowley and Ryan [13] first used x-ray reflectivity to characterize thin (1-10 nm) SiO_2 layers. The oxides examined in this study were grown to thicknesses ranging from 50-120 nm.

1.3 Sn/Ge(Si) Interface of Highly Milled Sn-Ge(Si) Powders.

The second part of this thesis includes investigations made on the Sn/Ge(Si) interfaces of highly milled Sn-Ge(Si) powders. The initial studies of the highly milled Sn/Ge system were made by Koch *et al.* [14] (1989) and Jang *et al.* [15] (1990), using Differential Scanning Calorimetry (DSC) and Transmission Electron Microscopy (TEM). They observed:

1. an apparent melting point depression of Sn [14], and
2. a compositional dependence of the enthalpy of fusion of Sn [15].

1.3.1 Melting point depression of metals.

Melting behavior of solids has been widely discussed for many years. Bulk metals are usually observed to melt at the melting point. However, there are instances where a depression of melting point was observed experimentally, which was thought to start from solid boundaries, such as surfaces and interfaces. The solid boundary initiated melting may have been the possible reason for the rare occurrence of superheating observed in solids. As a metal is heated, the fact that the boundaries of the metal melt before the bulk melting point would suppress superheating. There are several theories to interpret the melting behavior of solids, starting from the well

known Lindemann (1910) hypothesis, according to which melting is a vibrational instability released when the root-mean-square amplitude of vibrations reaches a critical fraction of the interatomic distance. Among other theories, Cotterill (1974) [16] emphasizes a catastrophic defect (dislocation) generation as the crucial factor, whereas Gorecky (1974) [17] suggests that metals melt when the equilibrium vacancy concentration reaches a critical value, followed by a sudden creation of a large number of vacancies, at the cost of latent heat. Boyer (1980) [18] concludes that a lattice shear instability is the precipitating feature for melting. Couchmann and Jesser [19] discuss the importance of heterogeneous nucleation of melting at the crystalline surface.

Several experimental studies made on metallic fine particles show that they melt at temperatures below the bulk melting temperature. Takagi (1954) [20] was the first to observe the phenomenon experimentally. Using electron diffraction and microscopic techniques, she studied the melting of thin, vacuum deposited layers of Sn, Pb and Bi. Since then, several studies have been performed on the melting of particles using *in situ* electron microscopy: i.e. Blackman and Curzon (1959) [21], and Wronsky (1967) [22] on Sn; Sambles (1971) [23], and Buffat and Borel (1976) [24] on Au; Berman and Curzon (1973) [25] on In; Peppiat (1973) [26], and Peppiat and Sambles (1975) [27] on Pb and Bi. All those studies show that the melting temperature decreases from the bulk melting point of the metal with decreasing particle size. The nucleation of melting on the surface is presumably responsible for the observed size-dependence of melting temperatures. In a more recent study made using DSC and x-ray diffraction, Willens *et al.* (1981) [28] observed the melting point depression of Pb in modulated Pb-Ge foils. As the Pb layer thickness decreased, the melting temperature was depressed and broadened. For a 20 Å thick Pb film, the start of the transition is 45°C

below the bulk melting temperature and the transition breadth is about 40 °C. The speculations are that the transition initiates at the Pb-Ge interface. Subsequently, Devaud & Willens (1986) [29] studied the melting behavior of 2 nm-thick Pb film sandwiched between two amorphous Ge films, using transmission electron microscopy (TEM). They concluded that the transition proceeds by a disordering mechanism rather than the formation of a liquid-solid interface. The disorder was nucleated at both Pb-Pb (grain boundaries) and Pb-Ge interfaces with the transition proceeding at a higher rate from the Pb-Pb grain boundaries. Franken and Van der veen [30] observed melting of single crystal Pb using ion scattering measurements. By monitoring the Pb (110) surface, they found the formation of a solid/liquid transition layer at the surface about 40 °C below the bulk melting point. As the temperature was further raised, the transition layer and the melt front progress towards the bulk.

The mechanically milled or ball milled Sn-Ge powders show some interesting results. Like Pb-Ge, Sn and Ge have negligible mutual solubilities in each other [31] and form a fine dispersion of the pure components through mechanical milling. This method is another alternative for obtaining a high interface/volume ratio as in modulated layered films. The observations made on Sn-Ge (50 at.% Sn) powders [14] milled for long times show a depression of the melting point of Sn. Melting is observed to begin as low as 36 °C below the equilibrium bulk melting temperature (the melting point of bulk tetragonal Sn is 231.9 °C). The depression of the melting point of Sn and broadening in the transition region increases with increasing milling time (decreasing particle size), reaching a saturation value after about 16 hours. Koch *et al.* [14] concluded that a vibrational mechanism induced at the Sn/Ge interface is the major contributor to this melting behavior.

In the present study, one experiment was designed to see whether the melting

transition of Sn begins at the Sn/Ge interface, using the modulated Sn/Ge and Sn/Al films. X-ray reflectivity at glancing angle geometry gives strong reflected Bragg peaks from modulated thin films. If the melting transition begins from the Sn/Ge interface, changes in the reflected Bragg peak can be monitored as the melting front proceeds toward the bulk of the film. However, the results were inconclusive due to difficulties encountered during the experiments. Ge in the Sn-Ge multilayers crystallized during heating, before reaching the range where the transition was expected, making the interface rougher. The Sn/Al multilayers deposited, were not good enough to produce satisfactory reflectivity data. However, the subsequent experiments made to understand the compositional dependence of the enthalpy of fusion of Sn lead us to interpret the apparent depression in melting point of Sn as a particle size dependent effect.

1.3.2 Melting enthalpy of Sn in the highly milled Sn-Ge powders.

DSC studies of Sn-Ge powders of different compositions, milled for a constant time (about 32 hours) show a change in the melting enthalpy of fusion of Sn. As the Ge concentration was increased, both the melting point and the enthalpy of fusion of Sn decreased. When the Ge concentration was increased above approximately 80 vol.%, the enthalpy of fusion essentially vanished. Jang *et al.* [15] concluded that, at this concentration, Sn was entirely in a disordered state adjacent to the Ge particles (milling makes the structure of crystalline Sn become more liquid like), such that no melting transition was observed. Later, Turnbull *et al.* [32] provided a model for this behavior supposing that Sn in these powders was distributed between an interfacial and bulk state. The interfacial state is one in which the Sn is assumed to be in a disordered

structure coating the Ge particles uniformly to a constant thickness of about one monolayer.

The approach here is to look at this interfacial Sn state from the structural point of view. The fact that the interfacial or free surface layers act differently from the bulk solids led us to look at this behavior in detail. It is known [33] that small amounts of Ge can stabilize the cubic phase of Sn, α-Sn, which normally transforms to the metallic phase at -13.2 °C, at temperatures above room temperature. Recent literature also reports the existence of α-SnGe alloys grown using molecular beam epitaxy on substrates such as Ge, CdTe, and InSb. Hochst *et al.* [34] grew α-SnGe alloys epitaxially on Ge(100) substrates at temperatures of about 400 °C. Our investigation describes results obtained about the Sn/Ge interfaces using EXAFS measurements. EXAFS is a proven tool to study disordered materials because of its ability to investigate the local atomic structure of each of the components in a material. X-ray diffraction and differential scanning calorimetry have also been used to support the results. This study shows that the previously assumed (by Turnbull *et al.*) interfacial Sn form exists as a cubic-SnGe alloy of several monolayers thick, at the Sn/Ge interface. Unlike conventional mechanical alloying, milling causes the ductile Sn to coat the brittle Ge particles. The resulting mixing of Sn and Ge at the interface gives rise to alloying. The stability of this alloy above the bulk melting point of Sn explains the reduction of melting enthalpy of Sn with decreasing Sn concentration. Similar alloying is observed when the milling process is applied to the Sn-Si system although the reaction is less extensive, possibly due to the larger lattice mismatch between Sn and Si. α-Sn has a band structure with a direct band gap of zero, similar to HgTe. Therefore, current research in the frontier involves, manipulation of α-Sn and another semiconductor appropriately to synthesize alloys,

quantum wells or a superlattice for technical applications [35-40]. This work provides the possibility of producing large quantities of SnGe alloy which previously could only be stabilized in thin epitaxially grown layers. The thesis concludes with a note on the application of the ball-milling method for producing other types of metal-coated particles which may be useful in catalytic applications.

Chapter 2

Theoretical

In this chapter, theoretical aspects of the two major techniques, x-ray reflectivity and EXAFS are discussed. The relevant theoretical formalism involved in x-ray diffraction etc. is discussed where necessary in the remaining chapters.

2.1 X-ray Reflectivity

2.1.1 Optical constants for x-rays and the Fresnel equation

The refractive index for x-rays can be written in the form:

$$n = 1 - \delta - i\beta \qquad (2.1)$$

where, δ and β are positive ($n < 1$). In terms of the atomic scattering factor f, the refractive index n can be written as:

$$n = 1 - 2\pi N r_e \frac{hc^2}{E} \sum \frac{\rho_j}{A_j} f_j \qquad (2.2)$$

where $r_e = e^2/m_e c^2$, is the classical electron radius, and $E = hw$, is the x-ray energy. N is the atomic number density, ρ is the mass density, A is the atomic mass, and m is the number of atomic species in the material. If f is written as $f = f' + if''$ then:

$$\delta = 2\pi N r_e \frac{hc^2}{E} \sum \frac{\rho_j}{A_j} f_j' \qquad (2.3)$$

$$\beta = 2\pi N r_e \frac{hc^2}{E} \sum \frac{\rho_j}{A_j} f_j'' \qquad (2.4)$$

with δ and β are also related by Kramers-Kronig relations given by:

$$\delta(\omega) = \frac{2}{\pi \omega_0^2} \int \frac{\omega^2 \beta(\omega)}{\omega_0^2 - \omega^2} \delta\omega \qquad (2.5)$$

The equations (2.3) and (2.4) are related to the x-ray reflectivity, for x-rays incident on a smooth surface at an angle θ, by the Fresnel equation [41] i.e:

$$R = \frac{I_R}{I} = \frac{h - (\theta/\theta_c)\,[2\,(h-1)\,]^{1/2}}{h + (\theta/\theta_c)\,[2\,(h-1)\,]^{1/2}} \qquad (2.6)$$

where

$$h = (\theta/\theta_c)^2 + \left([\,(\theta/\theta_c)^2 - 1\,]^2 + (\beta/\delta)^2 \right)^{1/2}$$

and θ_c is the critical angle below which the total external reflection occurs. For multiple interfaces this equation can be recursively applied with the boundary condition that the amplitude of the reflected ray from the semi-infinite bottom layer is zero. Then the reflectivity for n layers given by:

$$R_{n-1,n} = a_{n-1}^4 \cdot \frac{R_{n,n+1} + F_{n-1,n}}{1 + R_{n,n+1} F_{n-1,n}} \qquad (2.7)$$

where a_n is related to the phase of x-rays when traveling through layer n:

$$a_n = e^{-i\pi f_n d_n/\lambda}$$

and

$$F_{n-1} = \frac{f_{n-1} - f_n}{f_{n-1} + f_n}$$

When x-rays are incident on such interfaces, one can observe the total external reflection below θ_c, followed by modulations in the intensity for angles greater than θ_c due to the interference between the beam reflected from the boundaries. Parrett in 1954 [41] demonstrated that this phenomenon can be applied to thin films or layered structures to determine their morphology. The amplitude of the intensity modulations of a real interface are governed by the interface quality referred to as the roughness. Therefore, the Fresnel equations are modified by a term which accounts for the interface roughness.

In this case, the interface roughness is treated by assuming that the probability of finding a point on the interface at a particular value z is Gaussian [42-44] i.e:

$$W(z) = \frac{1}{\sqrt{2\pi\sigma^2}} . \exp\left[(z-z_0)^2/2\sigma^2\right] \qquad (2.8)$$

with the Fresnel equation modified by terms:

$$R_{n-1,n} = R_{n-1,n} e^{-8(\pi\sigma_n \sin\theta/\lambda)^2}$$

and

$$F_{n-1,n} = F_{n-1,n} e^{-2 f_{n-1} f_n \sigma_n^2}$$

where σ_n is the root mean square roughness of the nth layer.

The resulting set of equations can be solved using the matrix formalism described by Vidal and Vincent [45]. The model assumes that the roughness parameter is much less than the layer thickness and that the roughnesses of the interfaces are uncorrelated. When the roughness is large ($\sigma > 50$ Å), the corresponding interface can be treated as a succession of thin layers with gradually varying density.

2.1.2 X-ray reflectivity from Si-SiO_2 films

Figure 2.1 shows model calculations for a 500 Å SiO_2 layer on a Si substrate. The sensitivity of the density, surface, and interface roughnesses on reflectivity is illustrated. For no roughness, large angle data has a $(\theta/\theta_c)^{-4}$ dependence. The effect of interface roughness is illustrated using Figure 2.1 (b) where the factor $(\theta/\theta_c)^{-4}$ has been removed to bring out the interface details. The figure shows that the surface roughness changes the overall slope of the reflectivity curve, while the interface roughness controls the q-dependence of the amplitude of the modulations at a given density. The morphology of a thin film can be obtained by comparing the experimental reflectivity data with the model.

2.1.3 X-ray reflectivity from Sn-Ge multilayers

The theory suggests that when applied to a periodic layered structure, such as a multilayer the x-ray reflectivity will show intense Bragg peaks. Figure 2.2 shows model calculations made for a Sn/Ge (50 Å/50 Å) multilayer. The Bragg peaks are the result of the interference of reflected beams from dissimilar interfaces. When the

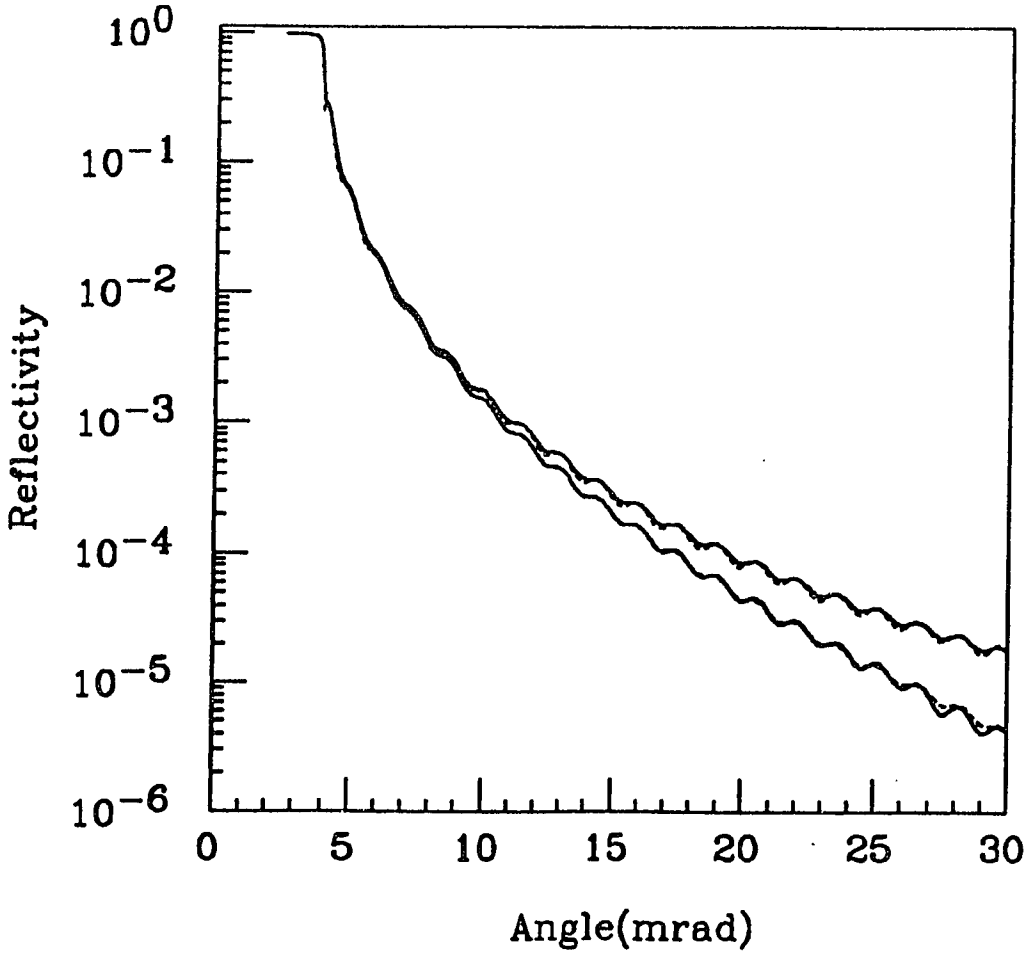

Figure 2.1: (a) Calculated reflectivity curves for 500 Å SiO_2 on Si. The two upper curves are for no roughness and for SiO_2 densities of 2.26 g/cm^3 (solid line) and for 2.22 g/cm^3 (dashed line). The two lower curves are for a density of 2.26 g/cm^3 with a surface roughness of 5.0 Å and interface roughness of 0 (solid line) and 5.0 Å (dashed line).

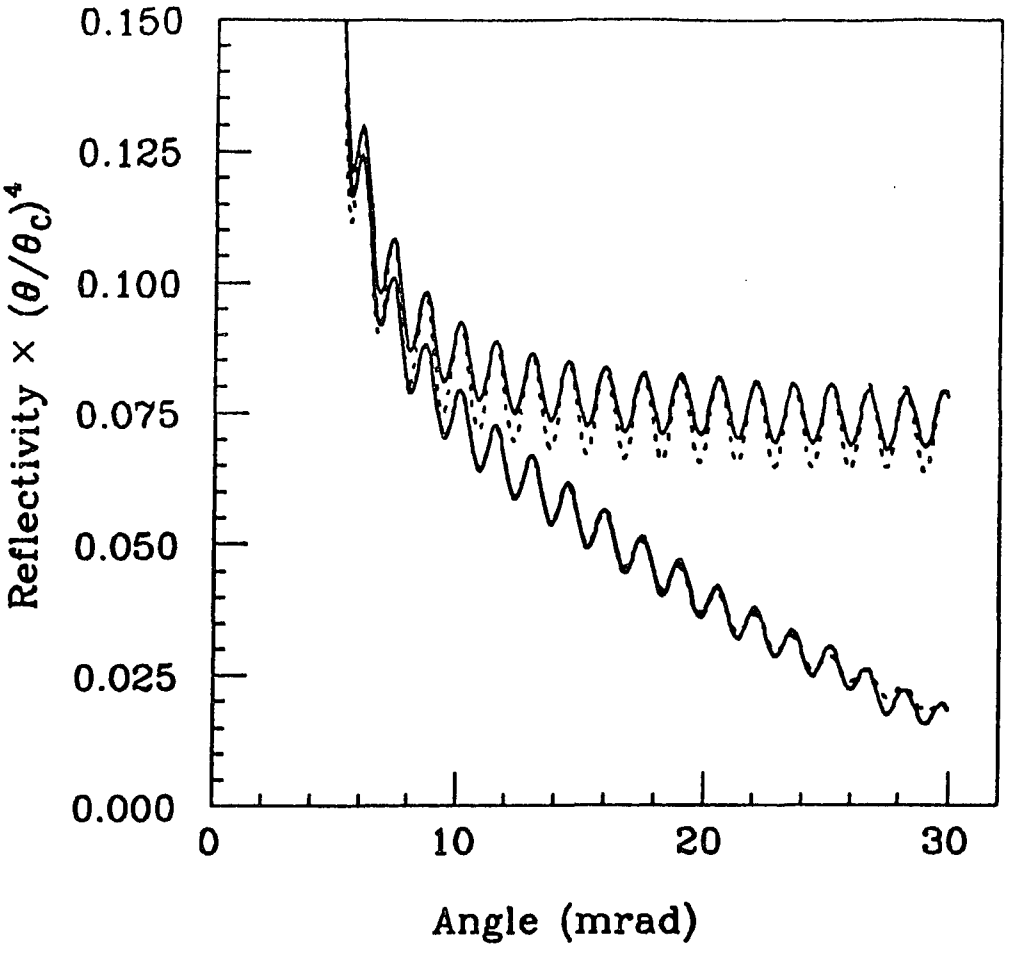

Figure 2.1: (b) The reflectivity curves in figure 2.1 (a), with a factor $(\theta/\theta_c)^4$ removed for clarity.

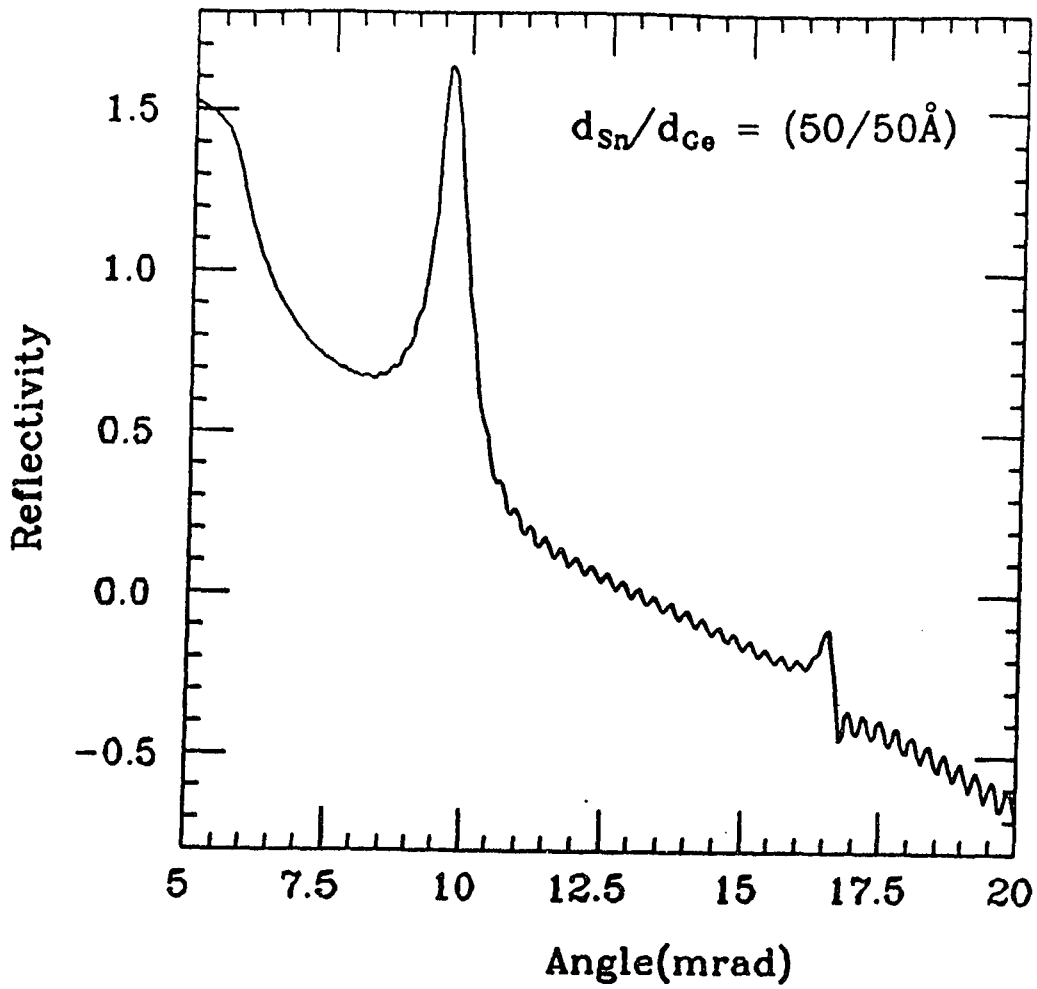

Figure 2.2: (a) Theoretical calculations at 8 keV, showing the log reflectivity vs angle for a Sn/Ge (50 Å/50 Å) multilayer (25 layers with a roughness of 10 Å).

phase difference of reflected beams from one set of interfaces (Sn/Ge) is equal to that of the other set of interfaces (Ge/Sn), the even ordered Bragg peaks vanish. The change in thickness of one set of layers with respect to the other would cause the even ordered peaks to evolve as shown in Figure 2.2(b). The change in thickness also causes an angular shift in the Bragg peaks which is less sensitive. The evolution of peaks makes the reflectivity method feasible to study whether the initiation of melting begins from the interface for a material (Sn in this case), which undergoes a detectable volume change during melting.

2.1.4 Accuracy of results

The accuracy of results obtained from the reflectivity depends on the number of parameters used in the theoretical model and the range of the data. The surface roughness, thickness and density of the film relative to the substrate can be determined with a high degree of accuracy. The accuracy of the interfacial information depends on the way it is treated in modelling. Even though more layers of gradually varying density may take the model closer to the actual interface, the associated large number of parameters may increase the uncertainty of the results. In general, the simplest model gives the most accurate results. SiO_2/Si films usually have atomically sharper interfaces and the density of the Si substrate is already known. Therefore, in most cases, a two-layer model is sufficient to approximate the actual case and the results have a very high accuracy.

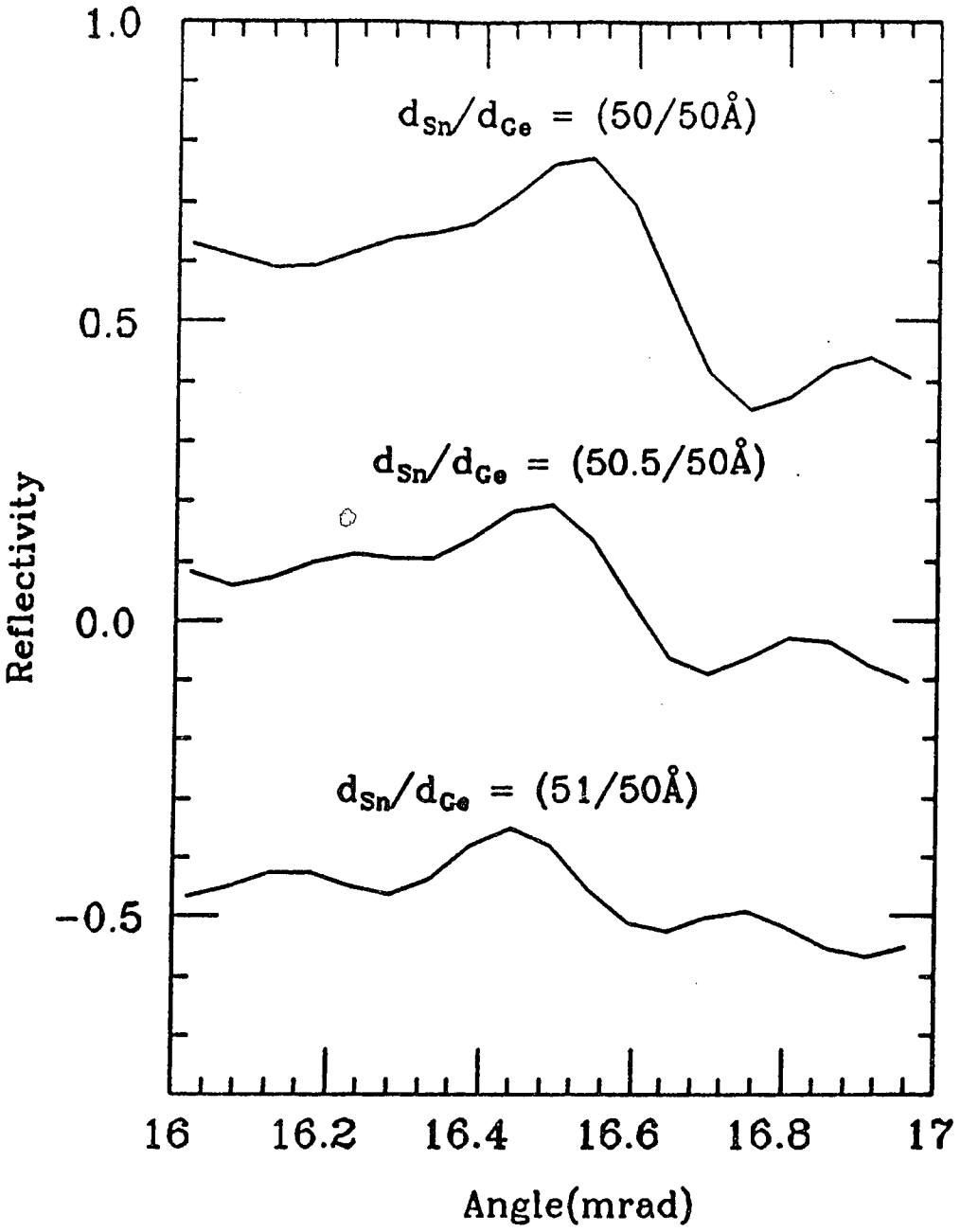

Figure 2.2: (b) The intensity variation of the 2nd order Bragg peak as Sn goes through the melting transition.

2.2 X-ray Absorption Spectroscopy

The absorption of x-rays by atoms varies smoothly with the photon energy except at some discrete energies where abrupt increases occur. These are called the absorption edges and correspond to the x-ray photon attaining enough energy to excite additional occupied electron levels in the atom. However, for condensed matter, the absorption of x-rays on the high energy side of the edges does not vary monotonically, but shows a rather complicated behavior, which is governed by the atomic environment around the absorbing atom. After an absorption event, the resulting photoelectron will scatter from the neighboring atoms. The scattered part of the electron's wave function interferes with the outgoing part, and the phase of the interference varies with the electron's (and hence, photon's) energy, giving rise to an energy dependent absorption spectrum with oscillatory behavior. The features occurring within a few tens of eV of the edge are commonly referred to as the x-ray absorption near edge structure (XANES). In the XANES region, photoelectrons have such a low kinetic energy and long mean free paths that they can experience multiple scattering in addition to single scattering. The information one can obtain from the XANES include bonding geometry, valence state of the absorbing atom, and partial unoccupied density of states.

2.2.1 X-ray absorption fine structure (EXAFS)

EXAFS refers to the oscillations extending from about 30 eV above the edge up to as much as $\sim$1000 eV. The multiple scattering events make a negligible contribution to the EXAFS from the first near neighbors, and in most cases, one can obtain the structural information of a material through an analysis of the first near

neighbor region. In the EXAFS region, the interference function χ(k) can be written as:

$$\chi(k) = \frac{\mu(k) - \mu_0(k)}{\mu_0(k)} \qquad (2.9)$$

where μ_0(k) is the smoothly varying part of the absorption due to all absorption processes, μ(k) is the total absorption due to a core level electron, and k, the photoelectron wave vector, is related to the energy E of the incident photon by $k=[2m(E-E_0)/h^2]^{1/2}$, where m is the electron mass and E_0 is the threshold energy.

2.2.2 EXAFS Equation

Application of this interference function to determine the structural parameters was first demonstrated by Sayers *et al.*[46]. The structural parameters include the type and number of near neighbor atoms (coordination number), near neighbor distance, and the mean-squared relative displacement with respect to an absorbing atom. The corresponding EXAFS interference function stated in terms of the structural parameters is based on a single scattering theory, assuming that the curvature of the outgoing wave can be neglected compared to the dimensions of the scatterer (plane wave or small atom approximation). The subsequent theoretical development involves not only the improved single-scattering formalism [47-51], but also formulations that take into account the spherical wave nature of the photoelectron and multiple scattering. Recently, Mustre *et al.* [52] introduced an interesting formalism (FEFF theoretical code,Version 5), based on the spherical wave nature of the photoelectron and multiple scattering. This formalism can represent EXAFS data accurately, even

up to third or fourth near neighbors and is practically very useful for data analysis. It also shows the importance of multiple scattering contributions when analyzing the higher order near neighbors.

However, in many cases, the EXAFS analysis is limited up to the first near neighbor shell where multiple scattering is not important and comparison with standards can produce accurate results using the single scattering theory. The objective here is to discuss the theoretical formalism of EXAFS based on the single scattering model. In the single scattering approximation, the EXAFS equation for absorption at K or L_I edge is given by:

$$\chi(k) = -\sum \frac{N_j}{kR_j^2} S_0^2(k)\, e^{-2k^2\sigma_j^2} e^{-2R_j/\lambda} \sin[2kR_j + \delta_j(k)] \quad (2.10$$

Equation (2.10) is a result of application of the Fermi's Golden Rule to a single electron associated with an absorber, backscattered singly by a scatterer, expanded with approximations to an actual system which contains a large number of absorbers, scatterers, and the intervening medium [53,54]. Let us discuss each of those terms in equation (2.10) briefly, with the associated assumptions and approximations.

The atomic environment around an absorber can be divided into well defined coordination shells depending on the average distance from the absorber to the scatterer and its type. (The normal criterion [53] for considering that atoms are in different shells is that they are separated well enough so that their transforms in R-space (radial distance from the absorber) show clearly separated peaks. In practice, this criterion means that atoms more than about 0.6 Å apart are considered to be in separate shells.) The total EXAFS contribution is obtained by adding the contributions

from the atoms of each shell. In equation (2.10), summation is over the coordination shells of atoms surrounding the absorbing atom with N_j atoms in shell j situated at an average distance R_j from the central atom. As the photoelectron wave travels to the scatterer and back to the absorber, the amplitude is reduced by a factor $1/R^2$. The argument in the sine represents the resulting total phase difference. Both the path difference ($2kR_j$ term) and the phase shift ($\delta_j(k)$ term) due to the varying potential between the absorber and scatterer contribute to the total phase difference.

$F_j(k)$, the backscattering amplitude, is a term characteristic of the scatterer. Calculations done for a wide range of atoms show, in general that F(k) peaks at low k and falls off roughly as $1/k^2$ at higher values of k, while the overall magnitude at high k increases with the atomic number of the scatterer. For heavier atoms, a resonance similar to the Ramsauer-Townsend effect [55] causes a dip in F(k). As a result, F(k) tends to have a double-peaked or triple-peaked structure for heavier atoms. Figure 2.3 illustrates the behavior of $F_j(k)$ for Sn and Ge, where a dip is observed for Sn near 7 $Å^{-1}$.

2.2.2 (a) Manybody effects

The terms S_0^2 and $e^{-2R/\lambda}$ account for the many body effects occurring in an actual system. As the photoelectron (the 'active' electron) is excited from the core hole, the remaining electrons in the excited atom see a different Coulombic potential. Consequently, there is a probability that the remaining electrons also can be excited. These relaxed electrons (the 'passive' electrons) have different states compared to their initial states. Thus, relaxation effects alter the EXAFS amplitude by a factor, S_0^2, known as the many electron correction factor. Passive electron relaxation depends on the photoelectron energy. As a function of photon energy, S_0^2 is expected to

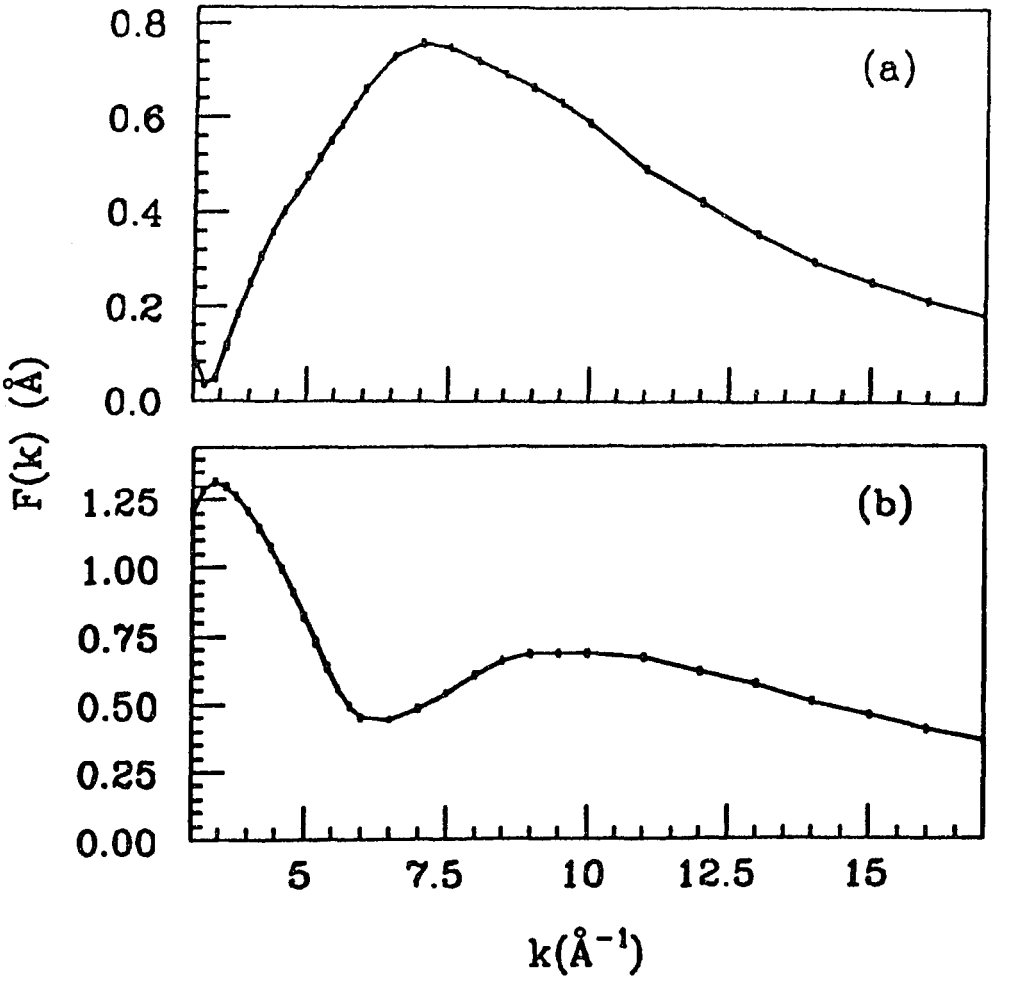

Figure 2.3: Backscattering amplitude F(k) for (a) Ge and (b) Sn calculated using FEFF (Version 4.08).

asymptotically approach a constant value less than one. In practice, S_0^2 is often approximated by a constant value obtained by fitting to a material of known structural parameters.

The inelastic losses, such as scattering by other electrons, phonons, and plasmons determine the lifetime of the photoelectron. In addition, the hole left behind by the photoelectron can be filled by another electron in the atom before the backscattered electron reaches the hole. Both events affect the coherency between the initial and final states. A mean free path term λ, gives the average distance an excited electron travels before losing coherence with its initial state. λ is related to the electron mean free path λ_e and equivalent hole mean free path λ_h, by:

$$\frac{1}{\lambda} = \frac{1}{\lambda_e} + \frac{1}{\lambda_h} \qquad (2.11)$$

The term $\exp[-2R/\lambda]$ term has been phenomenologically added to the EXAFS equation.

2.2.2 (b) Thermal vibrations and structural disorder

In any coordination shell, the atoms will not be at the same distance because of thermal vibrations and structural disorder, which affects the EXAFS amplitude and phase. The $\exp[-2k^2\sigma_j^2]$ term, in the equation (2.10) is a Debye-Waller type term representing the averaged effects of thermal vibrational and structural disorders, where a Gaussian disorder is assumed and σ^2 is the root mean square displacement of atoms from the average distance. The pair distribution function g(r) is used for averaging. (see, equation 2.12.)

$$\chi_j(k) = \int dr g(r) \frac{e^{-2r/\lambda}}{r^2} \sin[2kr + \delta_j(k)] \qquad (2.12)$$

The net distribution is a convolution of the structural and thermal displacements which can also be expanded in terms of cumulants. Normally, the distribution function has a Gaussian symmetry where only the first two cumulants are sufficient. The first cumulant term being zero (the phase dependent term), only the second term (amplitude modification term) contributes to the equation. However, for non-Gaussian disorders, the higher order cumulants should be considered and corrections are necessary for both phase and amplitude.

To summarize, equation (2.10) was formulated taking most of the inelastic losses into account, in a system which undergoes absorption of x-rays, and can be applied to systems with harmonic thermal vibrations and small, symmetric static disorders. Using a reliable data analysis method and reference compounds (standards), equation (2.10) can give accurate structural information.

2.2.3 Accuracy of results

The accuracy of structural parameters extracted from EXAFS depends on many factors. Particularly important are the number parameters being determined, the amount of disorder, the range of the data, and the quality of the reference data. In the simplest case where there is a single isolated shell, one may be able to determine the change in interatomic distance due to temperature effects etc., to within a few thousandths of an angstrom, and to obtain a mean square displacement to within a few percent of σ^2. On the other hand, when several shells must be fit simultaneously with

a limited data range the results are less accurate.

In general, the interatomic distance for the first near neighbor shell can be determined with an accuracy of 1%. The coordination numbers are less accurate, due to their correlation with the σ^2. Typical accuracies are 15% for the coordination number, and 20 % for absolute σ with better accuracies for changes in σ^2.[54]

Chapter 3

Experimental

The x-ray measurements for this work were done at beamlines X-11 A & B, at the synchrotron radiation facility, NSLS (National Synchrotron Light Source), at Brookhaven National Laboratory.

3.1 Synchrotron X-ray Beamlines

A typical synchrotron radiation storage ring consists of an orbital ring where electrons are accelerated by bending magnets. A beamline is a large mechanical setup which carries radiation generated by the accelerated electrons to an experimental station, which is a properly shielded space normally located at the end of a beam line also known as the experimental hutch. A modern storage ring consists of a number of beamlines tangentially coupled to beamports (sources), where radiation is produced. The x-ray beam of the experimenter's interest is obtained by using the components, the x-ray optics, associated with the beamline.

The basic mechanism of every beamline is similar, even though there are differences depending on the designer's interest and the energy range etc. The major components involved in the X-11A beamline setup [56] are schematically illustrated by Figure 3.1. The slit S_1 is centered on the beam to maximize the beam intensity, by adjusting its overall vertical height, before entering the monochromator. The slit separation can be optimized to attain a good resolution depending on the wavelength (energy), while a good intensity is also maintained. The monochromator, using the Bragg diffraction condition, selects x-rays of the required energy. The X-11A monochromator consists of two different crystal geometries. One configuration

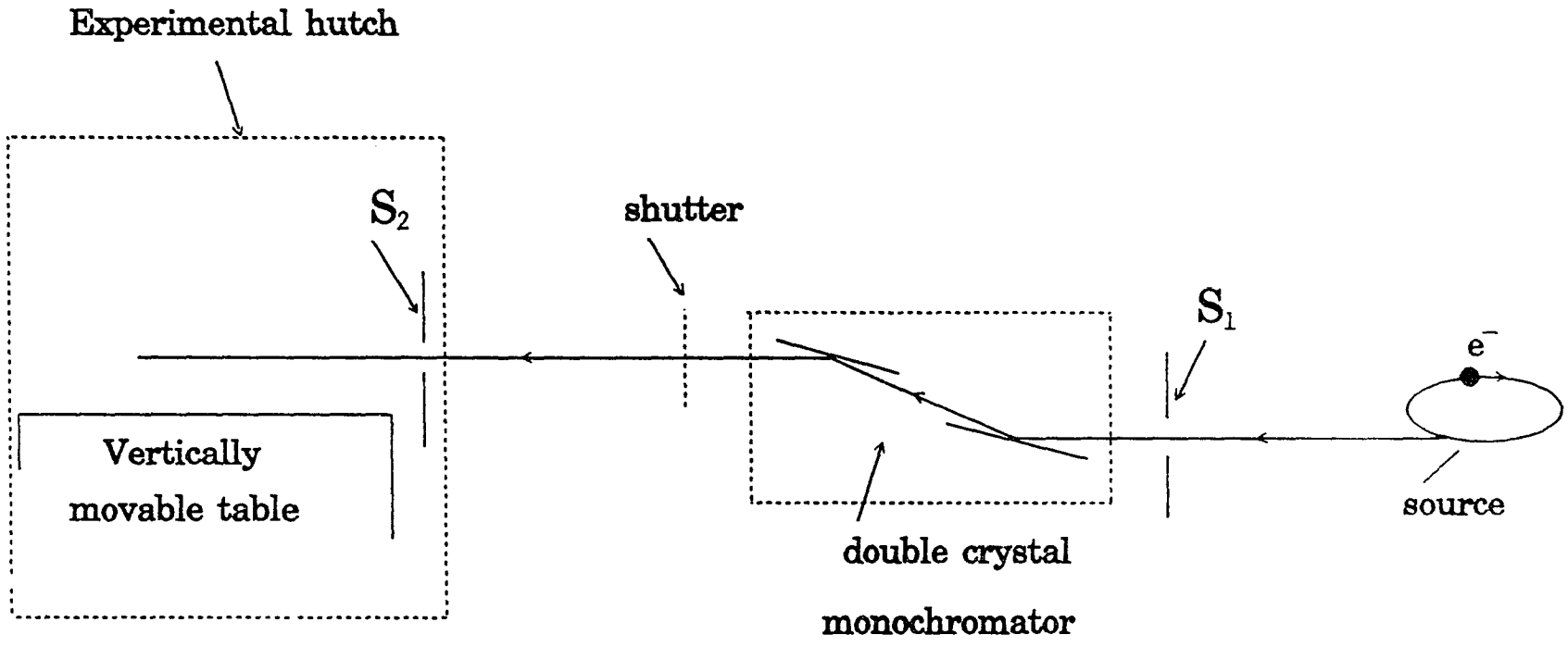

Figure 3.1: Schematic diagram involving the major components of the X-11A, x-ray beam line at the NSLS.

(nondispersive configuration [57]) has two crystals parallel to each other with both rotating. In this case, rotation of the monochromator causes a vertical beam offset. Therefore, during an experiment the offset is compensated by moving the experimental table vertically, according to the energy. The second configuration, not used in this work, involves four crystals (dispersive, nondeviating configuration) with two parallel pairs rotating in opposite directions, to maintain a zero beam offset. The type of monochromator crystals are selected according to the resolution and energy range needed. The user also has the option of detuning the crystals to reduce higher harmonics which are the multiples of the fundamental wave length which are passed by the monochromator. By detuning, (rotating one crystal slightly with respect to the other to break parallelism) higher harmonics can be rejected, because the crystal rocking curves for higher harmonics are narrower. The monochromatized beam then enters the experimental hutch through the slit S_2 (hutch slit). The hutch slit is used to control the beam size as required by the nature of the sample. The sample mounting stages and detection instrumentation in the experimental hutch can be changed depending on the type of the experiment. The X-11 beamlines are sufficiently equipped with detectors, computerized experiment-controlling facilities, and user friendly data acquisition methods for most EXAFS experiments. One can also perform experiments such as x-ray reflectivity, x-ray diffraction or scattering with the experimental instruments designed appropriately for use in the experimental hutch.

3.2 X-ray Reflectivity Measurements

The reflectivity of a thin film is simply the ratio of the intensity of the beam specularly reflected off the sample to the intensity of the incident beam, as a function of the incident angle. The measurement at the required energy (at a fixed monochromator angle), is made by rotating the sample and the reflected beam detector so that they maintain a θ:2θ ratio, where θ is the incident angle. However, the experiment should be carefully designed to measure only the incident and reflected beams by minimizing the scattered background radiation going into the detectors. The sample alignment is also crucial to obtain accurate data. First, I discuss the design and assembly of a two circle goniometer to make the x-ray reflectivity and diffraction measurements.

Figure 3.2 shows the configuration and the schematic diagram of the experimental setup for reflectivity measurements. The goniometer (Huber 424 two-circle model) consists of a fixed arm and an arm (detector arm) rotating about the center of the goniometer base on which the sample platform, a polished aluminum block or a temperature controlled copper holder, is mounted. The sample platform can also be rotated about the same center of rotation after a proper alignment (see the alignment procedure in appendix). Both rotations are motor driven with 200 steps/deg stepper motors. The step sizes can be decreased by coupling the motors with appropriate gear reducers or by program-controlled micro-stepping. The goniometer is mounted on the hutch table so that the plane of rotation of the sample and detector arm is vertical and parallel to the x-ray beam. The sample platform can be moved up and down perpendicular to the incident beam so that the center of rotation of the sample surface coincides with the center of rotation of the base irrespective of

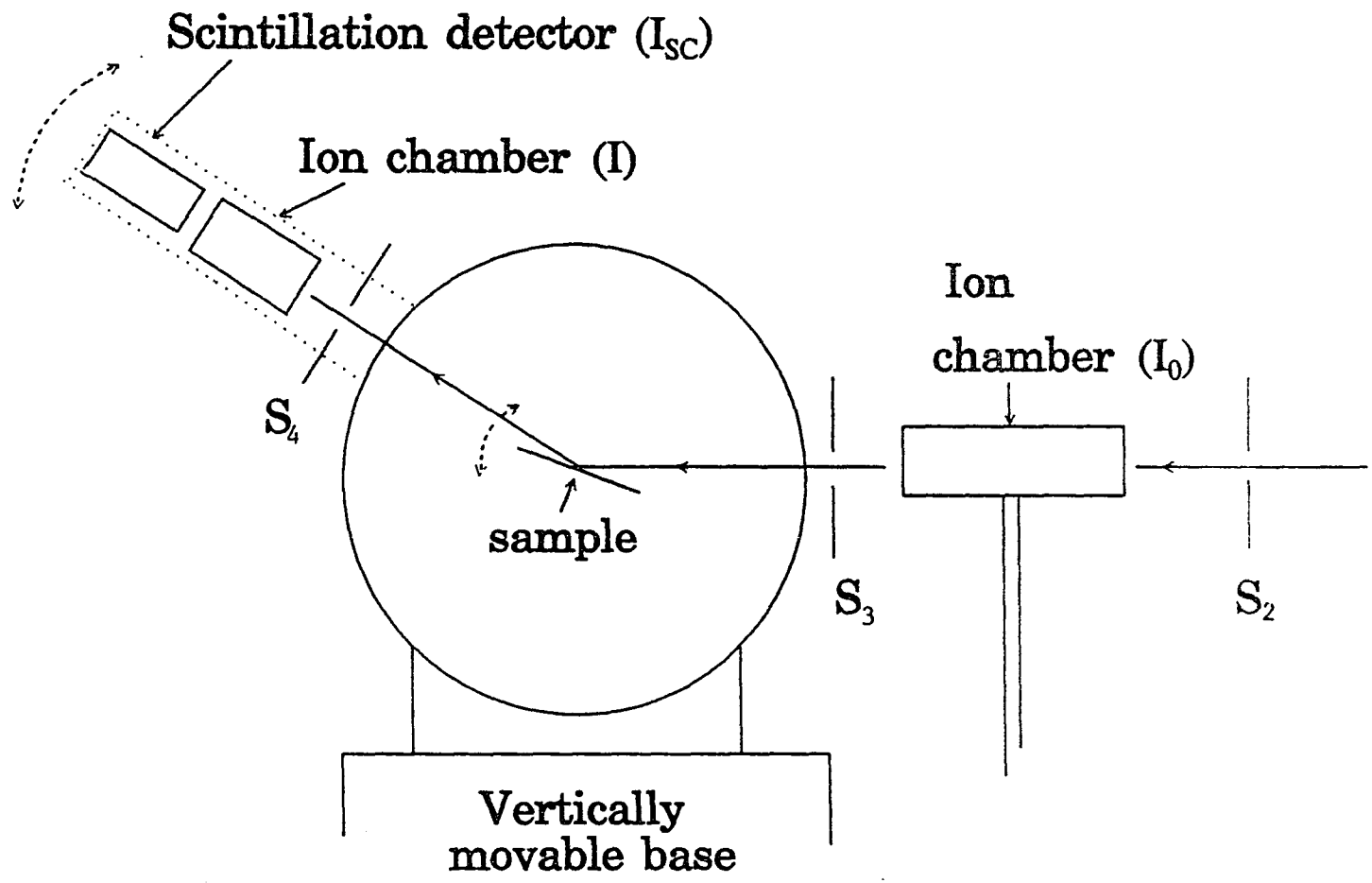

Figure 3.2: Schematic diagram of the experimental setup for x-ray reflectivity measurements.

the thickness of the sample. The beam which enters the experimental hutch through the slit S_2 (hutch slit) then goes through the slit S_3 which is mounted on the fixed arm. The slit S_3 is mounted to trim the tails of the scattered beam from slit S_2 (slit edges act as scattering sources) before the beam hits the sample. The slit S_4 on the rotating arm is used to select only the specular part of the scattered beam from the sample. For reflectivity measurements, slit S_4 is adjusted so that it is slightly larger than slit S_3.

The incident beam is monitored by a gas filled ionization chamber. The gases are selected such that only 10-20% of the x-ray beam is absorbed by the ionization chamber. The detector which monitors the reflected beam is a combination of a partially absorbing ionization chamber and a NaI scintillation detector. This system is useful for collecting data over a large dynamic range. The scintillation detector becomes saturated by the intense reflected beam at very low angles but gives good data at higher angles. The ion chamber signal is overwhelmed by noise at higher angles while giving good data at lower angles. The full reflectivity curve could be obtained by combining the signals from both detectors (see data analysis). Using appropriate gases in the ionization chambers, (see data collection) this detector combination produced data in a range of 5-6 orders of magnitude for the Si-SiO_2 system.

3.3 EXAFS Measurements

For EXAFS measurements, a choice must be made as to which measuring mode is used to determine the signal. The measuring mode is usually dictated by the nature of the sample. The direct method of measuring the absorption by a particular element

in a sample is the transmission mode, where the incident beam and the transmitted beam are monitored using the detectors. There are instances, where the absorption is measured by indirect monitoring processes, that are proportional to absorption. Auger emission and x-ray fluorescence are two such processes. A core hole, created by the photo-ejection of an electron, decays either by emission of fluorescence radiation or Auger electrons. Under certain conditions [57], EXAFS can be measured by the detection of fluorescence radiation or Auger electrons. For example, for dilute and very thin samples, good data can be obtained by measuring EXAFS in the fluorescence mode. For thick and concentrated samples, where transmission mode cannot be used, the fluorescence method can still be applied with appropriate corrections [58], or by detecting the signal from a specific take off angle [59]. Measurement of Auger electron yield is important when surface information is required. Usually, measurements have to be made in a vacuum. The total electron yield measurements involve the detection of Auger electrons, photoelectrons, and secondary electrons and are sensitive to depths from about 500-3000 Å depending on energy. Measurements are often done in a He atmosphere which simplifies them by enhancing the signal. A technique which is specifically applied to thin film surfaces and interfaces is the measurement of fluorescence EXAFS in the glancing angle configuration, developed by Heald and Chen [42-44]. This method has been successfully applied to a large number of interfaces. Thin film EXAFS can be extracted also by measuring the reflected x-rays [60,61]. The samples in our study (milled Sn-Ge(Si) powders) have sufficiently large concentrations to be measured in the transmission mode. Figure 3.3 shows a schematic of the standard experimental setup for the transmission EXAFS measurements. Once the incident x-ray beam is aligned to fall on the sample of interest, the monochromator is scanned in the required

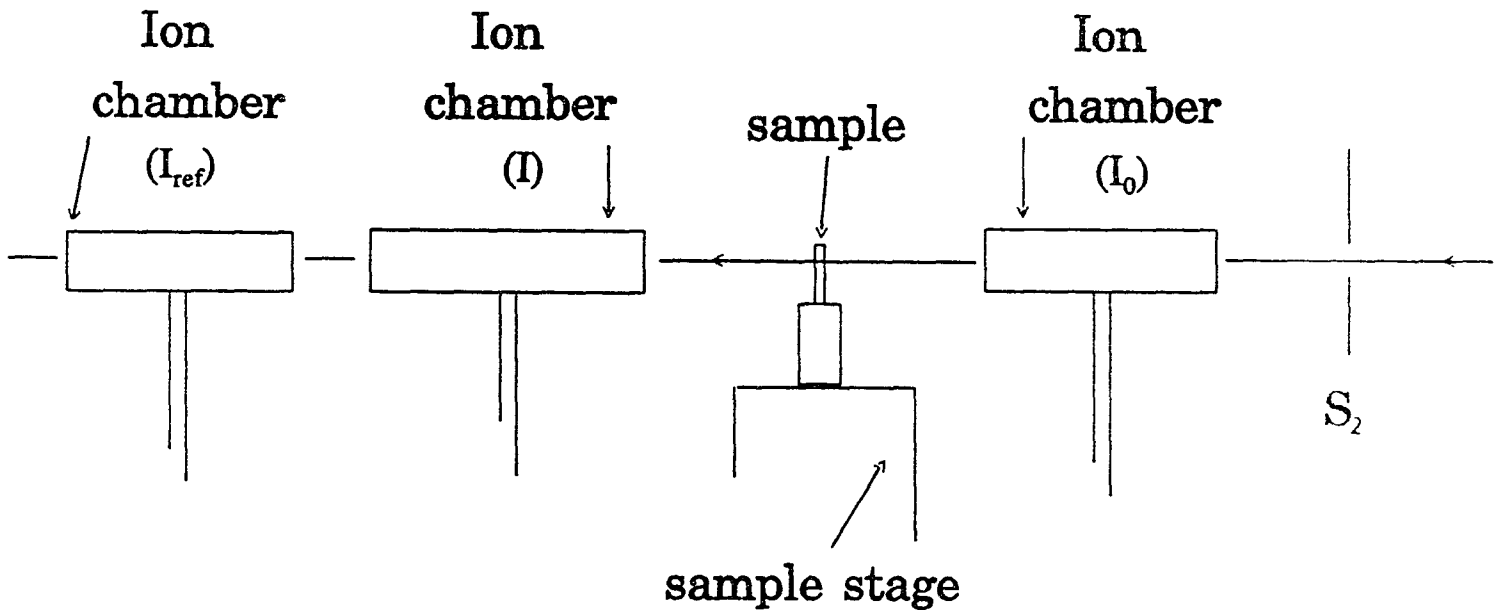

Figure 3.3: Schematic diagram of the standard experimental setup for transmission EXAFS measurements.

energy range to obtain the EXAFS spectrum.

3.4 Sample Preparation

3.4.1 Si-SiO_2 Samples

The Si-SiO_2 samples were grown by Drs. A.A. Bright and G.W. Rubloff at IBM, Yorktown Heights. The thermal Si-SiO_2 samples were grown using both 'wet' and 'dry' oxidation. In some cases HCl, which is thought to decrease impurity concentration at the interface, was added to the oxidation atmosphere. The PECVD oxides were prepared using a He-diluted process developed by Batey and Tierney. This is a silane/nitrous oxide process in which He is added as a diluent to suppress gas phase reactions. The dielectric quality of the oxides have been measured by MOS capacitor measurements. Table 3.1 lists the growth conditions for each sample.

3.4.2 Sn-Ge(Al) Multilayer Samples

The Sn-Ge multilayer samples were deposited on fused quartz substrates at liquid nitrogen temperature (77K), using electron beam evaporation in a belljar system. The substrates were opened alternatively to Sn and Ge sources, using an automatically controlled shutter. The deposition rates were monitored using two rate monitors and maintained at constant, 1.7 Å/s for Ge and 1.3 Å/s for Sn, values. The pressure during deposition was 2.0-3.0 $\times$ 10^{-7} Torr. However, the initial temperature dependent x-ray diffraction measurements of a Sn/Ge (40 Å/50 Å) multilayer of 20 periods showed the crystallization of Ge at a temperature between 130 and 185 °C. Therefore, the Sn-Ge multilayers were not suitable for studying the melting behavior

Table 3.1 The description of the Si-SiO_2 samples

Sample Identification	Oxidation condition	Nominal thickness (Å)
(1) SITH05	Thermal (dry/no HCl)	518
(2) SITH10	Thermal (dry/no HCl)	1081
(3) SIDH10	Thermal (dry/with HCl)	1046
(4) SIWH10	Thermal (wet/with HCl)	1003
(5) SICV05	PEVCD	~ 1000
(6) SICV10	PECVD	~ 500

of Sn and attempts were made to deposit multilayers replacing Ge by Al. (The metal induced crystallization of a-Ge in Ge-Al and Ge-Au films is discussed elsewhere [62,63].) The Sn-Al multilayers were deposited using a UHV chamber [42] modified to deposit both thermal and e-beam evaporated films. Multilayers were deposited on float glass and fused quartz at low temperature and room temperature. However, the films produced were cloudy, and we were unable to obtain good reflectivity measurements.

3.4.3 Sn-Ge(Si) Powder Samples

The entire handling, packing, loading, and unloading etc. associated with Sn-Ge(Si) powder samples was done inside an Ar dry box with moisture and oxygen content less than 5 ppm. Sn-Ge powder samples were first milled using a Brinkmann, Model MM2, Standard Mixer Mill and later, a SPEX 8000 mixer/mill. Sn-Si powder samples were milled using the SPEX 8000 mixer/mill. The starting materials were -100 mesh, 99.999% pure Sn and Ge, and Si ground to the size of -100 mesh from wafers. Milling was done in an o-ring sealed, cylindrical, hardened, tool steel vial, using a steel ball. Powders with varying Sn/Ge (20,30 and 40 vol.% Sn) and Sn/Si (10,25, and 40 vol.% Sn) were milled for nearly about 35 hours.

To pack the samples for x-ray absorption measurements, I used a rectangular copper holder with an array of slots. It is important to select the proper amount of sample, to avoid amplitude distortions due to thickness effects [57]. Samples sieved with -325 mesh were diluted, first with graphite, and later with boron nitride powder. Samples diluted with the latter gave better EXAFS data, due to improved packing. Since boron nitride is hydroscopic, care was taken to bake the powder in a rough vacuum before mixing with samples. The diluents were added to maintain the

absorption step $\Delta\mu x$, at the Sn K-edge at $\sim$ 1.5. (an optimum value to minimize amplitude distortions).

The packed sample holder was enclosed in a copper cell which had kapton x-ray windows, and sealed with indium. Another sample (20 vol.% Sn) was packed in a slotted aluminum plate using thin Al windows to perform heating experiments. An attempt was made to make an α-Sn standard by melting a piece of β-Sn (tetragonal or metallic phase) with a very small amount of Ge ($<$ 0.5 at.%) in a UHV chamber. To start the transformation, the specimen was kept in a freezer at -30°C. After two days the sample had transformed. It was ground to a fine powder and rubbed onto kapton tape. EXAFS analysis indicated that some of the powder had transformed back to tetragonal β-Sn during grinding. For DSC studies, samples (10-15 mg) were sealed in Al pans.

3.5 Data Collection

3.5.1. Si-SiO_2 Samples

The x-ray reflectivity of Si-SiO_2 samples, mounted on the sample platform of the goniometer, were measured at 8.0 and 12.0 keV, using the Si(111) double-crystal monochromator, detuned by $\sim$ 20%. The energy was initially calibrated to the Cu edge energy, 8.980 keV. The incident beam was monitored by filling the ionization chamber (I_0 chamber) with N_2 gas. The ionization chamber which monitored the reflected beam (I chamber) was filled with an Ar,N_2 gas mixture so that $\sim$ 20 % of the beam is absorbed, letting the rest of the beam traverse the chamber to the scintillation detector. The slits S_1, S_3, and S_4 were set at 0.25 mm, 0.1 $\times$ 8 mm^2, and 0.2 $\times$ 8 mm^2, respectively. Figure 3.4 shows the reflectivity signal obtained from the

two detectors. The background scattering was measured by scanning the detector through the reflected beam at several different angles (Figure 3.5).

3.5.2 Sn-Ge(Si) Samples

The Sn K-edge (29200 eV) transmission EXAFS of Sn-Ge(Si) samples were made using the Si(311) double-crystal monochromator, detuned by ~ 20%. The I_0 chamber and I chamber were filled by Ar and Kr gas, respectively. The monochromator entrance slit S_1, was maintained at 0.25 mm and the energy resolution at the Sn K-edge was estimated to be 6.5 eV. Measurements were made at 10 K, 100 K, and 200 K, in a displex refrigerator. Figure 3.6 shows the EXAFS scans obtained for some samples at 10 K. The 20 vol.% Sn (Sn-Ge) sample prepared for heating experiments was heated in a vacuum above the melting point of Sn and up to about 300°C while measuring EXAFS at several temperatures.

The diffraction measurements of Sn-Ge samples were made at room temperature at an energy of 8.5 keV. Measurements were done at beamline X-11B using a modified Phillips goniometer with the 120° position sensitive detector described previously. The Sn-Si diffraction measurements were made at 8.05 keV using the Huber goniometer described in section 3.2.

The DSC analysis was performed in a computer controlled DuPont 910 DSC system. The encapsulated samples were heated in flowing argon at a constant rate of 10°C/min. The control sample was an empty aluminum pan. The calorimeter was initially calibrated with respect to the melting point of indium.

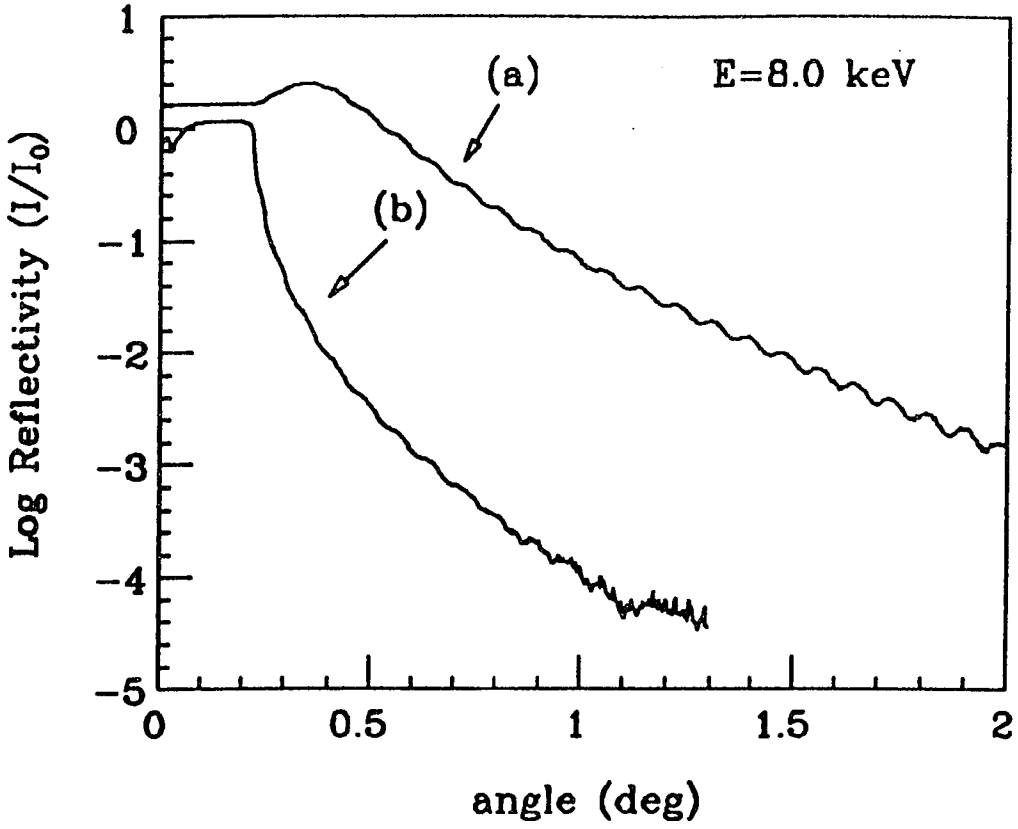

Figure 3.4: The x-ray reflectivity signals obtained for one of the Si-SiO_2 samples at 8.0 keV, from (a) the scintillation detector and (b) the ion chamber.

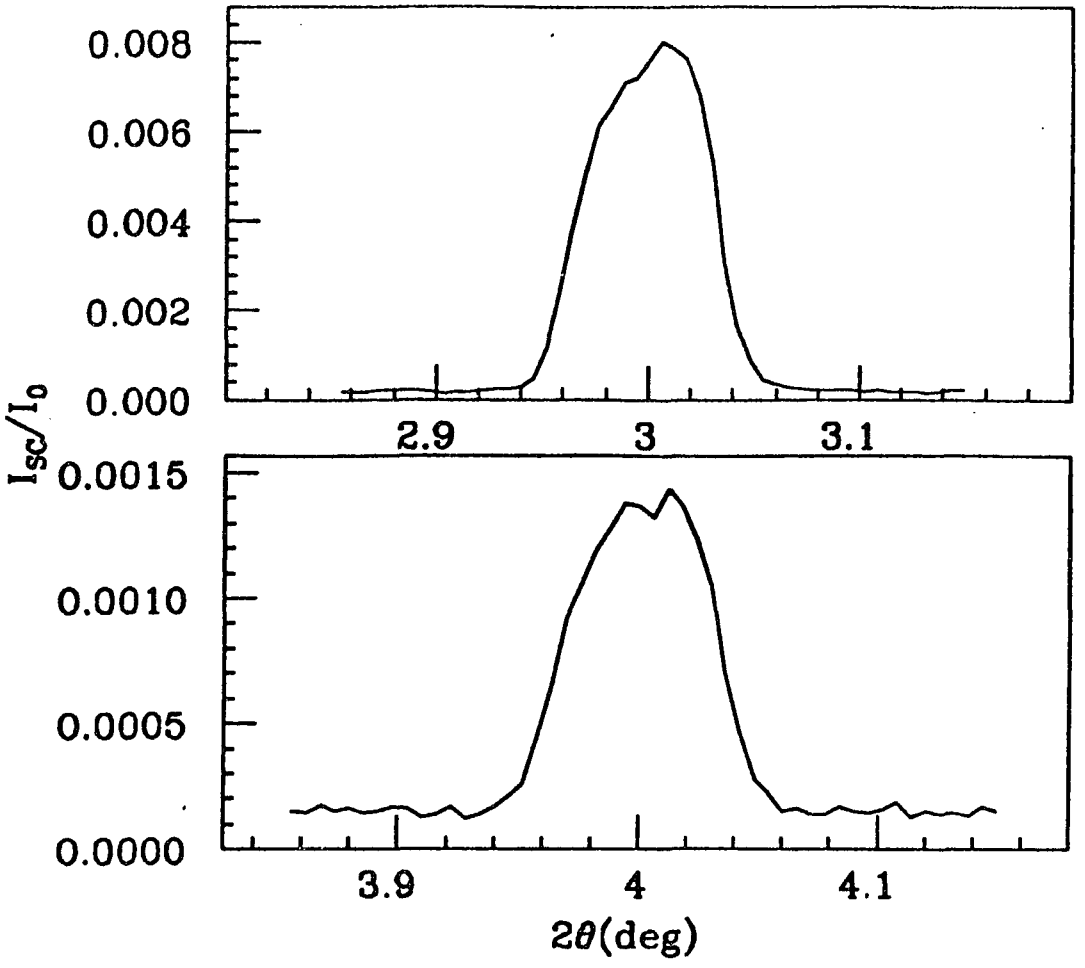

Figure 3.5: The background scattering measured using the scintillation detectors at $\theta = 1.5$ (deg) and at $\theta = 2$ (deg).

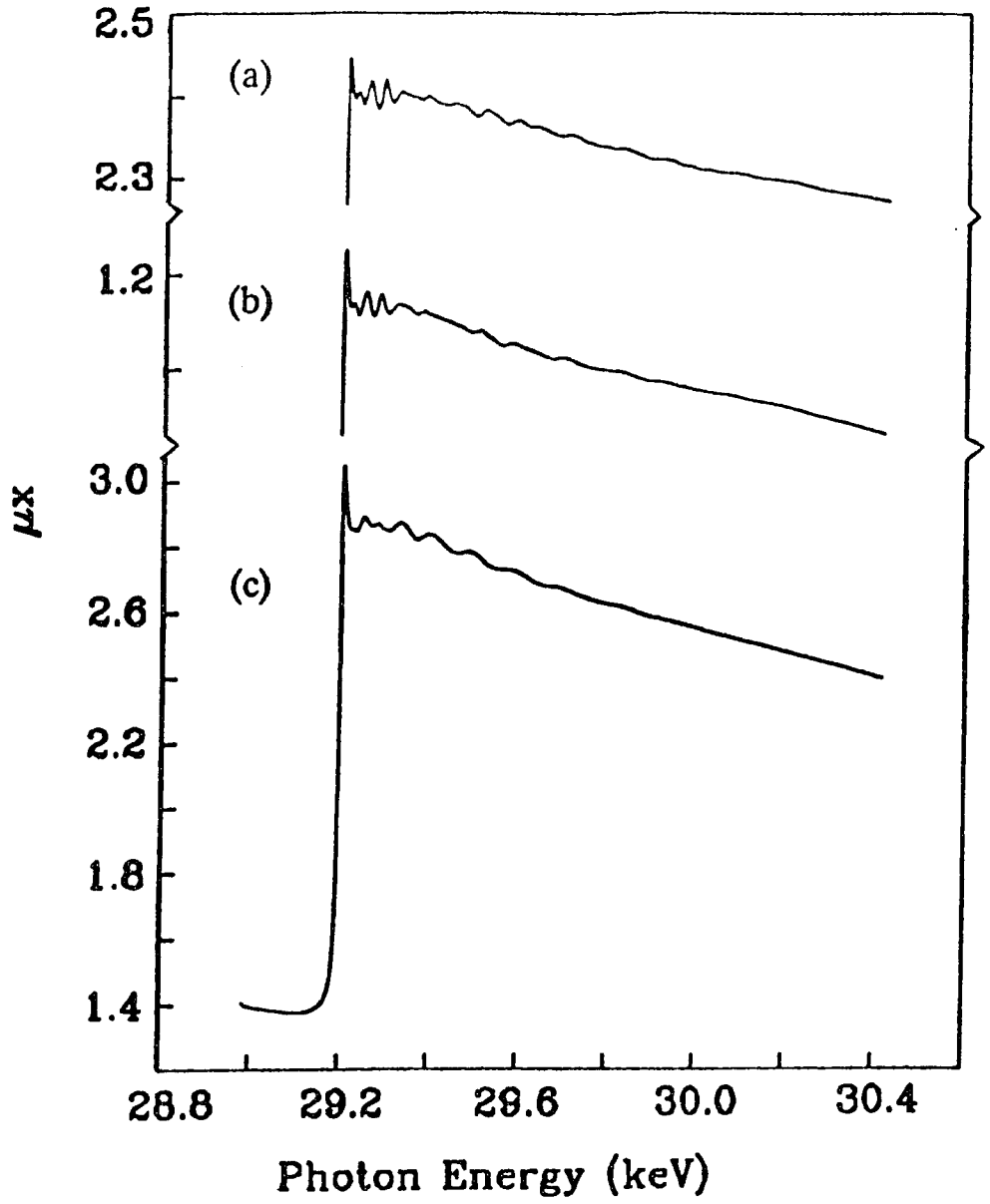

Figure 3.6: Sn edge (29.2 keV) transmission EXAFS data made at 10 K for (a) Sn powder (b) 40 vol.% Sn (in Ge) sample and (c) 20 vol.% Sn (in Ge) sample.

Chapter 4

Si-SiO_2 System

In this chapter, section 4.1 is used to discuss the data analysis procedure and results obtained for Si-SiO_2 system followed by the discussion in section 4.2.

4.1 Data Analysis and results

4.1.1 Dead-time corrections and combined reflectivity

The first step is to obtain the total reflectivity curve for a sample by combining the two curves obtained from the scintillator and ion chamber detectors shown in the Figure 3.4. However one has to consider the following. The scintillation counter stays inactive for a short time after it records an event (an incoming x-ray pulse). This time is referred to as the dead-time, τ, of the counter and to obtain the true counts, a correction which is significant at high counting rates, is required.

We used the following procedure to estimate the dead-time of the scintillation counter. The signals of varying counting rates were simultaneously measured using an ionization chamber and the scintillator, with an attenuator (a 21 mil Al foil) placed in front of the scintillator in order to avoid saturating it. Figure 4.1 shows the curve obtained for the ion chamber versus scintillator counts. The dead-time effect is represented by the deviation of the curve from the straight line which would be expected if the scintillator records the true count rates.

Our dead-time estimation showed that at 8.0 keV there is a region (an angular range) in which both the ionization chamber and scintillator have good signals where the dead-time correction is not important (Figure 4.2) Therefore, by simply matching

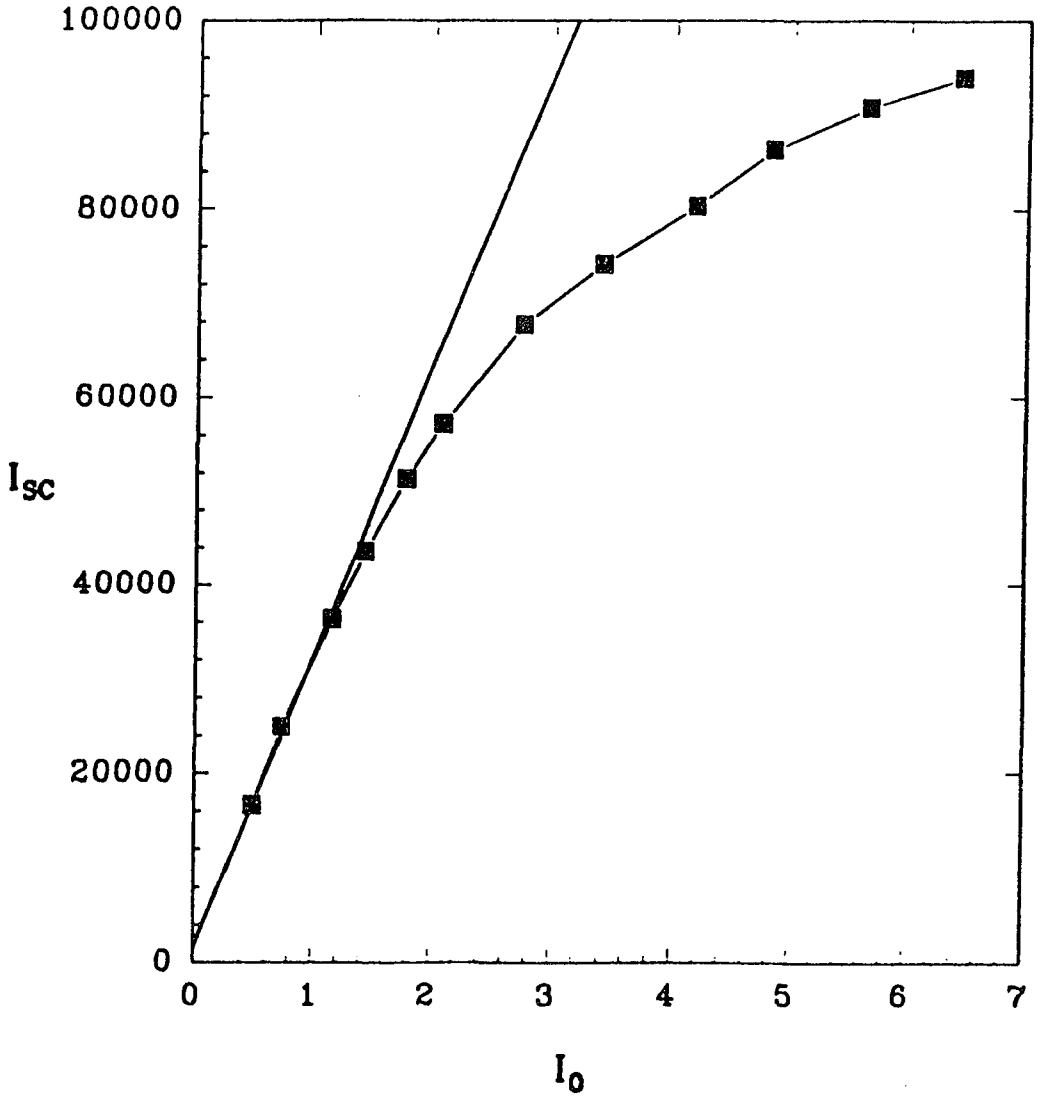

Figure 4.1: The variation of the scintillation detector signal I_{SC}, against the ion chamber signal I_0. The deviation of the curve from the straight line is due to the dead time effects of the scintillation detector.

the ion chamber signal and the scintillator signal in this region (this region includes approximately about 150 data points.) using a conversion factor, scintillator data in the saturated region were replaced by the converted ion chamber data. Figure 4.3 (a) and (b) shows the total reflectivity curves obtained for the samples at 8.0 keV. At 12.0 keV, in the region where dead-time correction is not important, the signal from the ion chamber is noisy and matching is not possible. In this case, one has to match the data in a region where dead-time correction is already applied. However, only the short ranged ion chamber data at 12.0 keV were used during the analysis (see, section 4.1.2).

Reflectivity of samples at 8.0 keV basically shows the features discussed in section 2.1.2. The thermal oxides have similar overall slopes but oscillations of different frequencies, depending on the oxide thickness. PECVD oxides have bigger slopes compared to the thermal oxides and one can also see a beat in the reflectivity amplitude in one of the CVD oxides. These features give good initial hints about the modelling required to obtain information on the film's morphology.

4.1.2 Fitting procedure

The information about the morphology of the films was obtained using the least square fitting method described previously [42]. Fitting was begun with a two layer model which gave excellent fits except for the PECVD sample that had a beat in reflectivity. Fitting parameters involve the parameters which depend on the experimental conditions and those which depend on the sample. The former parameters, the zero angle offset and the normalization factor, were adjusted using the low angle reflectivity data obtained at 8.0 and 12.0 keV. The use of two energies helps to reduce the correlations between the density and zero angle errors, and the

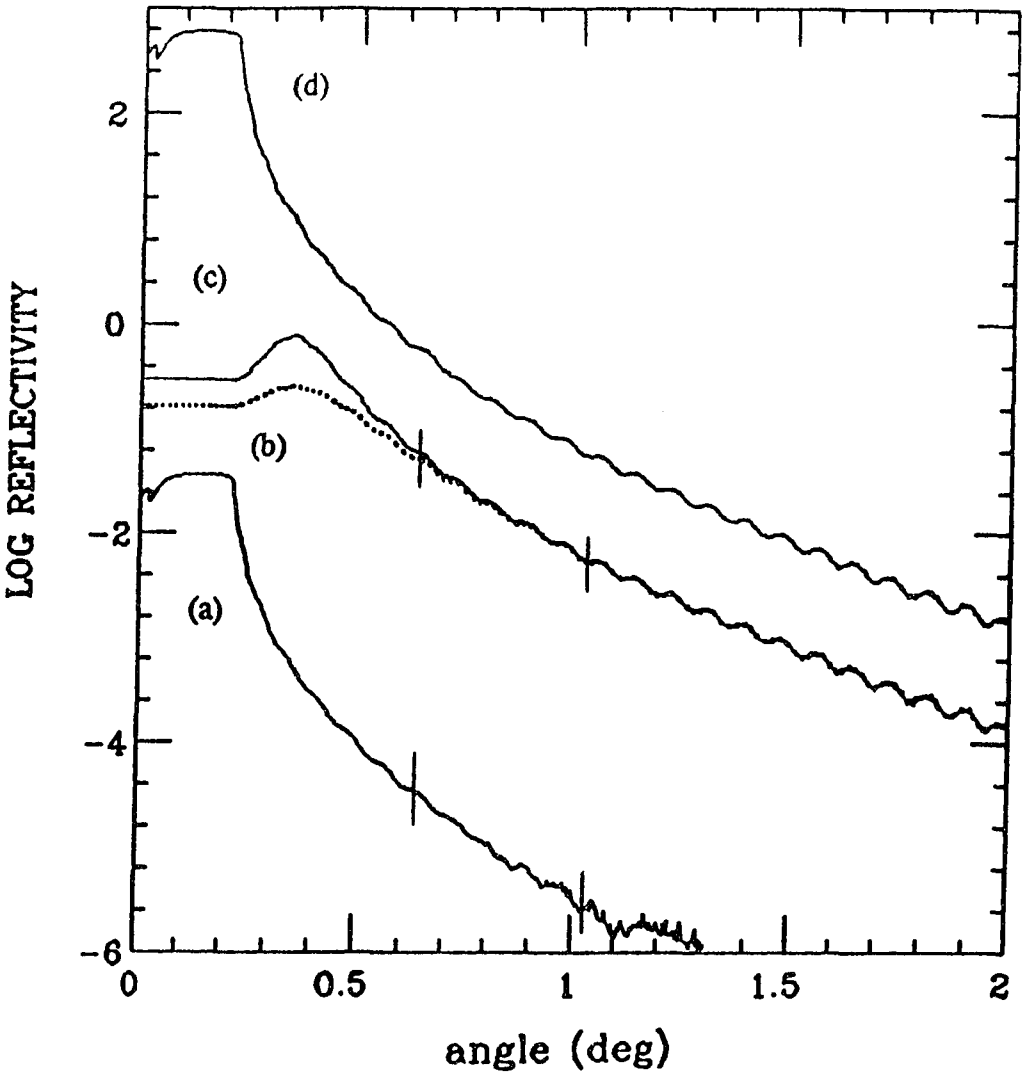

Figure 4.2: Reflectivity of curves obtained for one of the Si-SiO_2 samples (a) from the ion chamber (b) the scintillation detector (c) after applying the dead time correction to the scintillation detector signal and (d) after matching the signals from the ion chamber and the scintillation detector in the range indicated by two vertical lines.

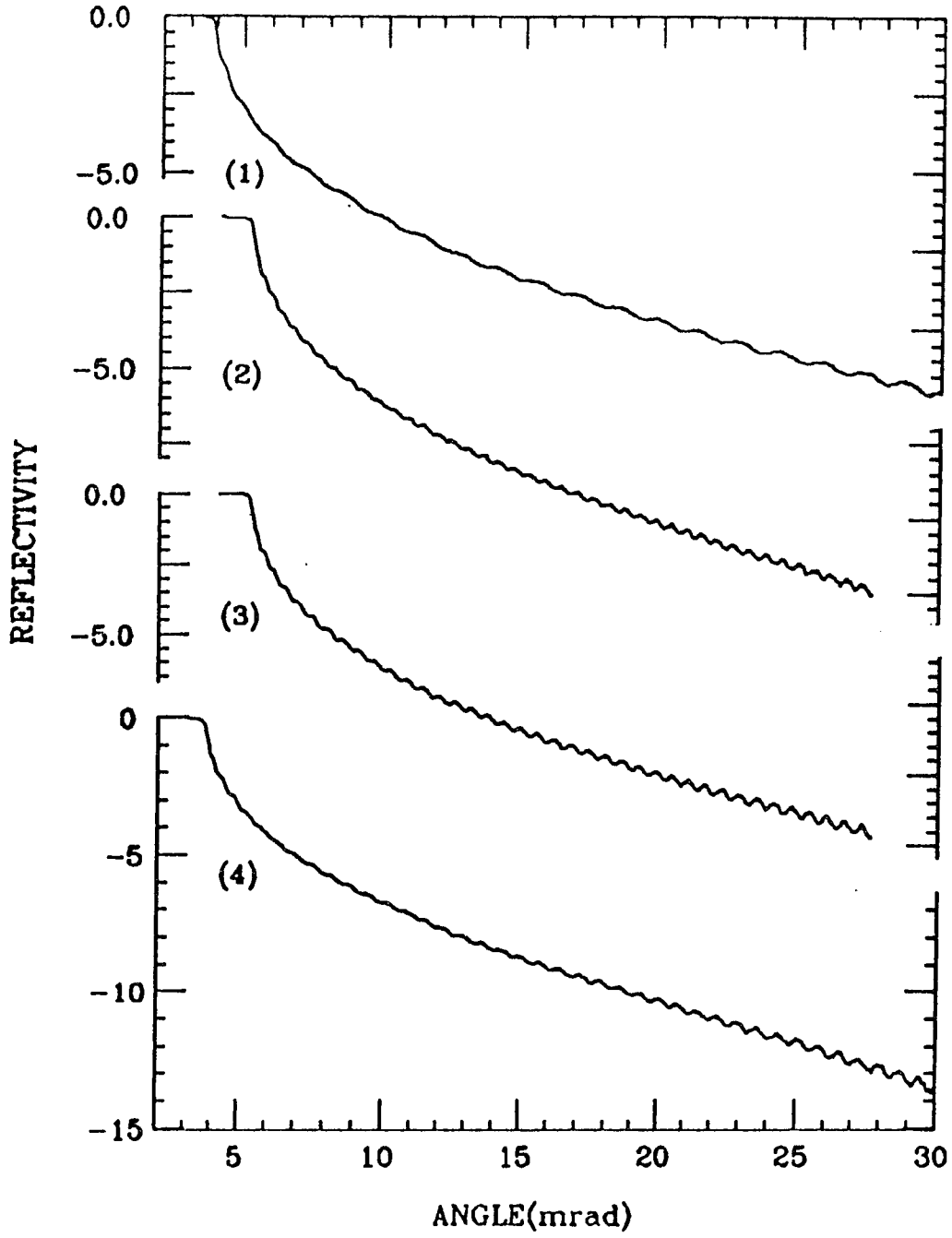

Figure 4.3: (a) Total reflectivity curves obtained for thermal oxides at 8.0 keV. (1) SITH05 (2) SITH10 (3) SIDH10 (4) SIWH10.

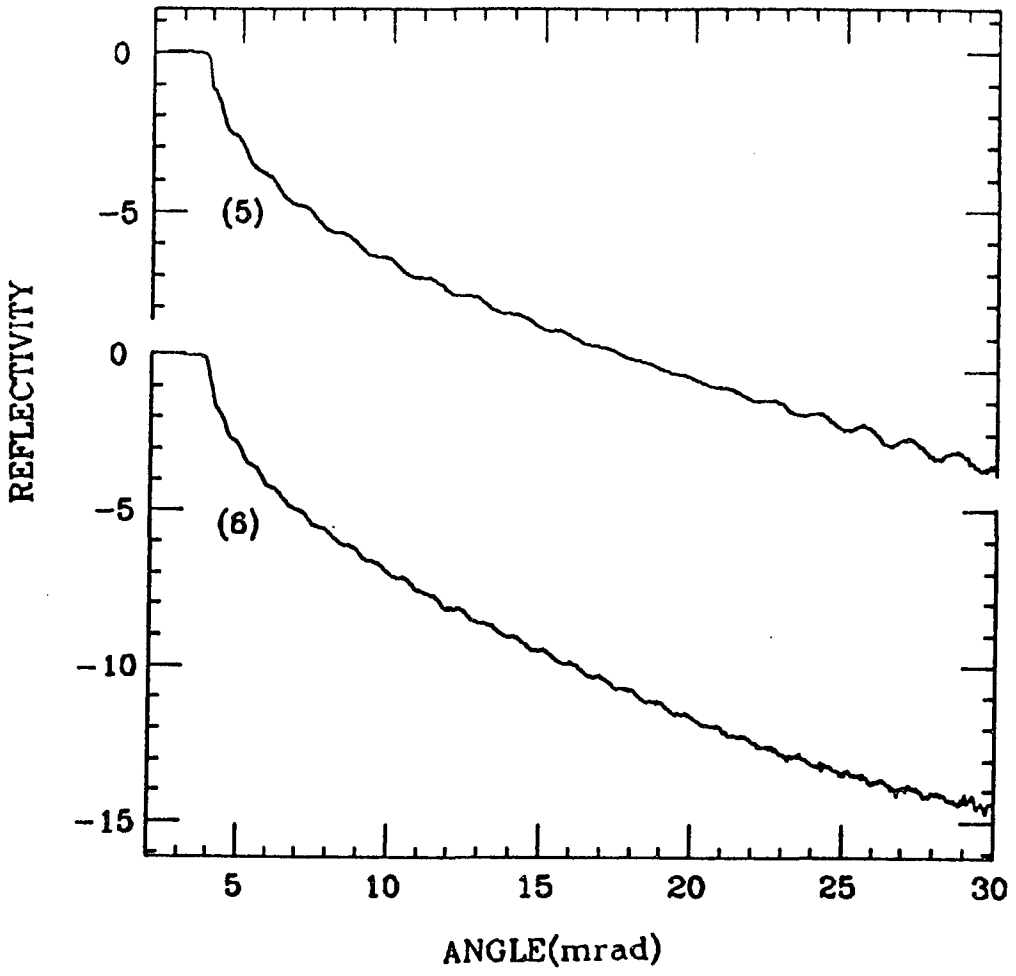

Figure 4.3: (b) Total reflectivity curves obtained for PECVD oxides at 8.0 keV. (5) SICV05 (6) SICV10.

associated zero angle corrections were found to be very small (of the order of 10^{-5} radians). The parameters associated with the sample, the surface roughness, density and thickness of the oxide layer, and the roughness at the Si/SiO_2 interface were adjusted by fitting them to the overall reflectivity curve at 8.0 keV.

The PECVD sample with a beat in the reflectivity oscillations required a different model. Fits were attempted by placing an additional oxide layer at various depths including the oxide surface, and good results were obtained only when the layer was placed at the interface. Figure 4.4 shows the fits obtained for one of the samples using this approach. Figure 4.5 shows the fits obtained for each sample, with emphasis on the interface region. A factor $(\theta/\theta_c)^{-4}$, was removed to bring out details at the interface. The corresponding fitting results are given in Table 4.1.

4.2 Discussion

4.2.1 Thickness and density

Since the reflectivity shows a large number of uniformly distributed small oscillations in an angular range of 3 to about 30 (mrad), the fitted thickness parameters have a high accuracy. Table 4.1 shows the similarities of oxide layer densities between the thermal oxides and the PECVD oxides, which is a sign of their good quality.[9] The densities of the thermal oxides are similar, irrespective of the oxidation conditions. The results are also similar to those obtained by Irene *et al* [5], for SiO_2 layers in conventional thermal oxides of similar thicknesses using ellipsometry, and by Chason *et al.* [64] for thin SiO_2/Si structures using x-ray reflectivity.

An interesting feature is the beat in x-ray reflectivity observed in SICV05

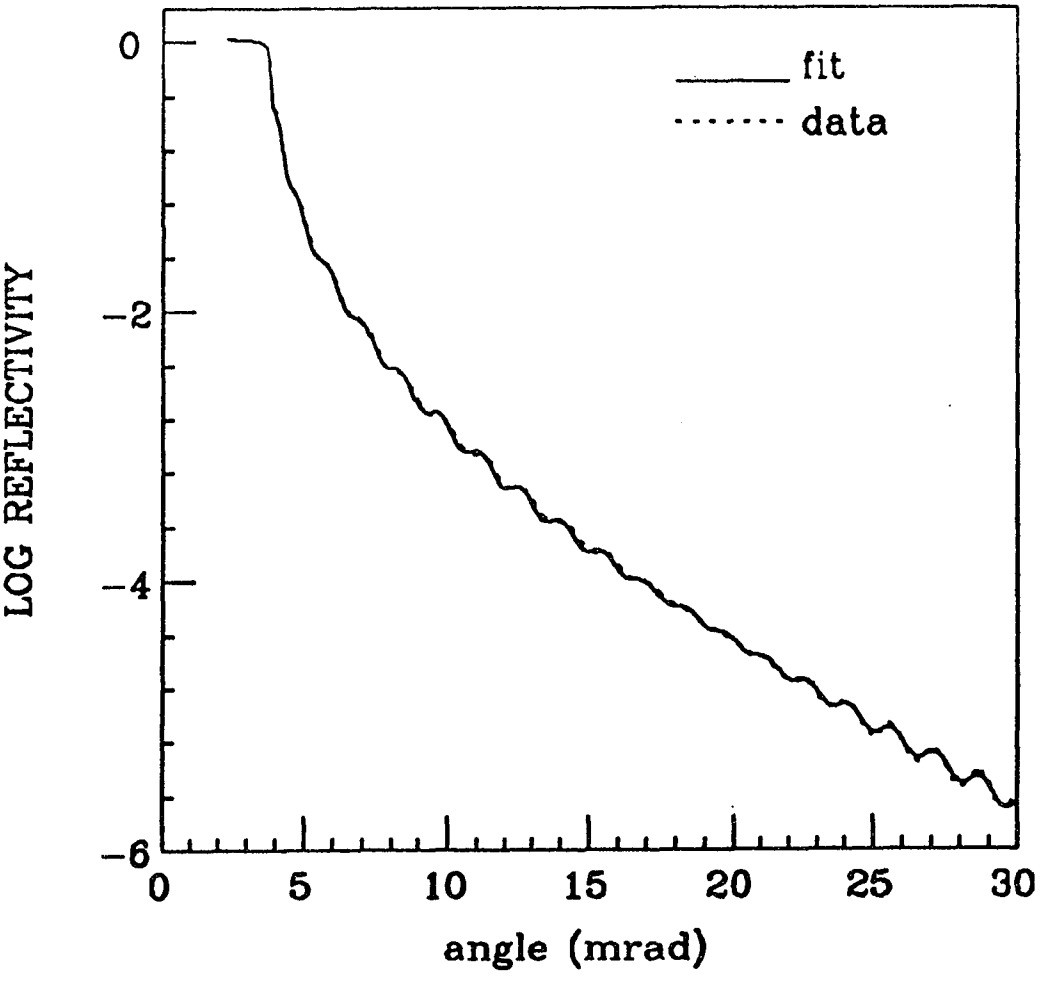

Figure 4.4: Fit (dashed line) obtained for SICV05 SiO_2 film compared to the data (solid line).

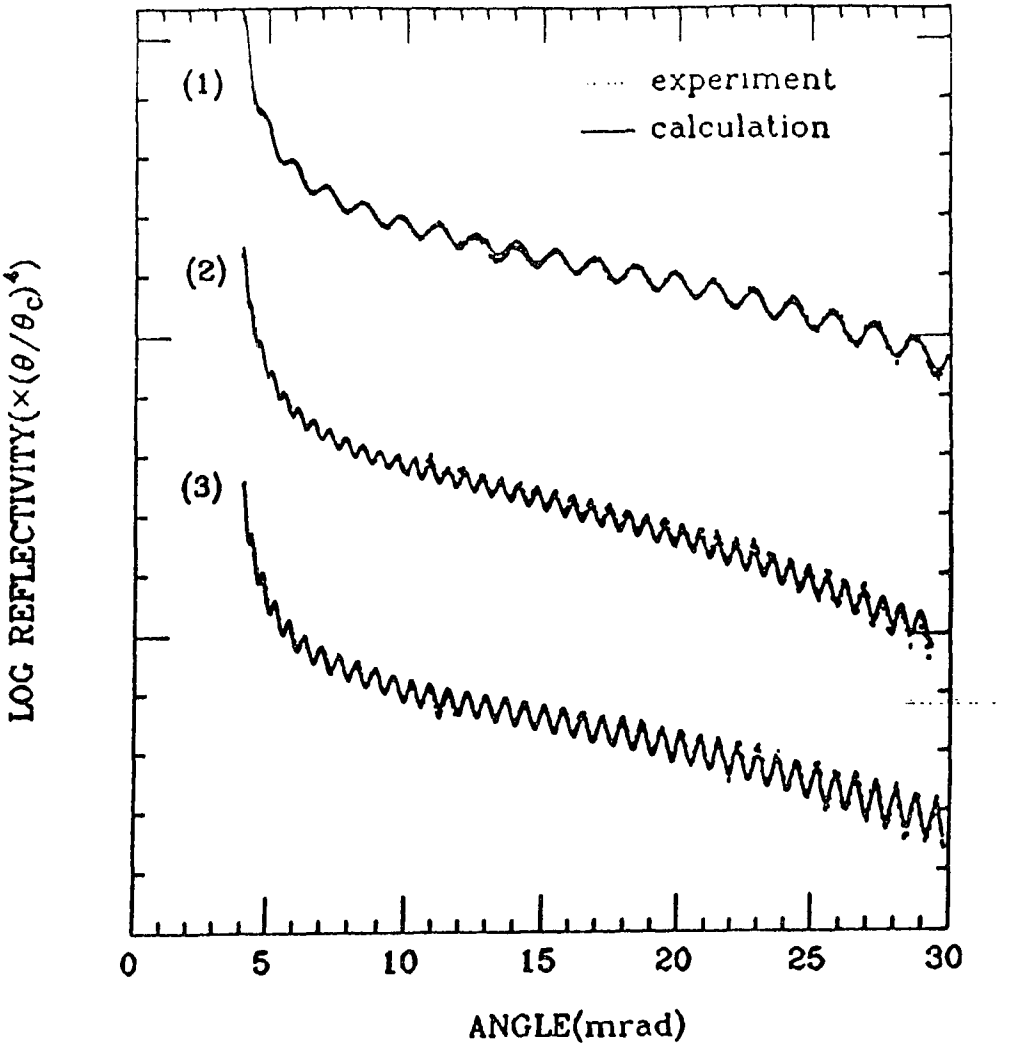

Figure 4.5: (a) Fits obtained for thermal oxides at 8.0 keV with a factor $(\theta/\theta_c)^4$ removed to enhance the interfacial details. (1) SITH05 (2) SITH10 (3) SIDH10.

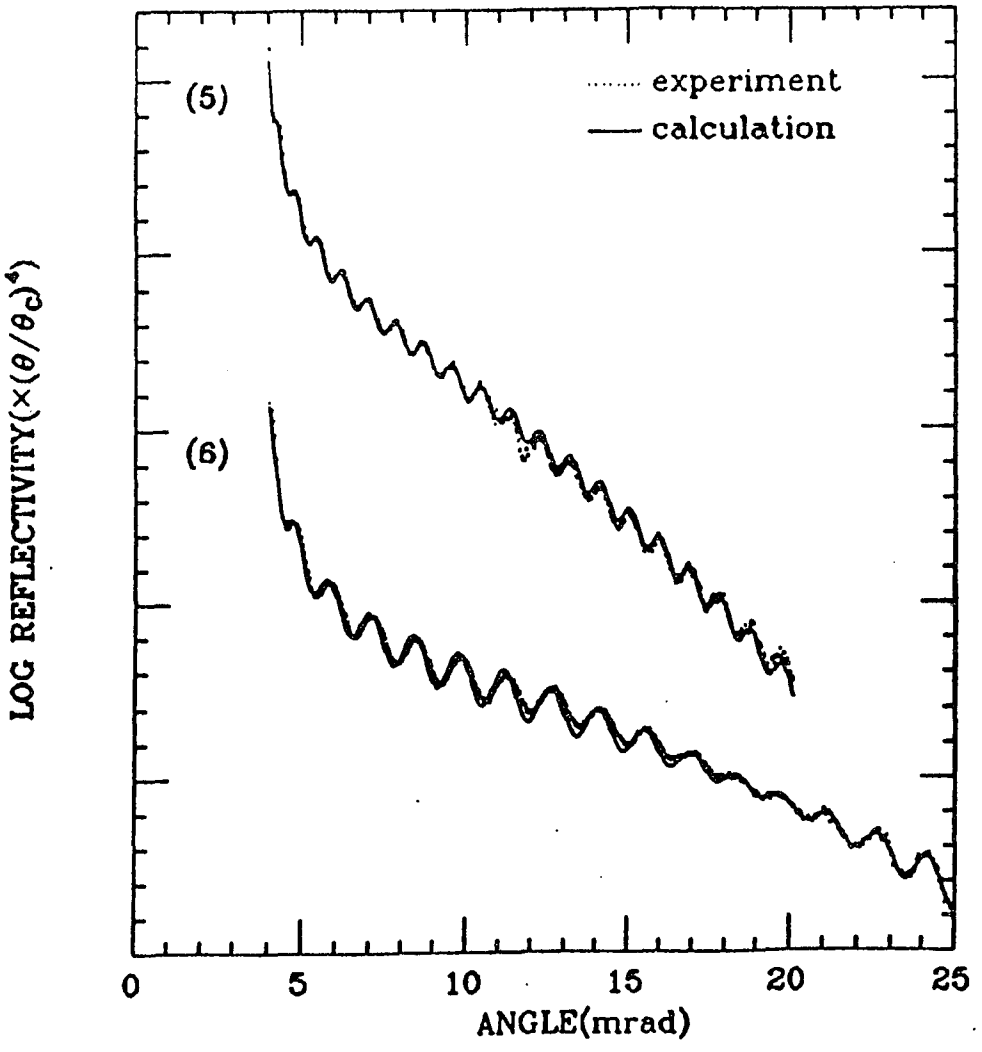

Figure 4.5: (b) Fits obtained for PECVD oxides at 8.0 keV with a factor $(\theta/\theta_c)^4$ removed for clarity. (5) SICV10 (6) SICV05.

Table 4.1 Parameters used to fit the reflectivity data of the samples. Two SiO_2 layers were required to fit the PECVD oxide SICV05.

Sample	Layer	Thickness (Å)	Density (g/cm^3)	Roughness (Å)
(1) SITH05	SiO_2	517 ± 1.0	2.26 ± 0.01	4.3 ± 0.2
	Si	.....	2.33	1.0 ± 2.0
(2) SITH10	SiO_2	1061 ± 3.0	2.24 ± 0.02	4.3 ± 0.1
	Si	.....	2.33	0.1 ± 2.0
(3) SIDH10	SiO_2	1137 ± 4.0	2.26 ± 0.02	4.8 ± 0.1
	Si	.....	2.33	0.0 ± 2.0
(5) SICV10	SiO_2	799 ± 4.0	2.25 ± 0.02	9.8 ± 0.1
	Si	.....	2.33	8.3 ± 3.0
(6) SICV05	SiO_2	475 ± 2.0	2.25 ± 0.02	6.2 ± 0.2
	SiO_2	42 ± 2.0	2.21 ± 0.02	3.0 ± 2.0
	Si	.....	2.33	6.0 ± 1.5

PECVD oxide. Fitting results show that the beat is due to a thin oxide layer of different density buried near the interface. This buried layer is only a consequence of the surface preparation technique used prior to the deposition. However, the results show the high sensitivity of x-ray reflectivity to density variations in the oxide layer enabling us to further review the extensively studied interface of the thermal oxides. (see section 4.2.3)

4.2.2 Roughness

Our model to interpret the interface roughness only gives an rms value. The real interface width is about three times the rms value. The interface roughness data for thermal oxides shows relatively small values, indicating a very narrow silicon-silicon oxide interface. The best fits for the thermal oxides are obtained for roughness values which are nearly zero. However the error bar indicates that the roughness value lies in the range of 0-2 Å. This value would translate to an interface layer of several monolayers thick. As shown in the model calculations, the overall slope in reflectivity is determined only by the surface roughness. Therefore, the surface roughness values have a relatively high accuracy. The roughness values of the thermal oxides also show that the oxide does not tend to roughen as it grows thicker.

The PECVD oxides, however, show higher roughness values than the thermal oxides. The negative effect of higher interface roughness on carrier mobility, interface density of states, and dielectric breakdown is discussed elsewhere [65-67]. Therefore, the higher interface roughness in the PECVD oxides is an area where further improvement is necessary.

In all of the oxides, the interpretation of surface roughness can be complicated by the adsorption of thin low-Z contamination layers such as hydrocarbons, since the films were exposed to ambient conditions. However, model calculations show that this

was not a major problem for the angular range used in this work.

4.2.3 Si/SiO_2 Interface

The emphasis of this work was to compare the morphology of the films of thermal and PECVD oxides. We also attempt to review the Si/SiO_2 interface, based on our results. Studies done on the PECVD oxides are limited. However, the thermally grown oxides have been widely investigated in the past several years using a number of interface probing methods which provide various pictures of the Si/SiO_2 interface. These variations may be attributed to the different conditions under which the Si substrate was prepared or the sensitivity of the probing technique to the different aspects of the interface. It is often questioned that how the transition occurs from crystalline Si to amorphous SiO_2 where a large change in molar volume occurs during the oxidation. There are two major but contrasting views about the Si/SiO_2 interface based on the experimental evidence. Both views invoke the existence of a transition region between the substrate and the oxide layer. In one case, this transition layer was found to be 5-10 Å thick. An interface layer of 7 ± 2 Å $SiO_{0.4}$ has been reported by ellipsometry [68]. The transmission electron microscopic studies (TEM) [69-71] also agree with a thin interfacial transition layer. For example, the lattice imaging studies made by Ourmazd *et al.* [70,71] show that the c-Si → a-SiO_2 transformation occurs via an ordered crystalline oxide layer of $\simeq$ 5 Å thick. In fact, this crystalline layer was found to be tridymite, a stable, bulk form of SiO_2. Our study did not directly reveal the chemistry of the Si/SiO_2 interface. However the rms roughness values of the thermal oxides agree with these results.

In another case, a much thicker region was observed, where the transition oxide layer extended as far as 30-50 Å from the oxide-silicon interface. The photoelectron

spectroscopic studies [72-75] show the existence of Si^{+1}, Si^{+2}, and Si^{+3} suboxide states at the Si/SiO_2 interface. Grunthaner *et al.*[74] and Himpsel *et al.*[75] showed that the Si^{+1}, and Si^{+2} states are localized within 6-10 Å of the interface, while the Si^{+3} states extend ~30 Å further. This picture can be modelled by introducing an intermediate oxide layer near the interface for the thermal oxides studied in our work. The intermediate layer being Si rich, apparently should have a higher density and if the difference is significant compared to the bulk oxide film, beats can be expected to observe in reflectivity, as in the case of SICV05 oxide. Figure 4.6 shows calculations made for SIDH10 thermal oxide using an intermediate layer of 40 Å thick. The optical constants for this layer were calculated assuming Si_2O_3 composition. The sample reflectivity shows gradually increasing oscillations in the logarithmic scale, with the increasing angle. However, calculated reflectivity shows the evolution of beats which are significant when the density of the intermediate oxide layer is between that of Si and bulk SiO_2 and become extinct as the density reaches the value of Si. Fits attempted with a three layer model with an intermediate layer, makes its density approach the density of the bulk oxide.

4.3 Conclusions

In this study we have examined the morphology of films of thermally and PECVD grown $Si\text{-}SiO_2$ thin heterostructures using glancing angle x-ray reflectivity. Both types of oxides have similar qualities in terms of density, suggesting that the low temperature PECVD technique can produce oxides of good bulk quality. However, the Si/SiO_2 interface of the PECVD oxides show the higher roughness than the thermal oxides. Further improvement in the interface quality of the PECVD oxides

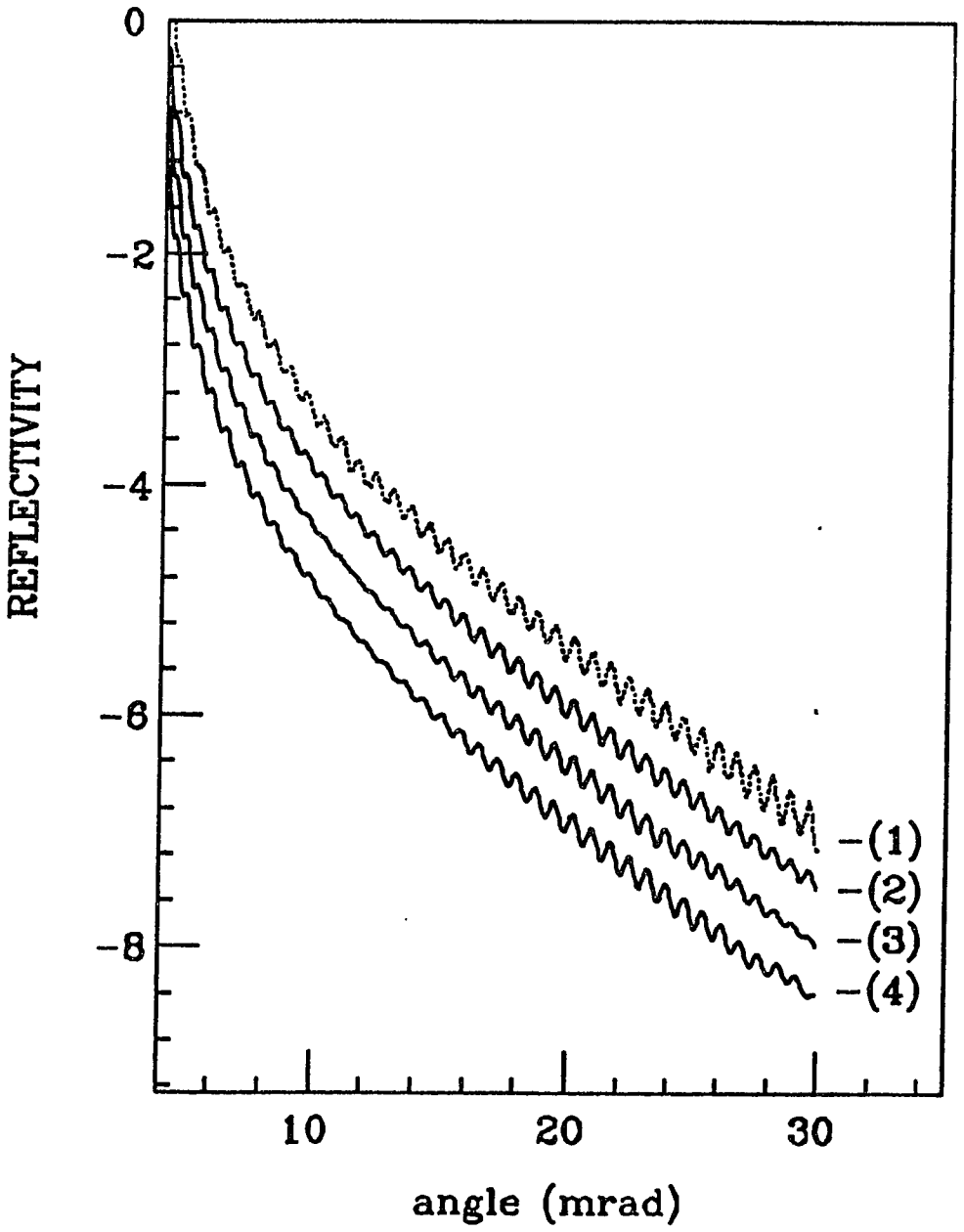

Figure 4.6: A comparison of x-ray reflectivity of SIDH10 sample (1) with the calculated reflectivities by introducing a 40 Å thick suboxide layer of density (2) 2.27 (3) 2.29 and (4) 2.31 g/cm^3. In each case the beats in the reflectivity can be observed.

is required, since the roughness plays a major role in electrical characteristics of these heterostructures. Results also show the sensitivity of x-ray reflectivity to thin buried thin buried layers at or near the interface. The current results on the reflectivity of thermal oxides do not show an extended interfacial transition region (30-50 Å), as observed by some experimental techniques. However, the rms interface roughness is not incompatible with a thinner transition layer (5-10 Å), as discussed above.

Chapter 5

Sn-Ge System

5.1 Data analysis and results

5.1.1 DSC and x-ray diffraction data

Figure 5.1 shows the DSC data obtained for Sn-Ge samples of varying concentrations. The melting transition is represented by a dip in the curve with respect to the plateau. The figure shows the broadened melting transition region of Sn in the samples such that tailing also occurs in the low temperature region. This behavior was interpreted by Koch *et al.* as the interface initiated depression of melting of Sn [14]. At 20 vol.% Sn concentration, the transition is represented by only a slight dip. Also, it is important to notice that there are no other features, such as dips or spikes, in the curve that would be expected in the case of a decomposition or compound formation during heating. The enthalpy of fusion corresponding to the transition can be obtained by evaluating the area subtended by the dip and the results (see, table 5.1) show that there is a reduction of enthalpy of fusion with decreasing Sn concentration as observed by Jang *et al.* [15].

The x-ray diffraction data (Figure 5.2) also show a systematic decrease in the intensity of β-Sn peaks with decreasing Sn concentration. At 20 vol.% Sn, the Sn diffraction peaks have almost disappeared indicating that Sn is in a different state. Another clear feature is the systematic broadening of the Ge peaks as the Sn concentration decreases. Since the powders are ball milled, broadening can be caused by both the particle size and a non-uniform strain. Therefore, to determine the particle size, the method described by DeKeijser *et al.*(1982) [76,77] was applied. This is

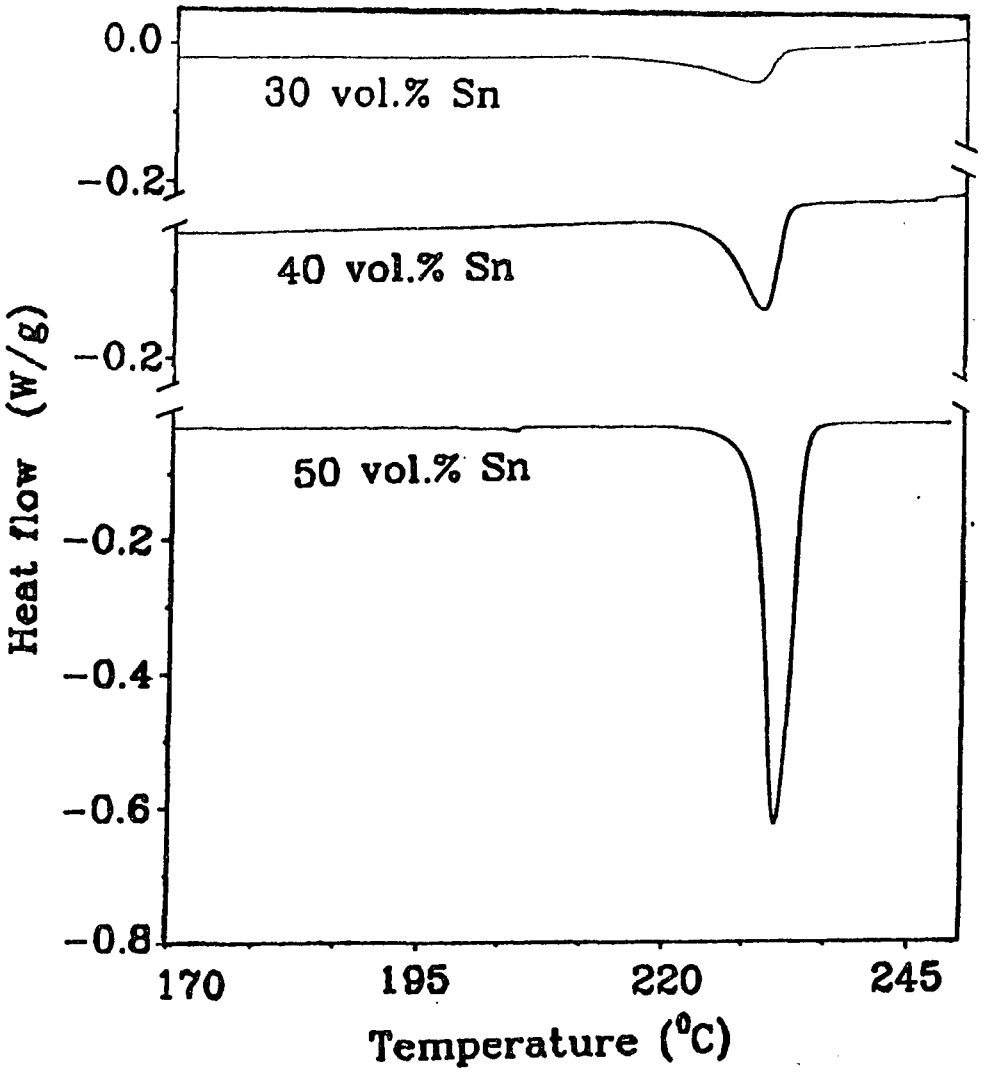

Figure 5.1: DSC data obtained for Sn-Ge powder samples. The melting enthalpy is found by evaluating the area subtended by the dip which correspond to the melting transition of Sn.

Table 5.1 Composition dependence of the melting enthalpy of Sn-Ge samples. The experimentally obtained melting enthalpy of pure Sn was 61.5 J/g.

Sample (vol.% of Sn)	Melting enthalpy of Sn (J/g)
40	48.8
30	20.0
20	3.6

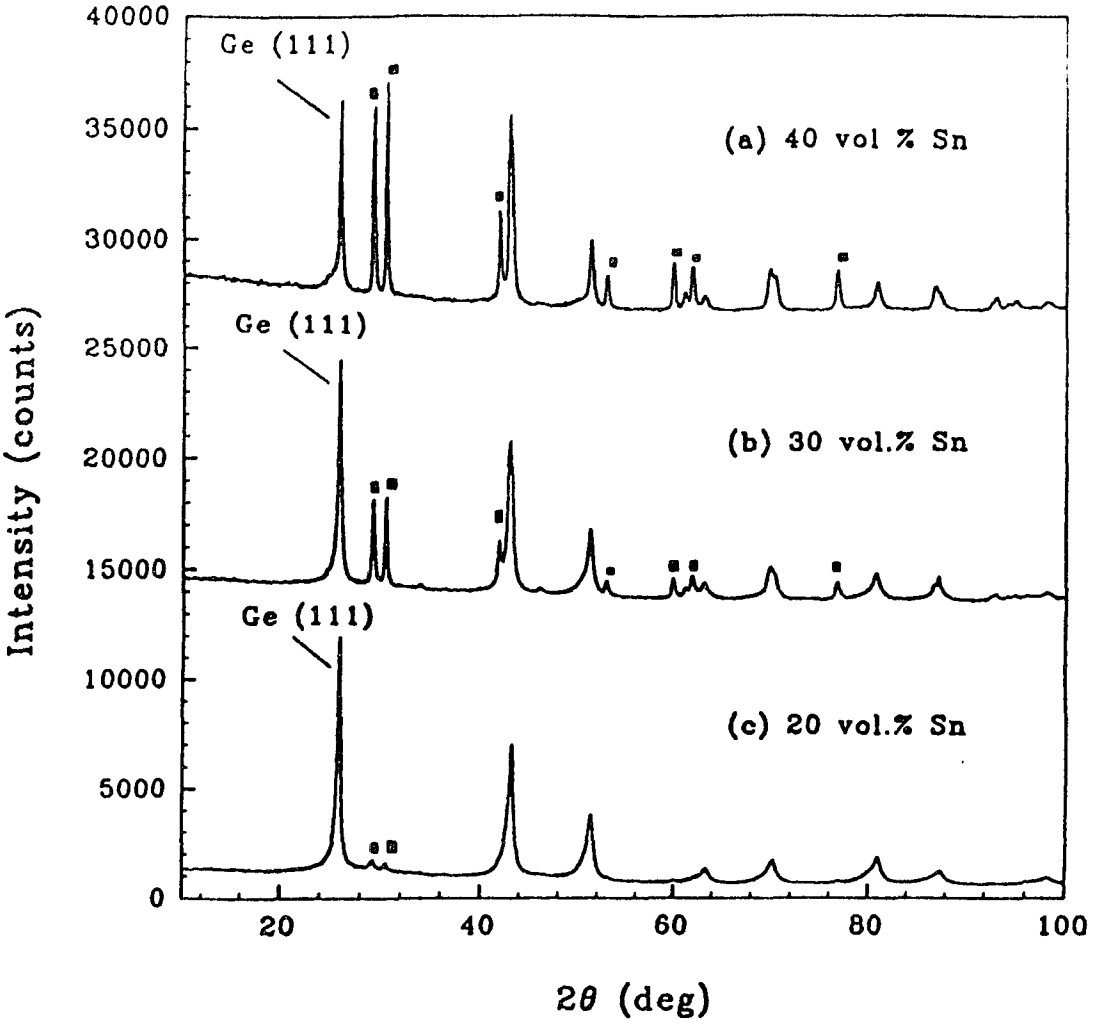

Figure 5.2: Room temperature x-ray diffraction measurements of (a) 40 vol.% Sn (b) 30 vol.% Sn and (c) 20 vol.% Sn (in Ge) samples taken at 8.5 keV. Peaks marked by a box corresponds to β-Sn diffraction profiles.

essentially a single peak procedure, but could be extended to multiple peaks. The diffraction profile was assumed to be Voigtian, which is a convolution of the Cauchy profile due to the crystallite size and the Gaussian profile which arises from the strain. The Cauchy and Gaussian components are separated using the ratio, ϕ, of the FWHM of the profile to its integral breadth ($\phi = 2w/\beta$). β is determined by evaluating the area within the diffraction peak and the background level. When $\phi = 0.63662$, this profile is fully Cauchy and when $\phi = 0.93949$, it is fully Gaussian. The Voigt function method is strictly valid as long as ϕ lies between 0.63662 and 0.93949.

If h refers to the experimental profile, g to the standard profile, and f to the true structurally broadened profile, then:

$$\beta_C^f = \beta_C^h - \beta_C^g \qquad (5.1)$$

$$(\beta_G^f)^2 = (\beta_G^h)^2 - (\beta_G^g)^2 \qquad (5.2)$$

Subscripts C and G stand for the Cauchy and Gaussian components respectively. The crystallite size is given by:

$$D = \frac{\lambda}{\beta_C^f \cos\theta} \qquad (5.3)$$

and the strain by:

$$e = \frac{\beta_C^f}{4\tan\theta} \qquad (5.4)$$

β is measured on the 2θ scale in radians. λ and θ are the wavelength and the corresponding Bragg angle. Since the Ge(111) profile is well separated and statistically

more suitable, the analysis of peak broadening was carried out on the Ge(111) peak of each sample. The results are given in Table 5.2.

Table 5.2 Average particle size of Ge powders determined by analyzing Ge(111) diffraction profile using equation 5.3. Systematic decrease in the particle size is seen with the decreasing Sn concentration.

Sample (vol.% of Sn)	Peak position $(2\theta)°$	$\phi = 2w/\beta$	Average Ge particle size D(Å)
40	51.26	0.81	405 ± 155
30	51.22	0.83	300 ± 95
20	51.22	0.86	250 ± 70

5.1.2 EXAFS data

The data analysis discussed below was done using the University of Washington EXAFS data analysis software package.

5.1.2 (a) Background subtracted EXAFS χ data

The first step is to extract [54] the EXAFS interference function $\chi(k)$ from the experimentally measured absorption spectrum (Figure 3.6). In analyzing experimental measurements, the threshold energy E_0, mentioned in section 2.2, is associated with some feature at the absorption edge. In our case, the maximum derivative point was chosen to be the edge position (threshold energy). Besides the absorption due to the edge of interest, there is background absorption due to the other edges in the same element and absorption by the other elements in the sample. These absorptions are represented by the smoothly varying pre-edge region, which extends to the post-edge region in the spectrum. Removal of pre-edge background is done by fitting a linear fit to the pre-edge region and subtracting the extrapolated smooth curve from the spectrum above the edge. The resulting spectrum is then normalized with respect to the edge step followed by the post-edge background subtraction. Removal of the post-edge background involves isolating the oscillatory part due to EXAFS by subtracting the smoothly varying part from the EXAFS range of the spectrum (30-1000 eV in this case). Using a cubic spline function and adjusting the number of knots the smoothly varying part is obtained. Conversion from the energy space to the k-space gives the standard χ data, which is a characteristic of the absorbing material.

Figure 5.3 shows the k^2 weighted EXAFS $\chi(k)$ data obtained at 10 K for powder samples of 40 vol% Sn and 20 vol.% Sn compared to the EXAFS of β-Sn powder. Systematic changes in EXAFS are seen when the Sn concentration is varied. The

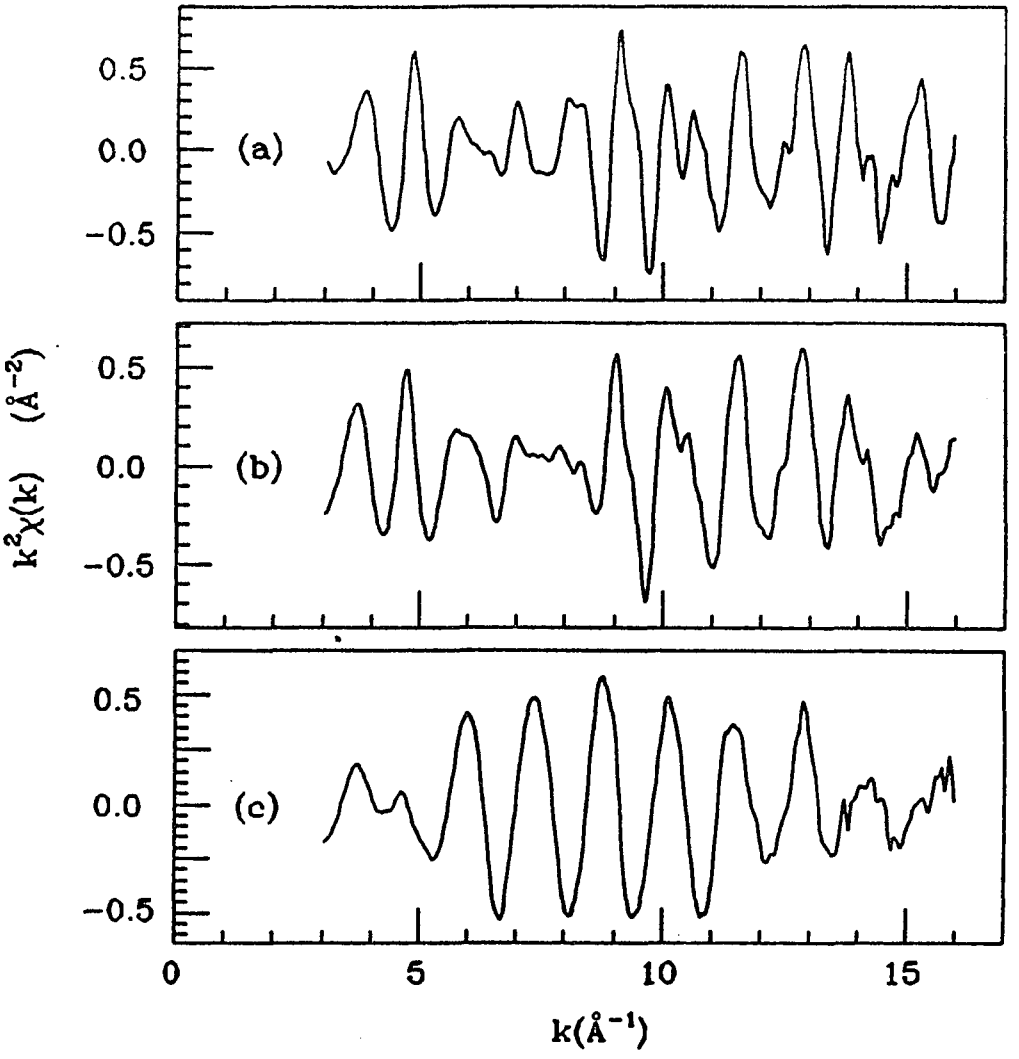

Figure 5.3: Background subtracted k^2 weighted EXAFS for the Sn K-edge obtained at 10 K for (a) β-Sn powder (b) 40 vol.% Sn and (c) 20 vol.% Sn samples.

characteristic dip in the Sn EXAFS envelope observed at about 7 $Å^{-1}$ is due to two factors. As discussed in section 2.2.1, the backscattering amplitude $F_j(k)$ of Sn shows a valley at about 7 $Å^{-1}$. In addition, Sn has two close first near neighbor shells which are only 0.18 Å apart (4 atoms at 3 Å, and 2 atoms at 3.18 Å with respect to an absorber). The interference effects between the two shells also contributes to the dip. However, at 20 vol% Sn the dip has diminished giving initial indications that the Sn near neighbor backscattering environment has changed. Also, the envelope shows a behavior similar to the $F_j(k)$ of Ge (see Figure 2.4). When we measured the EXAFS of the 20 vol.% Sn sample as a function of temperature, it was observed that there was essentially no change in EXAFS (Figure 5.4) as the sample was heated above the melting point of Sn, and thermal damping was much less than that for β-Sn.

5.1.2 (b) Fourier Transform of $\chi(k)$

The above EXAFS includes scattering from different near neighbor shells and consists of sinusoidal oscillations of various frequencies determined by the near neighbor distances, R_j. The contributions from different coordination shells can be separated by Fourier transforming $\chi(k)$:

$$F(r) = \frac{1}{\sqrt{2\pi}} \int k^n \chi(k)\, e^{ikr} dk. \qquad (5.5)$$

The weighting factor, k^n, with n = 1,2 or 3 is used depending on the specific system under study. For example a small n emphasizes the lower Z contributions while large n often improves the transform for high Z materials. The resulting spectrum in r-space, normally referred to as the Radial Structure Function (RSF) or EXAFS Radial

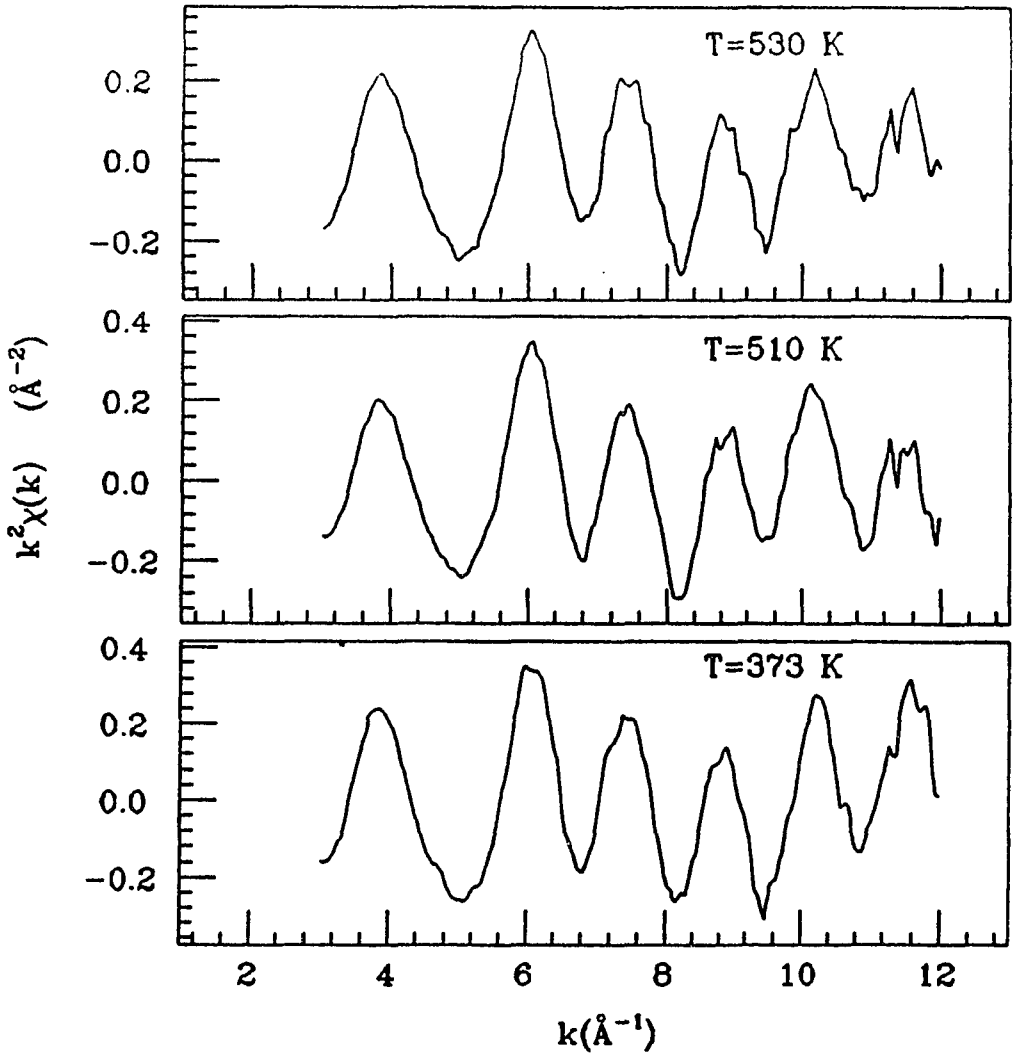

Figure 5.4: $k^2\chi(k)$ of 20 vol.% Sn sample measured at T=373 K, 510 K and 530 K.

Distribution Function (RDF), consists of a series of peaks centered at positions corresponding to various coordination-shell distances. The distances are shifted from the real shell distances due to the k dependence of the phase. Figure 5.5 shows the EXAFS RDFs obtained for Sn powder, 40 vol.% Sn and 20 vol.% Sn, by transforming the k^2 weighted data over the k-space range of 3.4 to 16 $Å^{-1}$. The 40 vol.% Sn RDF clearly shows a new peak P_B which has evolved on the left-hand side of the peak P_A which corresponds to the first Sn-Sn nearest neighbors of the β-Sn phase. At this point, we can identify this new form of Sn to be interfacial Sn, as suggested by Turnbull *et al.* At 20 vol.% Sn, the peak P_A vanishes leaving only peak P_B, indicating that Sn is not in the β-phase at this concentration. In other words, the mixture, in which there are both bulk and interfacial Sn phases, has essentially reduced down to the interfacial phase at 20 vol.% Sn concentration. Also, there are essentially no higher shells at this concentration, indicating that the interfacial phase is disordered.

5.1.2 (c) Standards

The single-shell EXAFS peak at 20 vol.% Sn concentration is a good starting point to begin the extraction of structural information about this interfacial Sn form. However, a suitable set of standards is needed for comparison. The contamination of the α-Sn standard by β-Sn made it difficult to use during our analysis. β-Sn has two close shells, which complicates the extraction of a single Sn-Sn bond. Therefore, the first shell EXAFS due to α-Sn was calculated using the FEFF theoretical code (Version 4.08) which takes into account the curved wave nature of the photoelectron. The program requires the many electron correction parameter, S_0^2, as an input. This was adjusted by fitting the calculation to the experimental data of the first two shells

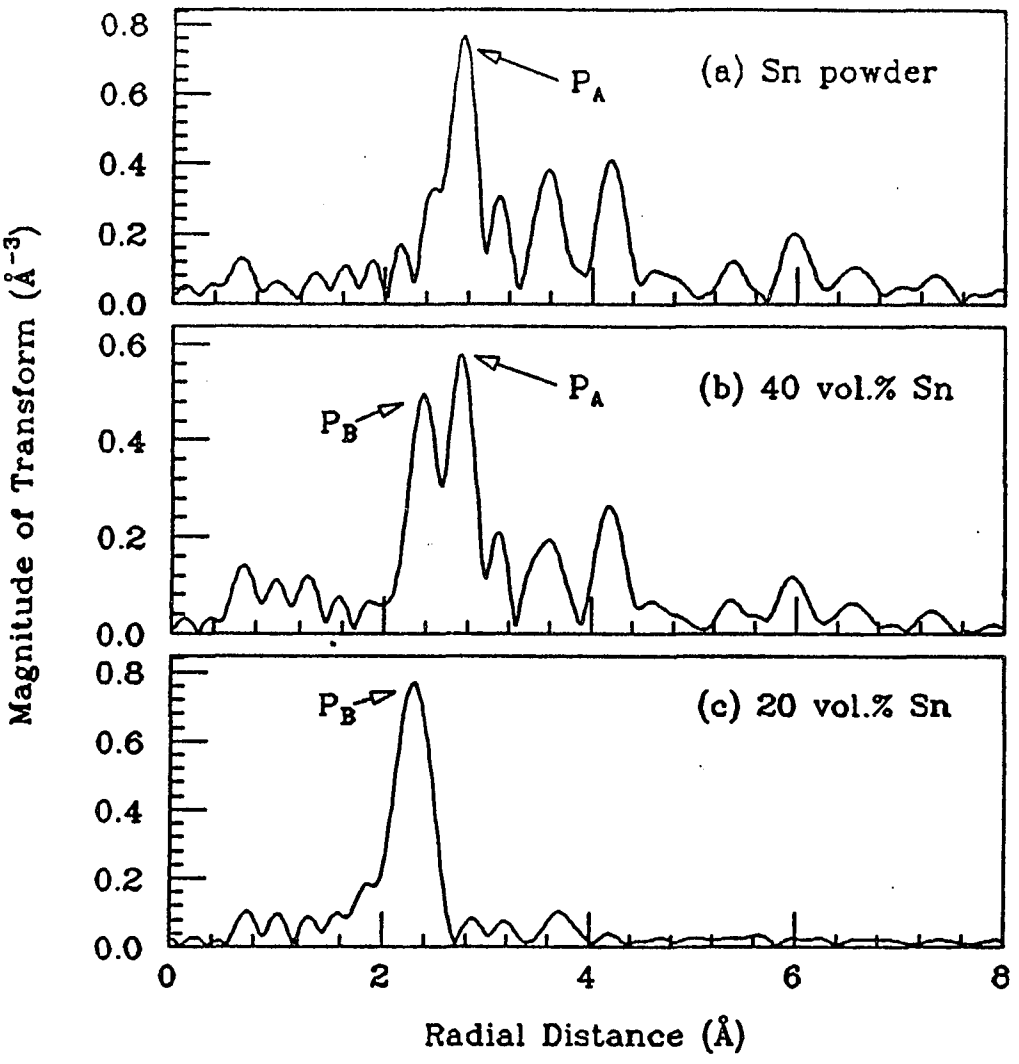

Figure 5.5: Fourier transforms of EXAFS $k^2\chi(k)$ (at 10 K) for the Sn K-edge in (a) Sn powder (b) 40 vol.% Sn and (c) 20 vol.% Sn.

of the β-Sn powder. Figure 5.6 shows a fit obtained for β-Sn powder using this calculation. A value of 0.85 was found for S_0^2. S_0^2 is mainly an atomic factor and can be transferred to the other calculations which involve the same absorber. We also used the FEFF theoretical code to calculate the first-near-neighbor EXAFS from a 50 at.% α-SnGe alloy using two approaches. One approach was to use a 50 at.% α-SnGe alloy with a Sn atom surrounded by 4 Ge atoms in a chemically ordered zinc blende structure. The second approach was to assume that a Sn atom is surrounded by two Ge atoms and two Sn atoms so that the 50:50 atomic ratio is preserved whereas the chemical environment could be random. In both cases, the first-near-neighbor distance of 2.62 Å was used in the calculations, by assuming the lattice parameters of the alloy (6.06 Å) to have the average value of the lattice parameters of α-Sn and Ge (6.46 Å and 5.65 Å, respectively [78]). Figure 5.7 shows the comparison of k^2 weighted EXAFS $\chi(k)$ of the 20 vol.% Sn sample and the calculated ordered 50 at.% α-SnGe alloy. The two spectra are in very close agreement with each other suggesting that the spectrum of the 20 vol.% Sn sample is essentially due to single-shell EXAFS of Sn-Ge first-near-neighbors with a bond length near 2.62 Å.

5.1.2 (d) The Inverse Transform and Curve Fitting

One rather straightforward method of obtaining structural parameters is to compare the unknown with the standards in the k-space. In this method, the contribution from a single shell, or sometimes, the interfering multiple shells in the r-space of both samples and standards can be isolated by inverse transforming (filtering) the selected range to the k-space. i.e:

$$k^n \chi_j(k) = \frac{1}{\sqrt{2\pi}} \int_{r_{min}}^{r_{max}} F(r)\, e^{-i2kr} dr \qquad (5.6)$$

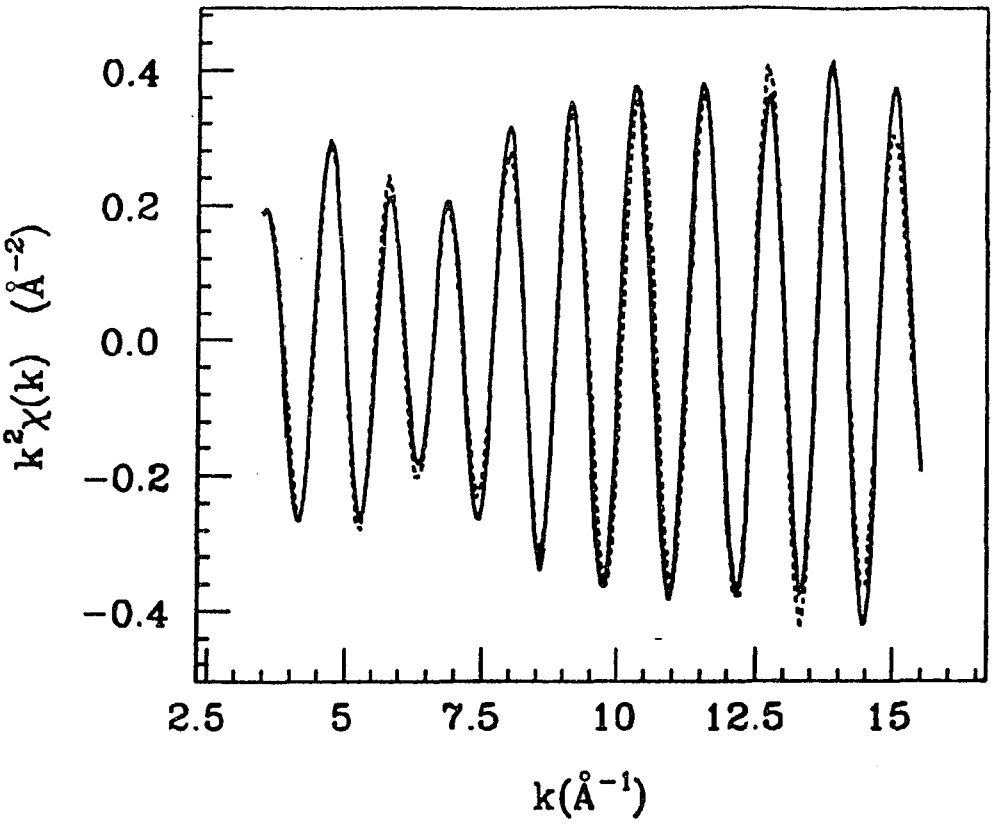

Figure 5.6: Fit obtained for Sn powder data using the FEFF calculation which is used to adjust the S_0^2 factor for Sn.

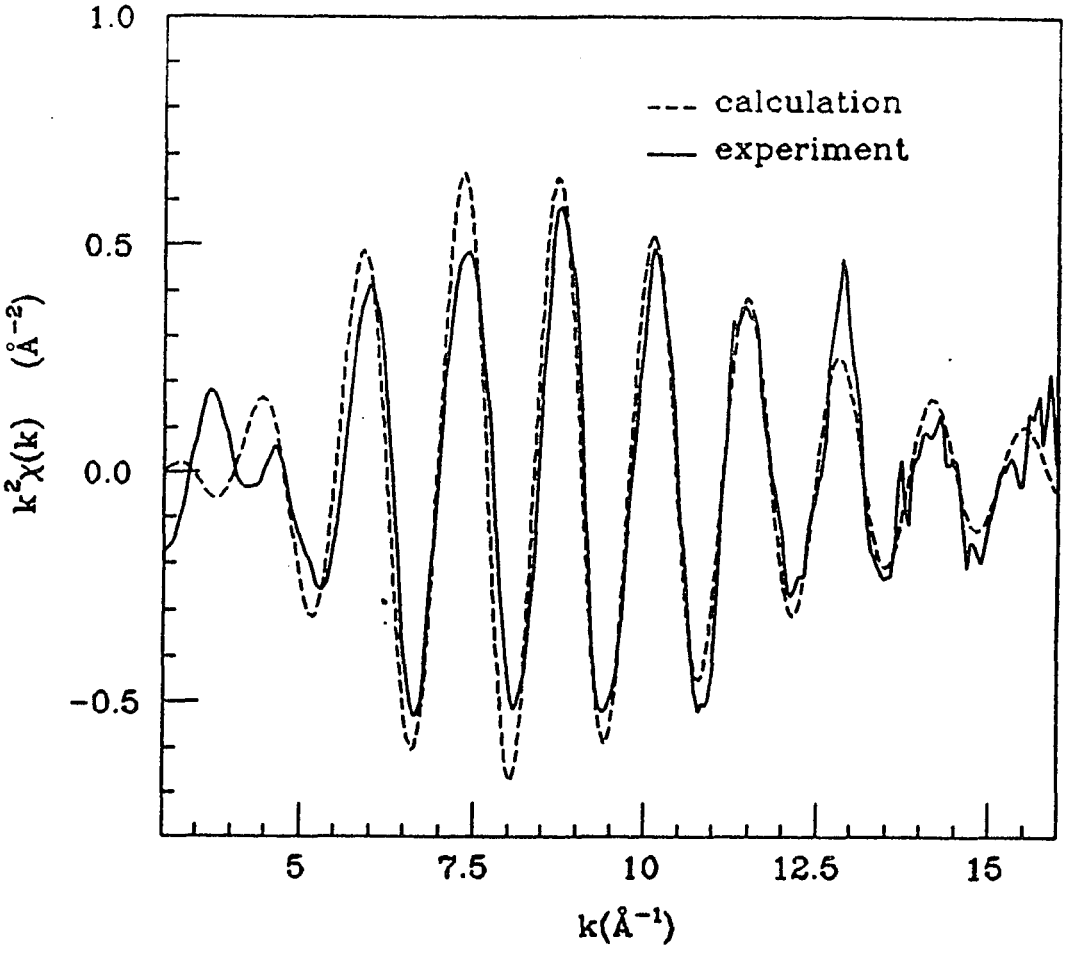

Figure 5.7: $k^2\chi(k)$ of 20 vol.% Sn sample (solid line) compared to the first shell $k^2\chi(k)$ of the calculated ordered 50 at.% SnGe alloy (dashed line).

If filtering can be performed only on one shell, the ratio method [54] is more suitable and sufficient for this comparison. In our case, the curve fitting method was used with appropriate standards. The standards used were, the calculated first shell EXAFS of ordered 50 at.% α-SnGe alloy, the calculated first shell EXAFS of α-Sn, and the measured EXAFS of the β-Sn powder. The latter two standards α-Sn and β-Sn were used to see whether the 20 vol.% Sn sample is actually multi-component due to small contributions from α-Sn and β-Sn which are hidden in the single-shell like sample RDF peak. For the sample and standards, an r-space window between 1.5 and 3.4 Å was chosen for filtering to include the near-neighbor contributions of the possible components while excluding the contributions due to other shells. The upper limit (3.4 Å) was determined by the β-Sn powder. The two close first and second shells in the β-Sn structure are difficult to isolate by filtering, and the filtering window was chosen to include both. Before fitting, the experimental $\chi(k)$ were corrected using McMaster coefficients [79] to account for the fall off of $\mu_0(k)$ past the edge. The maximum amplitude correction at high k (at 16 $Å^{-1}$) was found to be about 9%.

Fitting for 20 vol.% Sn sample was attempted with two different models. The first was a single shell model where first shell EXAFS is assumed to have only Ge near neighbors. The fitting parameters were, the three floating variables N,R, and σ^2 for Sn-Ge neighbors and the discrete variable E_0. The E_0 adjustment was significant especially when fitting theoretical standards with the experimental data (see, table 5.3). Fitting was tested using this model for the first shell EXAFS of the sample obtained at three different temperatures. This way, a higher accuracy in the coordination number could be achieved by minimizing the uncertainty arising from its correlation with the Debye-Waller factor. This model agrees quite well with the experiment indicating that the Sn RDF peak is due to Sn-Ge first near neighbors.

However, the experimental data from XRD and DSC shows that a small amount of β-Sn is present at this concentration. Therefore, in the second model fitting was tried using both Sn-Ge and Sn-Sn bonds. During fitting, sample Sn-Sn neighbors were assumed to have the same bond distance and σ^2 as in the bulk Sn powder. The only additional variable floated during fitting was the number of Sn-Sn bonds, which was 6 for pure β-Sn, since the filtering range chosen included the first two shells. This two shell-model lowered the least square fitting minimum by approximately 20% and improved the fit at low k. Figure 5.8 shows the fitting results obtained at 10 K, 120 K, and 200 K. The fitting parameters obtained at each temperature, using both models are given in table 5.3. For the two-shell fits at 120 K and 200 K, the number of β-Sn near neighbors approaches zero. A possible explanation of the inconsistency is shown in the Figure 5.9, which compares the temperature dependent, (filtered in the k-range, 1.5-3.4 Å) k^2 weighted $\chi(k)$ of β-Sn to that of the 20 vol.% Sn sample. The relatively high reduction in amplitude (higher Debye-Waller factor) of β-Sn at higher temperatures, makes its presence less significant during fitting. Even though the error bar makes the EXAFS result for the inclusion of β-Sn ambiguous, the XRD and DSC data lead us to conclude that the 20 vol.% Sn sample must have a small amount of β-Sn that is quantitatively represented by our result. Both models clearly show that the major contribution to the EXAFS at this concentration comes from Ge near neighbors. In each case, the average Sn-Ge first near neighbor distance was 2.64 ± 0.02 Å, which gives a value of 6.10 ± 0.05 Å as the lattice parameter of the alloy phase. Fits were also made and preliminary results were reported [80], including a small α-Sn contribution. However, the small improvement obtained did not justify its inclusion.

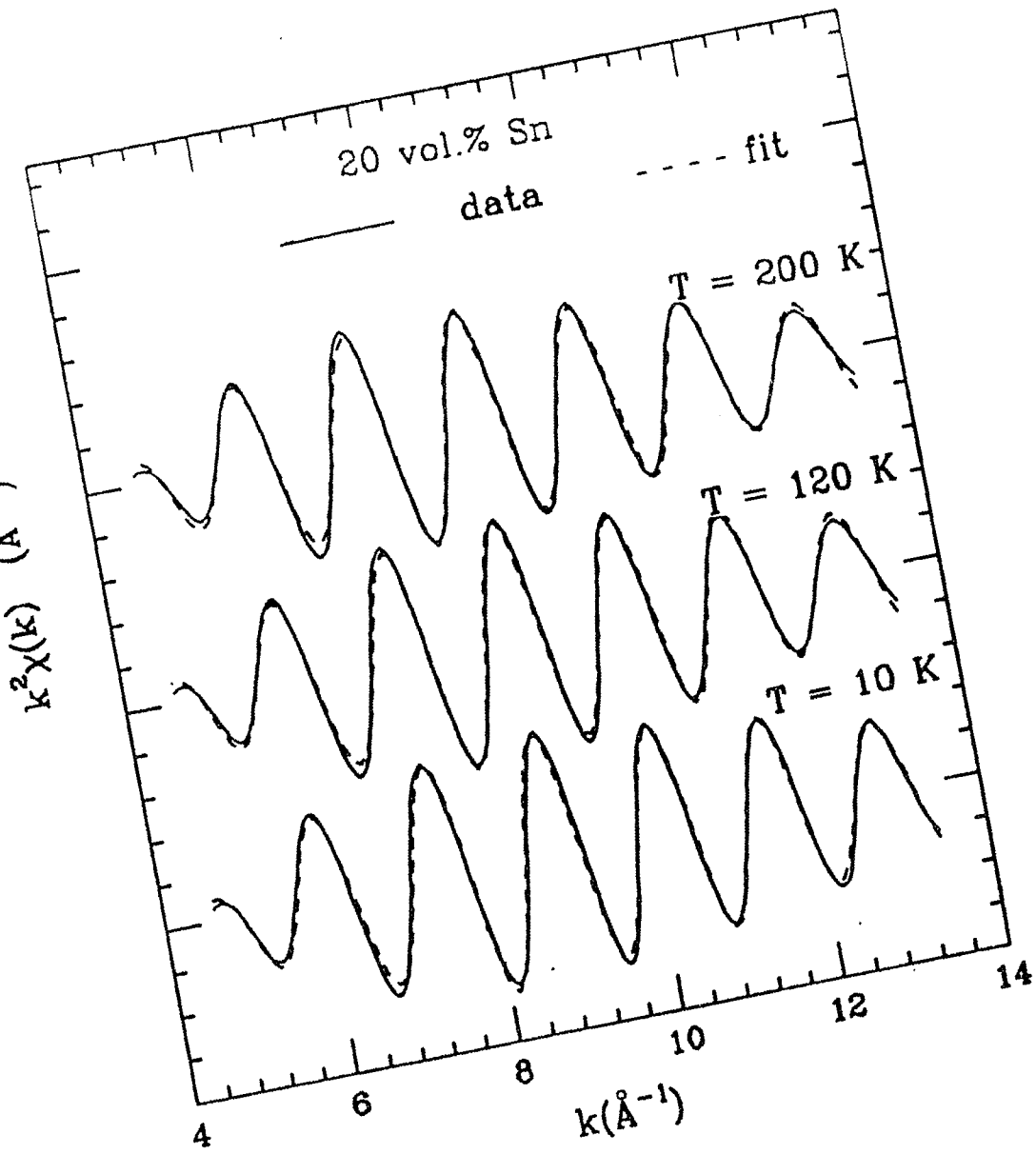

Figure 5.8: Fits (dashed line) obtained for 20 vol.% Sn sample compared to filtered data (solid line) at 10 K, 120 K and 200 K.

Table 5.3 EXAFS results obtained for 20 vol.% Sn sample from (a) the single shell model and (b) two shell model. At 120 K and 200 K N_{Sn-Sn} in the two shell model approaches zero.

(a) Single shell model

Temperature	N_{Sn-Ge}	$\Delta\sigma^2_{Sn-Ge}$ (Å^2)	R_{Sn-Ge} (Å)	E_0 (eV)
10 K	2.48±0.40	0.0031±0.0009	2.64±0.03	-5.5
120 K	2.52±0.40	0.0038±0.0010	2.64±0.03	-5.5
200 K	2.48±0.40	0.0043±0.0012	2.64±0.03	-5.5

(b) Two shell model

Temperature	N_{Sn-Ge}	N_{Sn-Sn}	$\Delta\sigma^2_{Sn-Ge}$ (Å^2)	R_{Sn-Ge} (Å)	E_0 (eV)
10 K	2.56±0.44	0.36±0.48(-.36)	0.0034±0.0015	2.64±0.03	-5.5

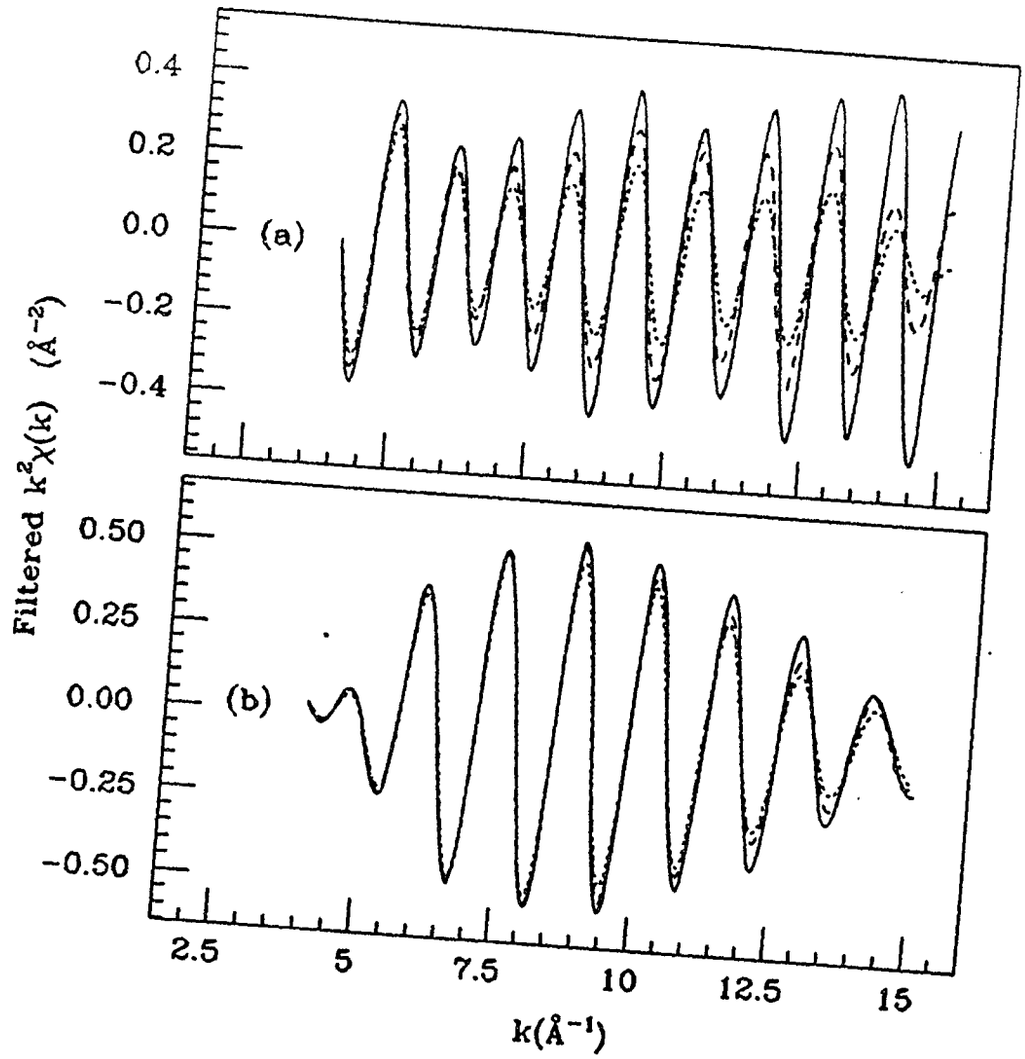

Figure 5.9: Comparison of filtered $k^2\chi(k)$ of 20 vol. % Sn sample to that of Sn powder at 10 K (solid line), 120 K (dashed line) and 200 K (dotted line).

5.1.2 (e) Samples of Higher Sn Concentrations

The 30 vol.% Sn and the 40 vol.% Sn samples can be analyzed in two ways. One way is to repeat the procedure used for the 20 vol.% Sn sample, using the β-Sn powder and the calculated α-SnGe alloy as standards. Another way is to use the 20 vol.% Sn sample as a standard by neglecting the small amount of β-Sn present in the sample and treat the high concentration samples as a mixture of β-Sn powder and an interfacial phase represented by the 20 vol.% Sn sample. We used the second method to analyze the samples of high Sn concentrations, with the initial assumption that the Debye-Waller factors of the samples and near-neighbor distances had not changed with respect to the standards. This way only two variables, number of Sn-Sn and Sn-Ge pairs, were adjusted. Only if the fit was still not satisfactory were the remaining parameters changed. For the 40 vol.% Sn sample a good fit was obtained only by adjusting the number of Sn-Sn and Sn-Ge pairs. For 30 vol.% Sn sample slight changes in σ^2 were required to obtain the best fit. Figure 5.10 illustrates the fitting results obtained for 40 vol.% Sn at 10 K and 120 K. The number of Sn-Ge bonds in these samples were estimated with respect to the fitting result (2.56 Sn-Ge bonds per Sn atom) obtained for the 20 vol.% Sn sample. Table 5.4 shows the fitting results obtained including the 20 vol.% Sn sample.

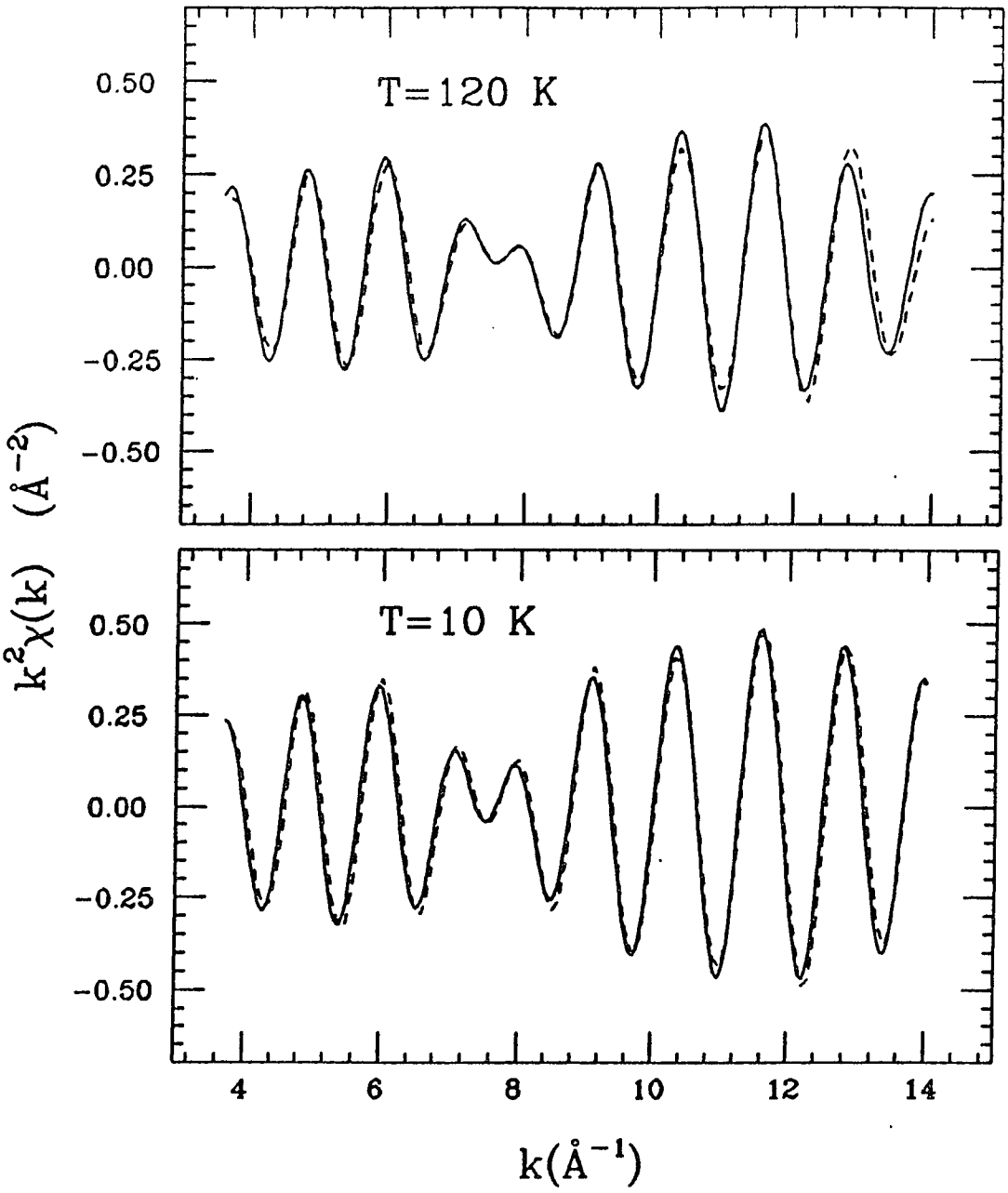

Figure 5.10: Comparison of filtered $k^2\chi(k)$ of 40 vol.% Sn sample data (solid line) to the fits (dashed line) at 10 K and 120 K.

Table 5.4 Variation of amount of Sn-Sn bonds and Sn-Ge bonds with the Sn concentration of the samples. 20 vol.% Sn sample and β-Sn powder were used as standards for fitting samples of higher concentrations.

Temperature	Sample (vol.% Sn)	$N_{Sn\text{-}Ge}$	$N_{Sn\text{-}Sn}$
10 K	40	1.40±0.40	4.80±0.60
10 K	30	2.20±0.40	2.70±0.60
10 K	20	2.56±0.44	0.36+0.48(-0.36)

5.2 Discussion

The XRD, DSC, and EXAFS results in tables 5.1,5.2 and 5.4 are summarized in table 5.5. The results show a systematic variation. The DSC and EXAFS results in columns 3 and 4, respectively, show that as the Sn-Ge phase becomes dominant, the melting enthalpy decreases accordingly. This section attempts to draw a clearer picture of these behaviors.

5.2.1 Lowering of coordination number

According to table 5.3, EXAFS results obtained for 20 vol.% Sn sample shows a reduction of the number of Ge near neighbors (2.56) by about 35% compared to the expected value of four near neighbors for an ordered alloy. My interpretation of this result is the following. As given by Turnbull's model, Sn coats the Ge particles to a certain thickness, and forms an alloy with Ge around the Ge core particles instead of existing as pure Sn in a disordered form. As shown later, this alloy layer is thin and it is likely that the outermost Sn atoms are not fully coordinated. In addition, the lack of significantly higher shell peaks for the 20% sample indicates the high degree of disorder in the alloy layer which could also contribute to lowering the coordination.

5.2.2 Debye-Waller factors and the Einstein model

The root-mean-square displacement or the Debye-Waller factor σ_j^2 determined from EXAFS differs from that obtained by XRD. The latter factor refers to the absolute root-mean-square displacement of an individual atom whereas the EXAFS Debye-Waller factor refers to the relative root-mean-square displacement along the bond direction between the absorbing and backscattering atoms. In EXAFS, the

Table 5.5 Summary of EXAFS, XRD and DSC results from tables 5.1, 5.2 and 5.4.

Vol.% Sn	Avg. Ge particle size D (Å)	Melting enthalpy of Sn (J/g)	% Sn-Ge contribution
40	405 ± 155	48.8	16.4
30	300 ± 95	20.0	32.7
20	250 ± 70	3.6	87.5

correlated motion (low frequency phonons) of an absorbing atom and its neighbor does not contribute to σ^2. The shell to shell variation in σ_j^2 can be described by relating it to the individual motion of the absorbing and scattering atoms with [81]:

$$\sigma_j^2 = \langle [(\boldsymbol{u}_j - \boldsymbol{u}_0) \cdot \hat{\boldsymbol{R}}_j]^2 \rangle, \qquad (5.7)$$

where $\mathbf{u}_j$ and $\mathbf{u}_0$ are the jth atom and central atom displacement vectors, $\mathbf{R}_j$ is a unit vector in the direction $\mathbf{R}_j$-$\mathbf{R}_0$, and the brackets refer to the thermal average. In terms of phonon frequencies ω, σ_j^2 can be expressed as [81]:

$$\sigma_j^2 = \frac{h}{M}\int d\omega \rho_j(\omega) \frac{\coth(h\omega/2k_BT)}{\omega}, \qquad (5.8)$$

where M is the atomic mass, k_B is the Boltzmann constant, and $\rho_j(\omega)$ is the normalized density of modes contributing to relative vibrational motion. For the first shell, the phonon spectrum is dominated by high frequency optical modes, with the frequencies lying in a narrow peak, so that the temperature dependence of σ can be accurately determined by a simple Einstein model of lattice vibrations, assuming that only a single phonon mode with frequency ω_E contributes to $\rho_j(\omega)$ [82]. In the Einstein model the equation 5.2 reduces to:

$$\sigma_j^2 = \frac{h}{M\omega_E}\coth(h\omega_E/2k_BT) \qquad (5.9)$$

where ω_E is the Einstein frequency. We can use the fitting results of temperature dependent EXAFS of the 20 vol.% Sn sample (Table 5.3) to determine the thermal vibrational behavior of the Sn-Ge bonds using equation (5.3) with M replaced by the reduced mass of the Sn-Ge oscillator. A comparison of the calculated results from the Einstein model and the experimental data is shown in Figure 5.11. The corresponding

Einstein temperature $\theta_E = h\omega_E/k_B$, obtained from the fit is 325 ± 29 K. This value is in the range of Einstein temperatures found for tetrahedral semiconductors [83], such as Ge (352 K), GaAs (318 K), and ZnSe (269 K), and is much higher than metallic Sn (150 K). In other words, bonding between Sn and Ge has a strong covalent nature as in semiconductors.

5.2.3 The new SnGe phase and the reduction of melting enthalpy

The Ge-Sn(tetragonal or β-Sn) equilibrium phase diagram is simple eutectic with essentially no solid solubility of Ge in Sn, and less than 1 at.% solubility of Sn in Ge. The above analysis indicates that the alloying between Sn and Ge occurs by interfacial Sn going into the Ge structure substitutionally. The solubility of Sn in Ge at an interface was found to be much higher. At 20 vol.% Sn (16.7 at.%), essentially all the Sn atoms are bonded to the Ge atoms. The physical nature of the two elements (Sn which is ductile and Ge which is brittle) seems to govern the alloying mechanism in the sense that a coating of Sn formed around the freshly exposed surfaces of the Ge particles upon milling causes the subsequent intermixing between Ge and Sn atoms. Analysis also shows that the resulting bonding is semi metallic, and the corresponding bond distance, 2.64 Å, is the average value of the bond distances of Ge (2.47 Å) and α-Sn (2.81 Å). The slight thermal damping in the EXAFS amplitude observed in the temperature dependent EXAFS (Figures 5.4 and 5.9) also agrees with this picture. It also explains the reduction of melting enthalpy of Sn observed through DSC studies. The decreasing β-Sn phase with decreasing Sn concentration leaves the SnGe alloy as the dominant phase. The stability of the alloy phase above the bulk Sn melting point accounts for the reduction of melting enthalpy because only the residual Sn which do not participate in bonding goes through the melting transition. Therefore, ball milling

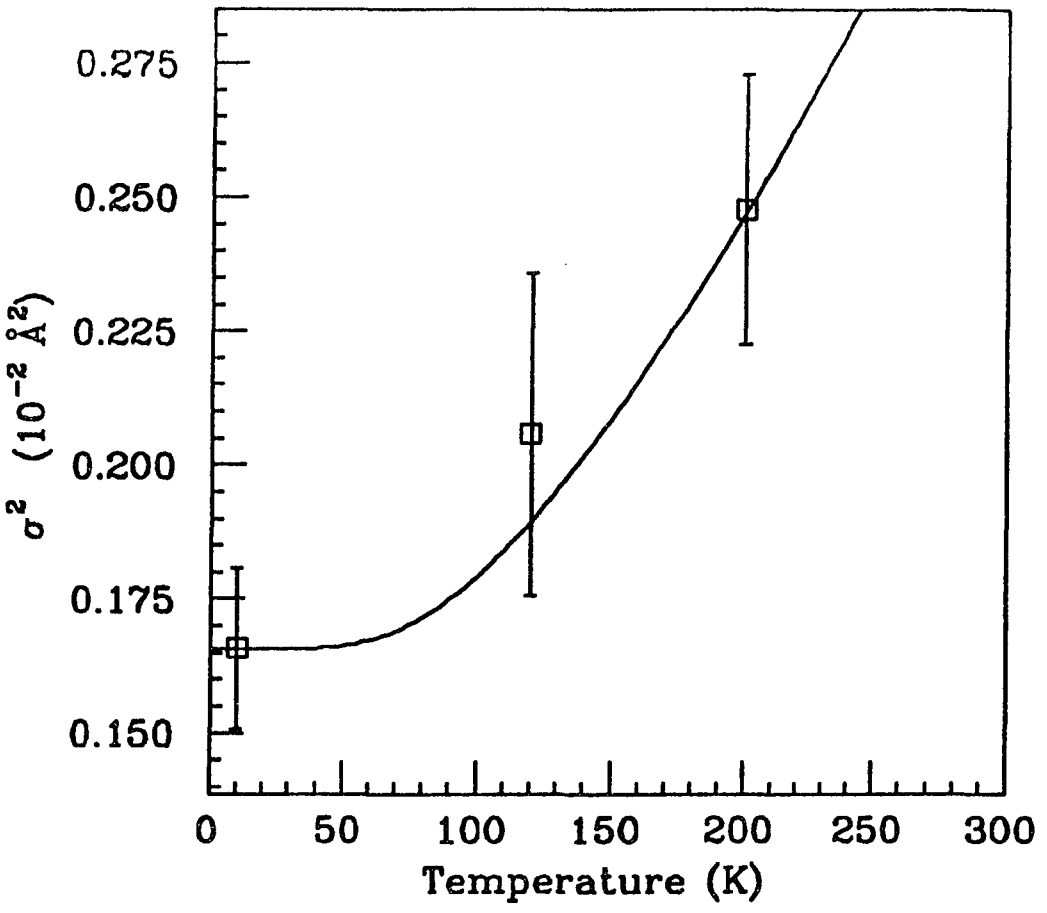

Figure 5.11: Change in Debye-Waller factor as a function of the temperature for the first shell Sn-Ge bonds. The solid line represents the Einstein model calculation.

apparently produces a cubic SnGe alloy having the zinc blend structure.

5.2.4 Thickness estimates of the SnGe alloy phase

The analysis of XRD line broadening shows that the average size of the Ge particles decreases with decreasing Sn concentration, irrespective of the fact that the samples were milled for about the same time. A possible explanation for this behavior is the ductile nature of metallic Sn which acts as a barrier during milling by preventing Ge from further cleavage. We used the particle size and EXAFS results from table 5.1 together to estimate the volume ratio of the alloy phase to excessive Ge (Ge which does not participate in bonding with Sn). The Ge core particles were assumed to be covered uniformly by a 50 at. % SnGe alloy layer to a certain thickness. To estimate the thickness, we used the same assumption as did by Turnbull *et al.*[32], that the Ge particles have cubic shapes with their average diagonal size being represented by the particle size measurements obtained by XRD. The estimated thicknesses are given in table 5.2. At each concentration, the results are consistent with the Ge particles being covered by an alloy layer of almost constant thickness of about 9 Å. (approximately 4 monolayers.) Even though the TEM studies show that the Ge core particles predominately resemble cubes or rectangles, layer thicknesses were estimated also assuming spherical shapes. The obtained average alloy layer thickness was about 15 Å. According to our results, the reaction at the interface includes several monolayers in contrast to Turnbull and co-worker's model which assumes only a single monolayer of disordered Sn at the interface. The decreasing particle size also makes more of the interfacial area available for alloying.

Table 5.6 Estimated thicknesses of the interfacial SnGe alloy layer at each Sn concentration. The Ge particles were assumed to have (a) cubic geometry with the dimension across the cube diagonal and (b) spherical geometry with the dimension across the diameter of the sphere representing the particle size determined by XRD.

Vol. % of Sn	Vol. ratio of $Sn_{.5}Ge_{.5}$/unbonded Ge	Thickness of $Sn_{.5}Ge_{.5}$ interfacial layer(Å)	
		(a) cubic geometry	(b) spherical geometry
40	22.1%	8.0	13.9
30	28.4%	7.5	13.0
20	51.0%	10.6	18.4

5.2.5 Composition of the Alloy

The consistency of the results discussed above indicates that the assumption of the 50/50 atomic ratio is reasonable. This assumption is also supported by the fact that α-SnGe alloys epitaxially grown on Ge(100) substrates have a preferred composition of approximately 50 at.% [34]. Bowman *et al.* [37] have estimated the lattice parameters of α-SnGe alloy grown epitaxially on CdTe substrates for lower Ge concentrations. The variation of lattice constant with the atomic concentration seems to follow a linear relationship. Extrapolation of these results gives a value of 6.15 Å for the lattice constant of a 50 at.% α-SnGe alloy which is in good agreement with our result (6.10 $\pm$ .05 (Å)). Further, the ^{119}Sn Mossbauer spectroscopic studies made on the milled Sn-Ge powders by Boolchand and Koch [84] gave results agreeing with our results. These studies revealed two sites corresponding to tetragonal β-Sn and a site where Sn is tetrahedrally coordinated to four Ge near neighbors. With lowering Sn concentration the tetrahedral site is observed to be the dominant site.

5.2.6 Melting point depression of Sn

As discussed in section 1.3.1, the depression of the melting point of solids is interpreted using various mechanisms. Particularly, the mechanisms of melting which is thought to start from the interfaces of systems such as Pb-Ge and Sn-Ge, are based on speculations which go along with the experimental observations. Koch *et al.* related the melting point depression of Sn in the milled Sn/Ge powder system to a vibrational instability induced at the Ge/Sn interface. Results show that as the Sn concentration is lowered the particle size decreases consequently causing the interface/volume ratio to increase. The tailing and broadening in the Sn melting transition region also

increases accordingly. Therefore, it is possible that the Ge/Sn interface plays a role in the melting point depression of Sn. However, the size effect cannot be ruled out which explains the melting point depression of metals such as Sn. Through the series of papers [20-27], discussed in section in section 1.3.1 it is fairly well established that as the particle sizes reach the nanometer scale the metals melt at temperatures lower than the bulk melting point. The range of depression depends on the type of the element and, for Au, the particles with diameter of 20 Å melt at a temperature as low as 600 K [24]. (The bulk melting point of Au is 1337.6 K.)

OUR study showed that only the residual Sn goes through the melting transition around the bulk melting point of Sn. It is interesting to see how this residual Sn exists in the samples. It is reasonable to assume that after extensive milling, the residual Sn is distributed in the sample as aggregates of small particles among the Ge particles covered by the SnGe alloy phase. Also, the sizes of Ge particle at each concentration lead us to assume that the residual Sn particles can have sizes ranging from a few tens to a few hundreds of angstroms, depending on the Sn concentration. Figure 5.12 (data were extracted from reference [22]) shows the variation of melting point of Sn with particle size as observed from electron diffraction for Sn films evaporated on carbon substrates. When the particles are about 100 Å, the associated depression of melting point is about 25 °C, which is in the range of the depression observed by Koch *et al.* Thus, the simplest explanation is that small Sn particles are the likely cause of the melting point depression of Sn in the milled Sn-Ge system.

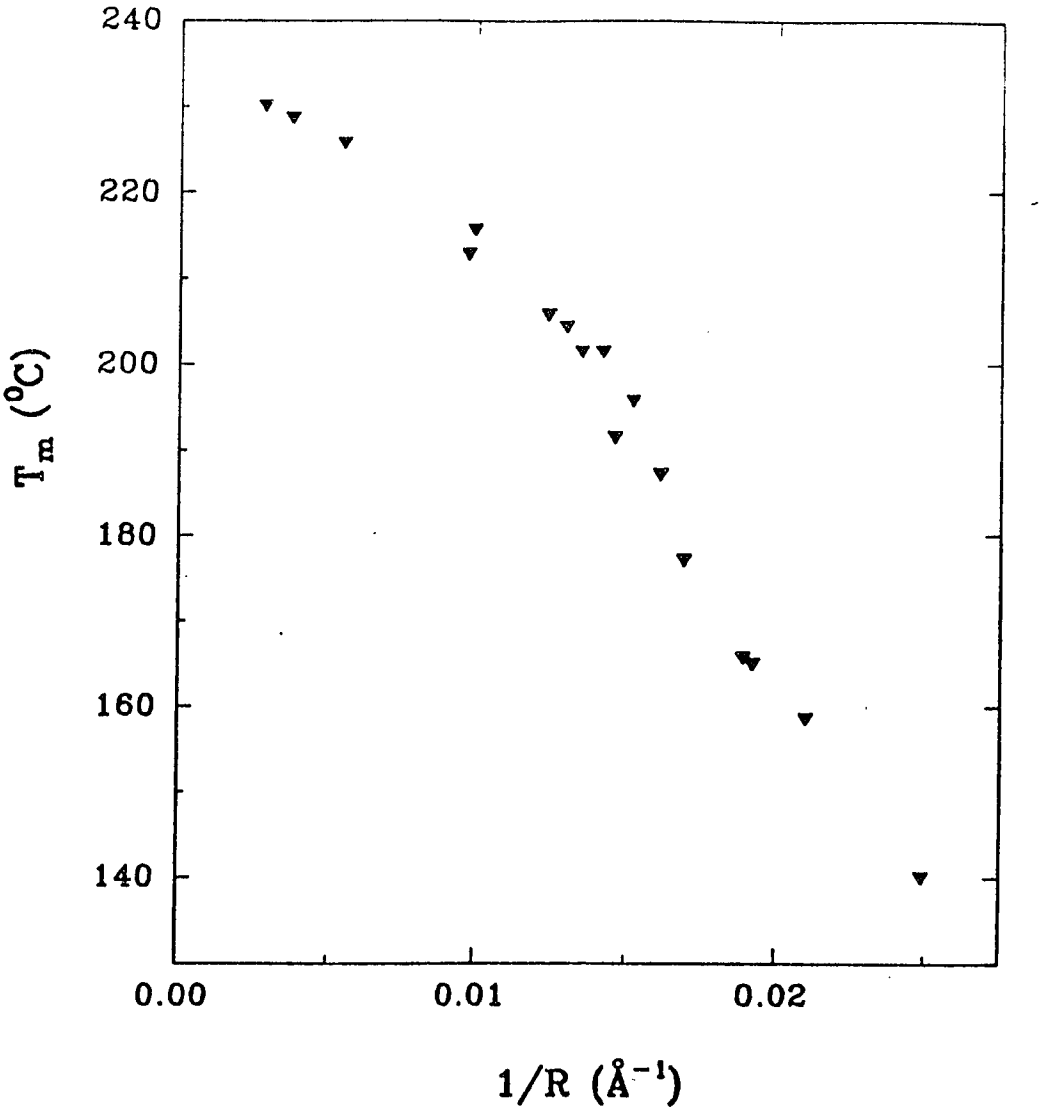

Figure 5.12: Variation of the Sn melting point with the Sn particle size. Results are based on electron diffraction measurements done on Sn films evaporated on carbon substrates. (data were extracted from reference [22].)

5.3 Conclusions

The experimental results obtained for the ball milled Sn-Ge powders, by EXAFS, XRD, and DSC are consistent with the fact that alloying between Sn and Ge occurs at the Sn/Ge interface. The alloy is found to be 50 at.% cubic with zinc blend structure and is stable above the melting point of tetragonal bulk Sn. Therefore the formation of this alloy is also consistent with the compositional dependence of melting enthalpy of these Sn-Ge powders. The milling also causes the alloying to occur within a few monolayers at the interface. Our analysis does not directly explain the melting point depression of Sn in these samples. However the particle size of the residual Sn in the samples could be the likely cause for this behavior.

Chapter 6

Sn-Si System

The data analysis for the Sn-Si system is a repetition of the procedure we discussed for the Sn-Ge system. Therefore, this section discusses the results more briefly, while making comparisons to the Sn-Ge system, wherever necessary.

Figure 6.1 shows the k^2 weighted $\chi(k)$ for the 40 vol.% Sn (in Si) and 10 vol.% Sn (in Si) samples compared to that of Sn powder. The changes are not as quite dramatic as compared to the changes in Sn-Ge system. However at 10 vol.% Sn the changes are clearer. Figure 6.2 shows the EXAFS RDF (transformed in the range, 3.4 to 16.6 $Å^{-1}$) of the 10 vol.% Sn sample. The peak at 2.0 Å is due to bonding between Sn and Si first near neighbors.

The quantitative EXAFS analysis in this case was done on the 10 vol.% Sn sample where there is a significant amount of bonding between Sn and Si. Taking into consideration the possible overlapping between Sn-Sn and Sn-Si first shell RDFs, the data were filtered in the range 1.2-3.35 Å, for fitting. As standards, Sn powder and calculated EXAFS of a 50 at.% Sn-Si alloy (see, dotted line in Figure 6.2) were used. For the calculation, an approach similar to that applied in the Sn-Ge system was used. Fitting was attempted by floating the number of Sn-Sn pairs and Sn-Si pairs initially. However, slight changes in the Sn-Sn bond distance and the Debye-Waller factor were required to obtain good fits. Figure 6.3 shows the fits obtained at each temperature and the corresponding results are given in Table 6.1. The average Sn-Si bond distance, 2.58 Å, is between that of Si-Si (2.35 Å) and Sn-Sn (2.81 Å) in the cubic phase (α-Sn). The Debye-Waller factor results of the Sn-Si bond gives an Einstein

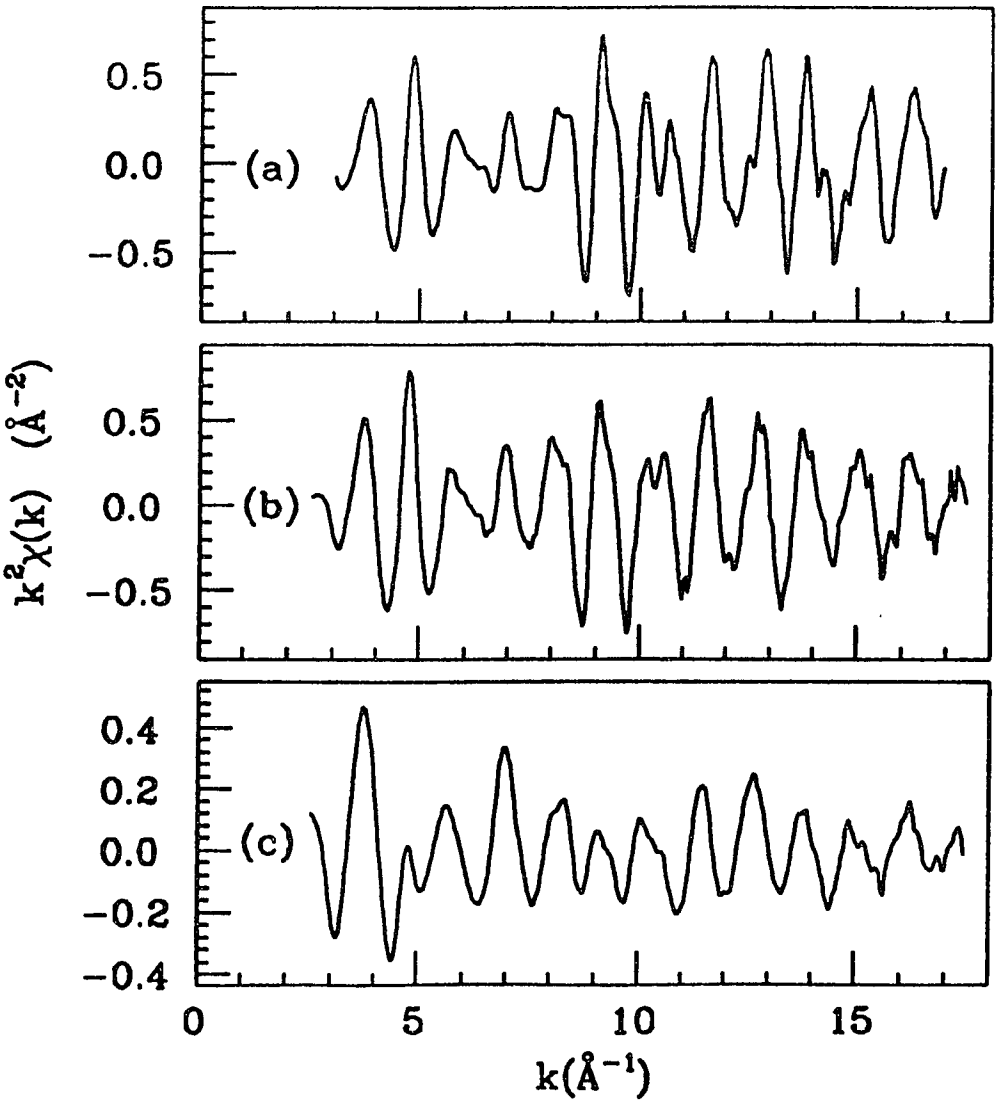

Figure 6.1: k^2 weighted $\chi(k)$ of Sn K-edge measured at 10 K for samples (a) Sn powder (b) 40 vol.% Sn (in Si) and (c) 10 vol.% Sn (in Si).

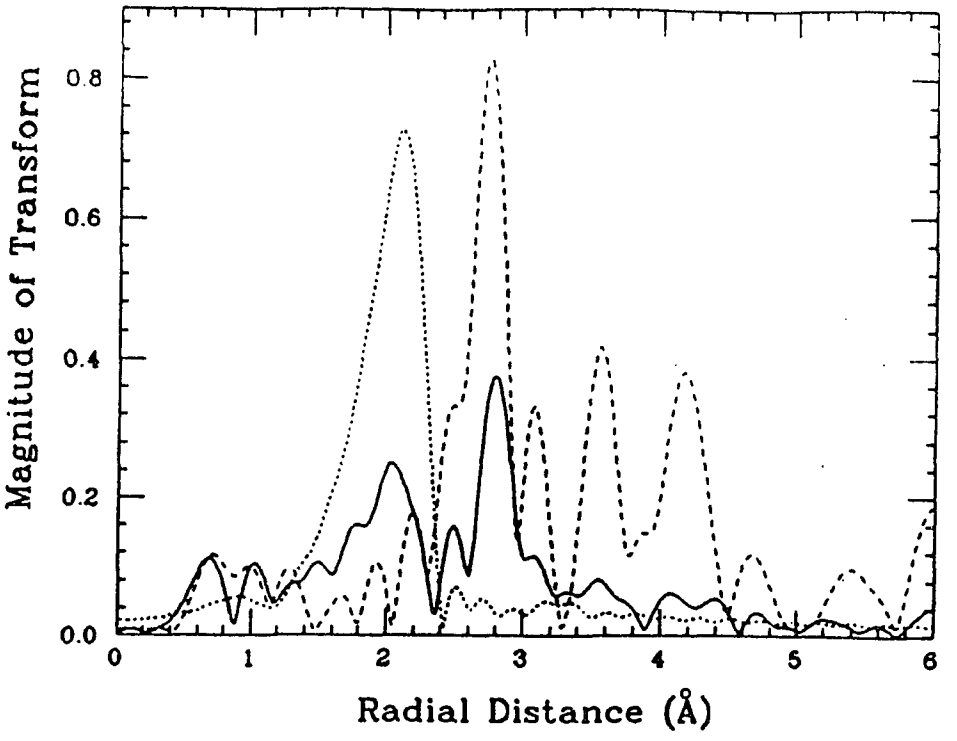

Figure 6.2: Fourier transforms of EXAFS $k^2\chi(k)$ data of 10 vol.% Sn sample (solid line) compared to that of Sn powder (dashed line) and calculated 50 at.% SnSi alloy (dotted line).

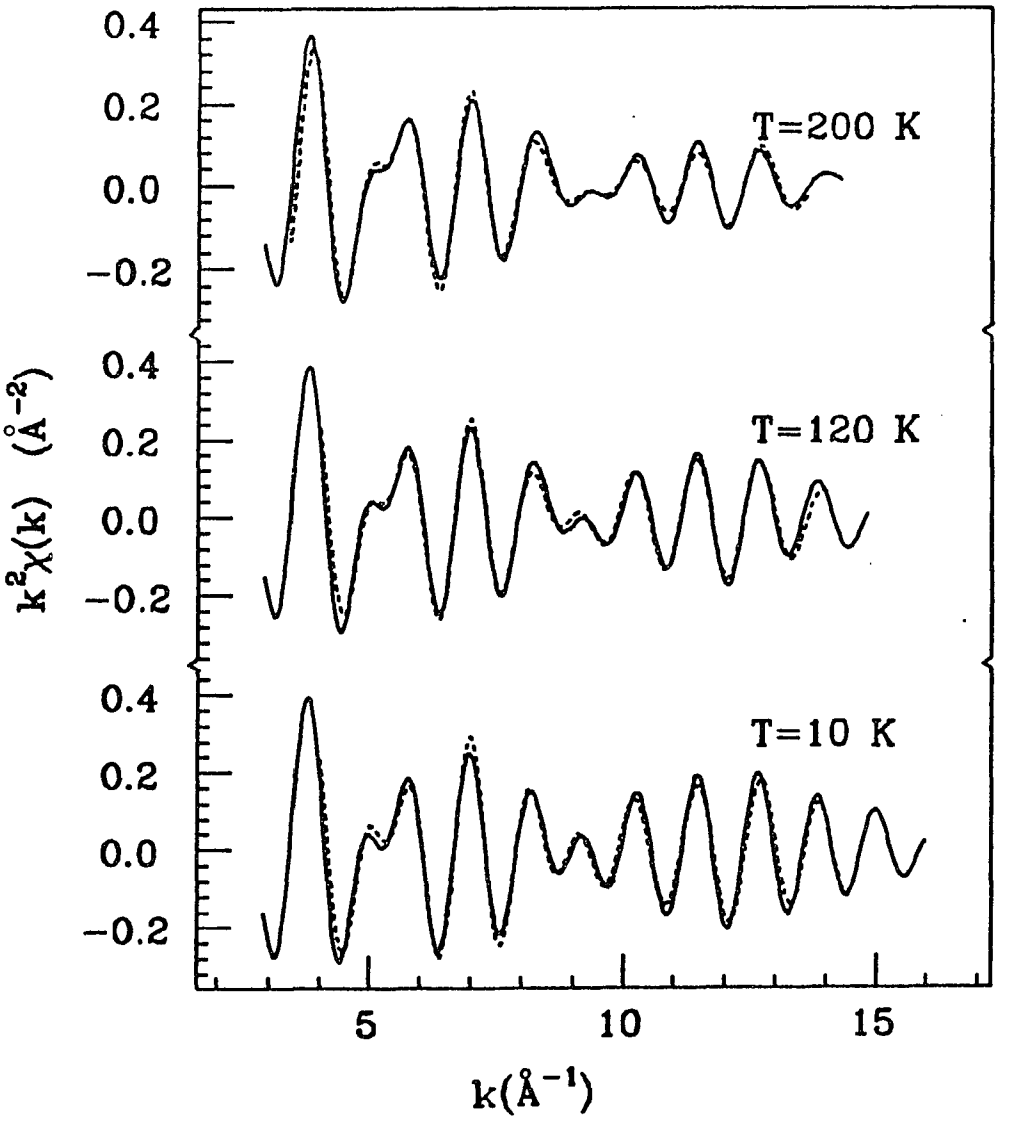

Figure 6.3: Fits (dashed line) obtained for the 10 vol.% Sn (in Si) sample (solid line) at 10 K, 120 K and 200 K.

Table 6.1 EXAFS fitting results obtained for 10 vol.% Sn (Si) sample at each temperature.

T(K)	% N_{Sn-Si}	$\Delta\sigma^2_{Sn-Si}$ ($Å^2$)	R_{Sn-Si} (Å)	% N_{Sn-Sn}	$\Delta\sigma^2_{Sn-Sn}$ ($Å^2$)	$E_{0(Sn-Si)}$ (eV)	$E_{0(Sn-Sn)}$ (eV)
10	29.0±3.0	.0039±.0010	2.59±.02	71.0±3.0	.0012±.0010	-6.0	-2.5
120	27.7±3.0	.0040±.0015	2.59±.02	72.3±3.0	.0017±.0010	-4.0	-2.5
200	27.0±3.0	.0054±.0020	2.59±.02	73.0±3.0	.0024±.0010	-4.0	-3.0

temperature of 351 $\pm$ 37 K, indicating that the bonding was strongly covalent, agreeing with the Sn-Ge system.

The x-ray diffraction data also shows a trend similar to Sn-Ge system in the sense that the Si diffraction line broadening occurs as the Sn concentration is lowered (see Figure 6.4). Measurements of the Si particle size, using the formalism described in section 5.1.1 are given in Table 6.2. The EXAFS and XRD results show that the alloying extends up to about 1-2 Å at the interface. The interface alloying between Si and Sn is clearly less extensive than that between Sn and Ge, which is attributed to the higher lattice mismatch between Sn and Si (14.3% for Sn-Ge and 20% for Sn-Si).

The Sn-Ge and Sn-Si systems both demonstrate that the ball milling method can be applied to two components, one which is ductile and the other brittle, to achieve an interface where the brittle component is coated by the ductile component. Whether there is an interfacial reaction may be governed by the chemical nature of the components and the thermodynamic conditions at the interface. For example, when this method was applied to two components Pt and SiO_2, which are important from the catalytic point of view, no intermixing was observed but the Pt was highly dispersed on the surface of SiO_2 particles [85]. The particles were comparable to industrial grade metal supporting catalysts indicating that the ball milling method is a potential candidate for producing catalytic materials.

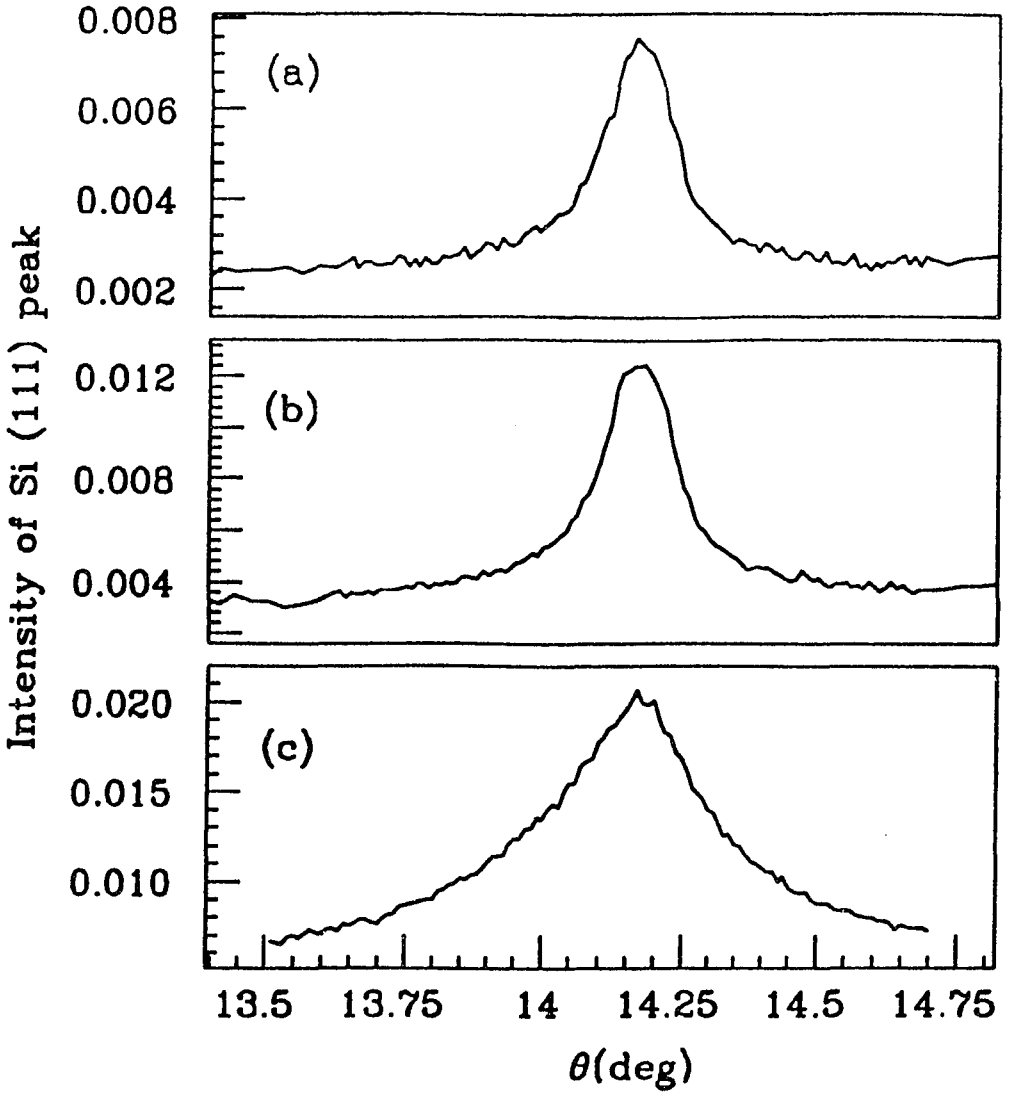

Figure 6.4: Si(111) XRD profile of (a) 40 vol.% Sn (b) 25 vol. Sn and (c) 10 vol.% Sn (in Si) samples.

Table 6.2 Average particle size of Si powders determined by analyzing Si(111) diffraction profile using equation 5.3.

Sample (vol.% of Sn)	Average Si particle size D(Å)
40	795
25	639
10	170

Chapter 7

Summary

The aim of this thesis was to investigate three interesting solid interfaces using mainly synchrotron radiation assisted x-ray techniques. The importance of a non-destructive technique like x-ray reflectivity to study the morphology of Si/SiO_2 thin films was demonstrated while comparing the oxides deposited thermally and using the PECVD method. The design of the x-ray reflectivity apparatus using a two detector system allowed acquisition of data with a data of a large angular range in which the reflected signal varies by 5-6 orders of magnitude. The results show the high quality of both thermally grown and low temperature, PECVD deposited silicon dioxides. The reflectivity technique allows determination of parameters such as density relative to the substrate. Since the density of crystalline silicon is known, the absolute densities of the silicon dioxides can be obtained. The interface roughness of the PECVD grown Si/SiO_2 interface is higher compared to its thermally grown counterpart. Therefore, further improvement is necessary to make the PECVD method more useful for SiO_2 film processing.

The study also showed the sensitivity of the technique to thin buried oxide layers near the interface. In fact, simulations showed that the reflectivity is sensitive to thin buried layers located anywhere in the oxide film, provided there is a significant density step. The rms roughness values obtained for thermally grown SiO_2-Si films agree with the existence of a thin (5-10 Å) transition layer at the Si/SiO_2 interface. The results do not show the presence of a 30-50 Å thick Si rich compressed oxide layer as observed by some other techniques. However, our interface picture cannot

be generalized to all thermally grown Si/SiO_2 interfaces because the properties of the interface could depend on the substrate processing methods etc. One way to clarify the issue is to study oxides which are thought to have a thicker transition layer consisting of sub oxides to see whether there is a limitation in the reflectivity technique.

The Sn-Ge system was investigated to obtain a clearer picture of the previously observed melting point depression of Sn and the reduction of melting enthalpy with decreasing Sn concentration. The experiments were planned in two different ways. X-ray reflectivity was used to see whether the melting of Sn initiates from the Sn/Ge interface. Attempts were made to deposit Sn/Ge and Sn/Al multilayers. The sensitivity of the Bragg peaks in the x-ray reflectivity of multilayers to the volume change that Sn undergoes during melting was selected as the probe of melting. However, due to difficulties encountered during the sample preparation the experiment was not successful.

In the second experiment, the ball milled Sn-Ge powders were examined using EXAFS and x-ray diffraction. Powders of varying Sn concentrations were ball milled in an Ar atmosphere. The Sn K-edge EXAFS and XRD measurements showed systematic variations with decreasing Sn concentration. EXAFS clearly showed the change in the near neighbor environment of Sn with lowering of the Sn concentration. Analysis showed that the changes were due to the bonding of interfacial Sn to Ge. When the Sn concentration is approximately 20 vol.% essentially all the Sn participated in bonding with Ge. The solubility of Sn in Ge according to the bulk phase diagram is less than 1 at.%. and our study showed that the solubility of Sn in Ge at the interface is much higher. The Sn coating formed around the Ge particles upon milling seemed to have caused intermixing of Sn and Ge. The variation of the

EXAFS Debye-Waller factor with temperature was used to study the nature of bonding between Sn and Ge. The Debye-Waller factors in the Sn-Ge first shell were fit with a simple Einstein model. The corresponding Einstein temperature (329 K) was in the range of tetrahedral semiconductors and much higher than that of metallic Sn (150 K), indicating that the Sn-Ge bond is strongly covalent. Alloying seems to happen by interfacial Sn going into the cubic Ge structure. The reaction at the interface was found to extend up to about four monolayers at each concentration. The consistency of the results agreed with the assumption that the alloy has 50:50 atomic composition suggesting that the alloy has a zinc blende structure. The reports of the existence of the metastable SnGe alloy epitaxially grown at 400°, with a preferred composition of $\sim$50 at.%, lead us to assume that a 50 at.% cubic SnGe alloy forms at the Sn/Ge interface.

The stability of the alloy above the melting point of bulk Sn (tetragonal Sn) explains the reduction of melting enthalpy as the Sn concentration was lowered. Because the Sn bonded to interfacial Ge is stable, only the bulk metallic Sn phase accounts for the melting transition, causing melting enthalpy to vanish at a concentration when all the Sn participates in bonding with Ge. The previously observed melting point depression of Sn in these ball milled powders cannot be directly explained based on our analysis. However the particle size of the residual bulk Sn may have been the possible cause.

We extended our study to ball milled Sn-Si to see whether there is the same interfacial alloying even though no epitaxially grown thin film structures have been reported. Samples of varying Sn concentrations were measured using EXAFS (Sn K-edge) and XRD. Systematic changes similar to, but not as quite dramatic as those in the Sn-Ge system were observed. At 10 vol.% Sn concentration the extent of alloying

was reasonably significant. Analysis showed that the bonding between Sn and Si is strongly covalent with an Einstein temperature of 350 K. However, the reaction at the interface was limited up to about 2 Å (close to a monolayer) which was attributed to the higher lattice mismatch between Sn and Si.

Appendix

An important part of the reflectivity data collection is the alignment of the goniometer and the sample. Before going through the alignment procedure it is useful to identify the parts of the goniometer which are important during the alignment (see, Figure A.1, see, Figure 3.2 also.). While widths of the slits S_3 and S_4 can be changed, the overall positions of the slits with respect to the arms can also be adjusted, in a direction perpendicular to the line joining the slits, using the screws denoted by P. The sample block mounting stage is attached to the circular rotating base (θ base) which controls the sample rotation. The sample block mounting stage is designed such that a pin, which is necessary for the alignment, can be mounted at the center of the stage. The stage can also be moved to adjust the pin position with respect to the slits.

1. Goniometer Alignment

The alignment of the goniometer is a two step procedure. The first step is to make sure that the center of rotation of the sample coincides with that of the rotating arm. The following procedure was used to check this alignment and could be done outside the experimental hutch.

(a) Viewing through a telescope [goniometer is leveled using the slit (S_3) center of the fixed arm as the reference point.], the pin is brought over to the line joining the centers of the slits S_3 and S_4.

(b) The θ base is rotated by 180 degrees to check whether the pin can still be seen at the center of the two slits. If the pin is off centered, the position of the slit S_4 is adjusted using screw P so that the pin and the two slit centers coincide with each other.

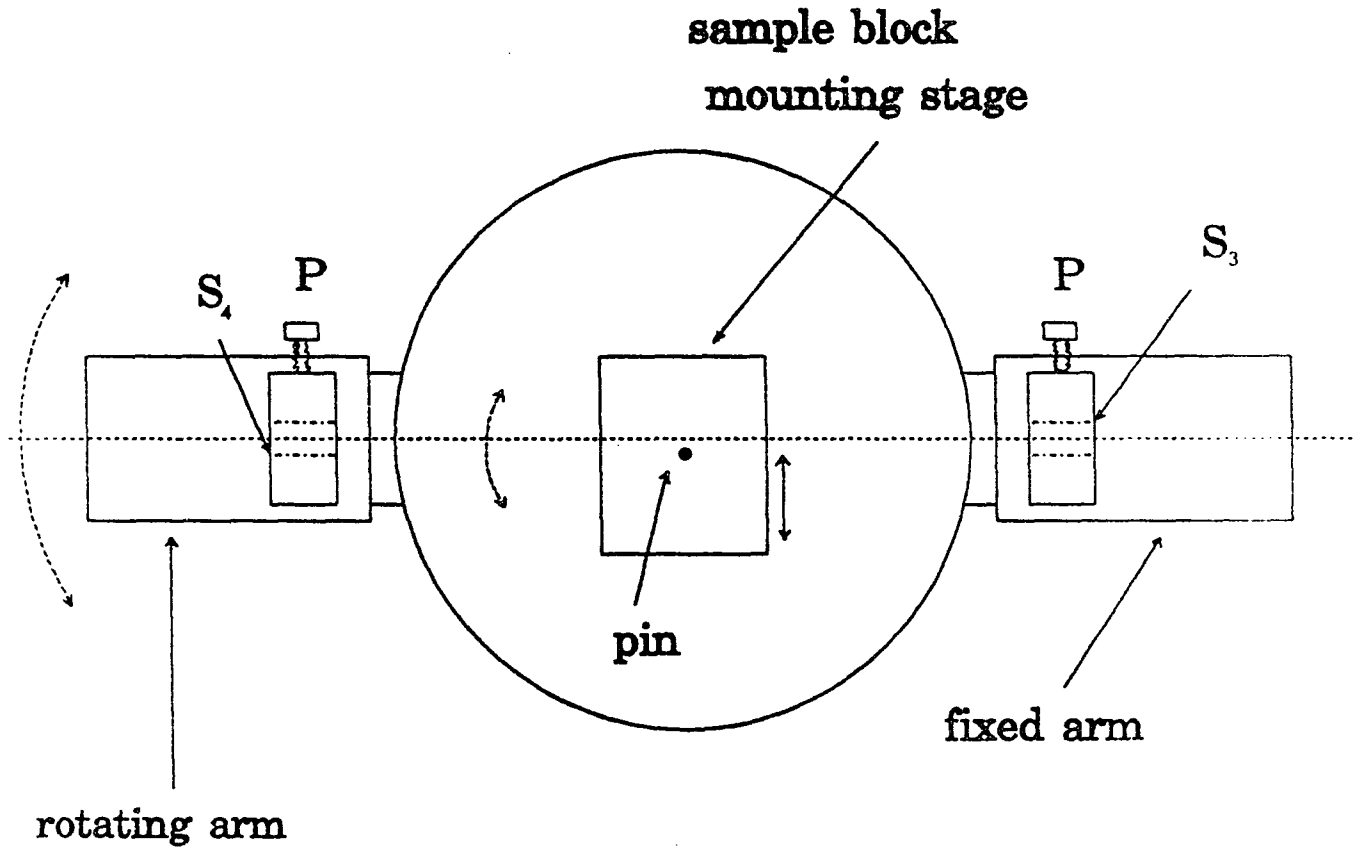

Figure A.1: Schematic of the goniometer with the alignment pin mounted on the sample block mounting stage.

(c) The θ base is rotated back by 180 degrees to its initial position to check the alignment. If the three elements, the two slit centers and the pin are misaligned, the pin position is adjusted to bring it over to the line joining the slit centers.

This procedure is repeated alternatively rotating the θ base until the slit centers and the pin lies on a straight line at which point two centers of rotation coincide with one another. Repetition of this alignment is not required unless the slit positions are changed.

Next step of the alignment is done as follows after the goniometer is mounted on the experimental hutch. (Every time when the goniometer is mounted one has to go through this alignment procedure.)

(a) The alignment pin is replaced by the sample mounting block, and the goniometer is placed such that S_3, and S_4 are in the direction of the incoming beam and the plane of rotation of the sample and the detector arm is vertical. The height of the slit S_3 is initially adjusted manually, by eye estimation such that it is at the same level as S_2 the hutch slit (Figure 3.2).

(b) Goniometer is leveled parallel and perpendicular to the beam using same reference as for previous alignment using a precision level. The goal is to align the planes of the slits and the sample surface (at $\theta = 0$ position) so that they are in the plane of the incident beam.

(c) Leaving S_4 opened wide, and S_3 at about .2 mm, the goniometer height is accurately adjusted using a computer controlled motor so that the actual beam gives maximum intensity when entering S_3.

(d) Slit S_3 is set at the desired beam width and the hutch slit S_2 is adjusted to the same

width by monitoring the transmitted beam. Typically beam heights of 50-100 microns are used. Slit S_3 is then opened to about 100 microns larger to ensure the entire beam detected by I_0 passes through.

2. Sample Alignment

(a) Mount the sample on the sample mounting block and move the block down so that the incident beam directly enters the detector through slit S_4. (see, Figure A.2) Narrow the slit S_4 so that it is slightly wider than S_3.

(b) Scan the detector through the incident beam to calibrate the 2θ angle (normally referred to as zero angle scan.)

(c) Calibrate $2\theta = 0$ position, using the midpoint of the intensity profile, obtained averaging the midpoints at several intensities (see, Figure A.3 (a).).

(d) Raise the sample to a position where it cuts down the incident beam intensity by 50%. (The half intensity point.) Due to the fact that the beam is not parallel to the sample plane, this may not be the true half intensity point.

(e) Rotate the sample to a small angle (normally, $\theta = 0.3°$) and scan 2θ arm around the reflected beam (for example, if $\theta = 0.3°$, 2θ is scanned in the range from .5° to .7°.). Calibrate θ using the averaged midpoints of the reflection profile. (see, Figure A.3 (b).)

(f) Repeat steps (d) and (e) until convergence. Generally the initial iterations are done manually until the sample is approximately aligned, then a motor scan is made. Typical alignment errors are approximately 0.001° for samples with sharp and symmetric reflectivity profiles.

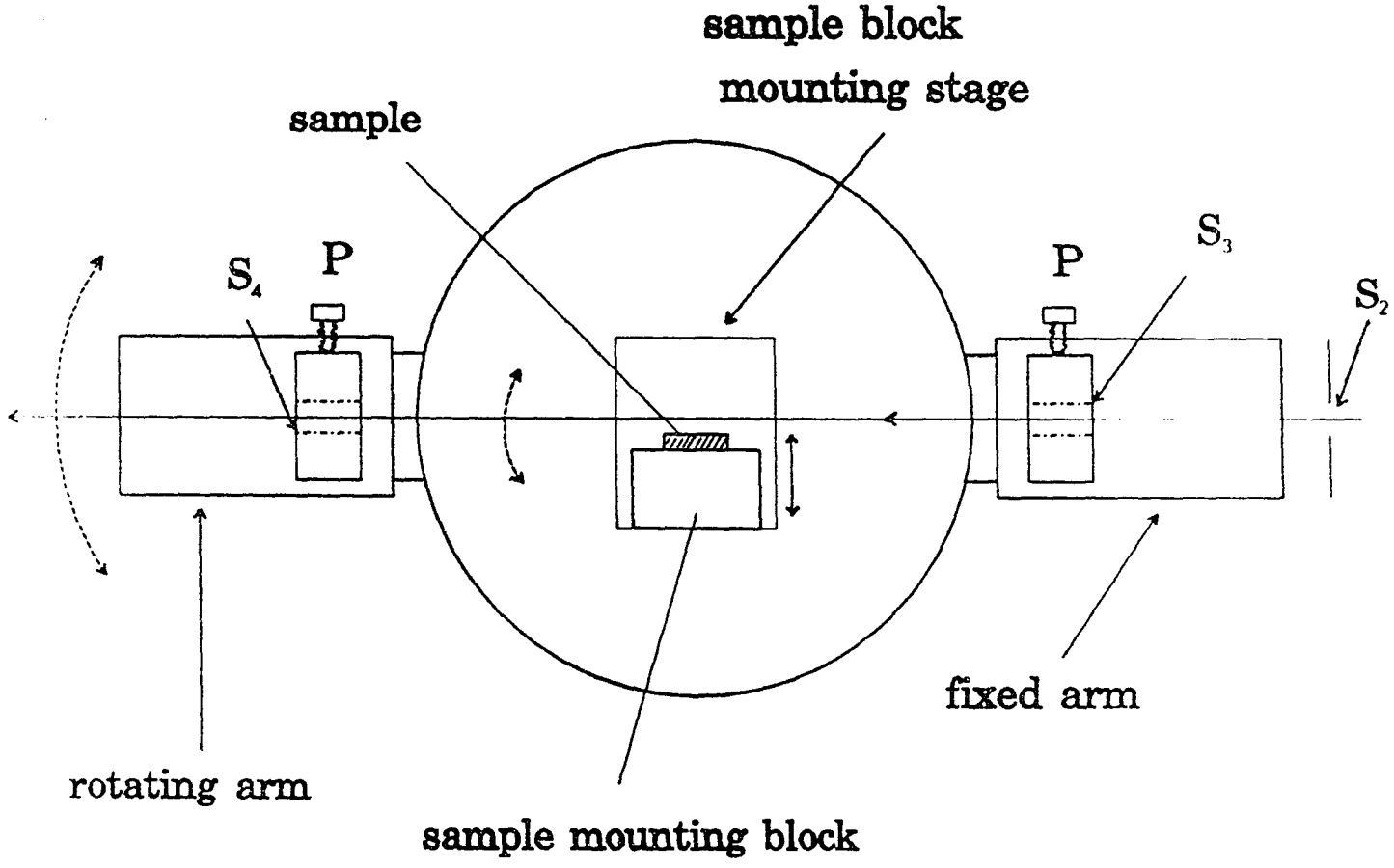

Figure A.2: Schematic of the goniometer with the alignment pin replaced by the sample mounting block.

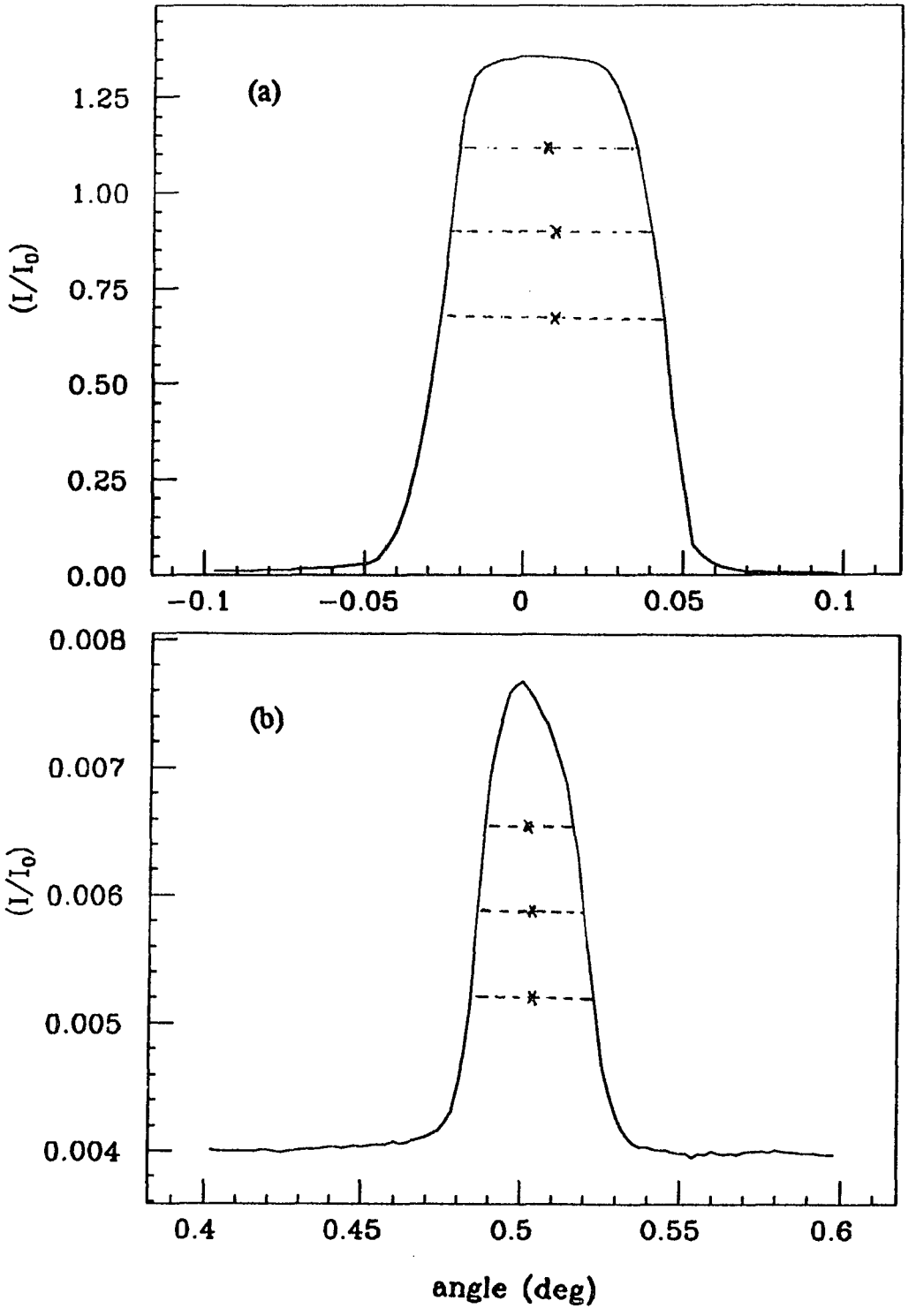

Figure A.3: (a) Incident beam profile obtained by making a 2θ scan, with the sample stage moved away from the beam. 2θ angle is calibrated by using the average value of the midpoints at several intensities. (b) A scan obtained to calibrate the θ rotation (θ scan).

note: The alignment of the sample perpendicular to the beam direction is important especially for small samples. For the large flat samples used in this work, this alignment was not important.

Bibliography

[1] D.Wolf *et al.*, A.J.Freeman *et al.*, B.N.Engel *et al.*, I.K.Robinson and A.Ourmazd; in MRS Bulletin **15**, (1990) and references quoted therein.

[2] G.S.Oehrlein, J.C.Bean, F.J.Feigl, P.B.Ghate and L.F.Eastman; in Physics Today, **39**, No.10, (1986) and references quoted therein.

[3] C.R.M.Grovenor, *Microelectronic Materials*, (Adam Hilger, Bristol and Philadelphia, 1989).

[4] F.J.Feigl, Physics Today, **39**, No.10, 47 (1986).

[5] E.A.Irene, D.W.Dong and R.J.Zeto, J. Electrochem. Soc. **127**, 396 (1980).

[6] A.C.Adams,Solid State Technol.**26**, 135 (1983).

[7] J.R.Hollahan, J.Electrochem. Soc. **126**, 933 (1979).

[8] G.Luckovsky, P.D.Richard,D.V.Tsu,S.Y.Lin, and R.J.Markunas, J.Vac.Sci.Technol.A **4**, 681 (1986).

[9] J.Batey and E.Tierney, J.Appl.Phys.**60**,3136 (1986).

[10] P.J.Shultz and K.G.Lynn, *Rev. Mod. Phys*, **60**,701 (1988).

[11] P.Asoka-Kumar,K.G.Lynn,T.C.Leung,B.Nielsen,G.W.Rubloff and Z.Weinberg,Phys.Rev.B. **44**, 5885 (1991).

[12] P.Asoka-Kumar,K.G.Lynn,T.C.Leung,B.Nielsen and X.Y.Wu, J.Appl.Phys.**69**, 6603 (1991).

[13] R.A.Cowley and T.W.Ryan, J.Phys.D **20**, 61 (1987).

[14] C.C. Koch, J.S.C. Jang and S.S. Gross, J. Mater. Res., **4**, 557 (1989).

[15] J.S.C. Jang, C.C. Koch, J. Mater. Res., **5**, 325 (1990)

[16] R.M.J.Cotterill, J.Cryst.Growth **48**, 582 (1980).

[17] R.W.Cahn, *Nature*, **273**, 491 (1978).

[18] L.L.Boyer,Phase Transitions **5**, 1 (1985).

[19] P.R.Couchman and W.A.Jesser, Phil.Mag.**35**, 787 (1976).

[20] M.Takagi, J.Phys.Soc.Japan,**9**,359 (1954).

[21] M.Blackman and A.E.Curzon, *Structure & Properties of Thin Films*,

[22] C.R.M. Wronsky, Brit.J.Appl.Phys,**18**, 1731 (1967).

[23] J.R.Sambles, Proc.R.Soc.Lond.A.**324**, 339 (1971).

[24] Ph.Buffat and J.P.Borel, Phys.Rev.A, **13**, 2287 (1976).

[25] R.P.Berman and A.E.Curzon, Can. J. Phys.**52**, 923 (1974).

[26] S.J.Peppiatt,Proc.R.Soc.Lond.A.**345**, 401 (1975).

[27] S.J.Peppiatt and J.R.Sambles, Proc.R.Soc.Lond.A.**345**, 387 (1975).

[28] R.H.Willens, A.Kornbilt, L.R. Testardi and S. Nakahara, Phys. Rev. B **25**, 290 (1982).

[29] G.Devaud and R.H.Willens,Phys. Rev. Lett. **57**, 2683, (1986).

[30] J.W.M. Frenken and J.F. van der Veen, Phys. Rev. Lett. **54**, 134 (1985).

[31] T.B.Massalski,*Binary Alloy Phase Diagrams*, vol. 2 (American Soc. Metals, (1986).

[32] D.Turnbull, J.S.C.Jang and C.C.Koch,J.Mater.Res.,**5**,1731 (1990).

[33] A.W.Ewald, J.Appl.Phys.,**22**,1436 (1954).

[34] H.Hochst, M.A.Engelhardt and I.Hernandez-Calderon, Phys. Rev. B **40**,9703 (1989).

[35] J.Olajos, P.Vogl, W.Wegscheider and G.Abstreiter, Phys. Rev. Lett. **67**, 3164 (1991).

[36] P.R.Pukite, Alex Harwitt and S.S.Iyer, Appl. Phys. Lett. **54**, 2142 (1989).

[37] R.C.Bowman, Jr., P.M.Adams, M.A.Engelhardt and H.Hochst, J.Vac.Sci.Technol. **A 8**, 1577 (1990).

[38] M.T.Asom, E.A.Fitzgerald, A.R.Kortan, B.Spear and L.C.Kimerling, Appl. Phys. Lett. **55**, 578 (1989).

[39] C.A.Hoffman, J.R.Meyer, R.J.Wagner, F.J.Bartoli, M.A.Engelhardt and H.Hochst, Phys. Rev. B **40**, 11693 (1989).

[40] Jian Zi, Kaiming Zhang and Xide Xie, Phys. Rev. B. **45**, 8397 (1992).

[41] L.G.Parratt, Phys.Rev.**95**,359 (1954)

[42] H.Chen, Ph.D Thesis, City University of New York (1989).

[43] S.M.Heald, H.Chen, and J.M.Tranquada, Phys. Rev. B **38**, 1016 (1988).

[44] H.Chen and S.M.Heald, J. Appl. Phys. **66**, 1793 (1989).

[45] B.Vidal and P.Vincent, Appl. Opt. **23**, 1794 (1984).

[46] D.E.Sayers, E.A.Stern and F.W.Lytle, Phys. Rev. B **27**, 1204 (1971).

[47] E.A.Stern, Phys. Rev. B **10**, 3027 (1974).

[48] P.A.Lee and J.B.Pendry Phys. Rev. B **11**, 2795 (1975).

[49] E.A.Stern, D.E.Sayers and F.W.Lytle, Phys. Rev. B **11**, 4836 (1975).

[50] C.A.Ashley and S.Doniach, Phys. Rev. B **11**, 1279 (1975).

[51] E.A.Stern,B.A.Bunker and S.M.Heald, Phys. Rev. B **21**, 5521 (1980).

[52] J Mustre,Y.Yacoby,E.A.Stern and J.J.Rehr, Phys. Rev. B **42**, 10843 (1990).

[53] E.A.Stern, in *X-ray Absorption: Principles, Applications, Techniques of EXAFS, SEXAFS, XANES,* edited by R.Prinz and D.Koningsberger, (Wiley, New York, 1987).

[54] S.M.Heald and J.M.Tranquada, in *Physical Methods of Chemistry*, edited by B.W.Rossiter,J.F.Hamilton, and R.C.Baetzold, (John Wiley & Sons, New York 1989).

[55] L.I.Shiff, in *Quantum Mechanics*, (McGraw-Hill, New York, 1969).

[56] D.E.Sayers, S.M.Heald, M.A.Pick, J.I.Budnick, E.A.Stern and J.Wong, Nucl. Instrum. and Methods **208**, 631 (1983).

[57] S.M.Heald, in *X-ray Absorption: Principles, Applications, Techniques of EXAFS, SEXAFS, XANES,* edited by R.Prinz and D.Koningsberger, (Wiley, New York, 1987).

[58] Z.Tan, J.I.Budnick and S.M.Heald, Rev. Sci. Instrum. **60**, 1021 (1989).

[59] D.M.Pease, D.E.Brewe, Z.Tan, J.I.Budnick, and C.Law, Phys. Lett. A **138**, 230 (1989).

[60] G.Martens and P.Rabe, Phys. Status Solidi, **58**, 415 (1980).

[61] R.Fox and S.J.Gurman, J. Phys. C, **13**, L249 (1980).

[62] S.M.Heald, J.K.D. Jayanetti and R.C.Budhani, in *Evolution of Thin Films and Surface Microstructure*, edited by C.V.Thompson, T.Y. Tsao, and D.J.Srolovitz, MRS Symposium Proceedings No. 202 (Materials Research Society, Pittsburgh, 1991).

[63] Z.Tan, S.M.Heald, M.Rapposch, C.E.Bouldin, and J.C.Woicik, Phys. Rev. B **46**, 9505 (1992).

[64] E.Chason, T.M.Mayer, A.Payne, and D.Wu, Appl. Phys. Lett. **60**, 2354 (1992).

[65] C.R.Helms, J. Vac. Sci. Technol. **16**, 608 (1979).

[66] P.O.Hahn and M.Henzler, J.Appl.Phys. **54**, 6492 (1983).

[67] P.O.Hahn, S.Yokohama, and M.Henzler, Surf. Sci. **142**, 545 (1985)

[68] D.E.Aspens and J.B.Theeten, J. Electrochem. Soc. **127**, 1359 (1980).

[69] N.M.Ravindra, J.Narayan, D.Fathy, J.K.Srivastava, and E.A.Irene, J. Mater. Res. **2**, 216 (1987).

[70] A.Ourmazd, D.W.taylor, J.A.Rentschler, and J.Bevk, Phys. Rev. lett. **59**, 213 (1987).

[71] A.Ourmazd, J.A.Rentschler, and J.Bevk, Appl. Phys. Lett. **53**, 743 (1988).

[72] F.J.Grunthaner, P.J.Grunthaner, R.P.Vasquez, B.F.Lewis, J.Maserjian, and A.Madhukar, J. Vac. Sci. Technol. **16**, 1443 (1979).

[73] G.Hollinger, E.Bergignat, H.Chermette, F.Himpsel, D.Lohez, M.Lannoo, and M.Bensoussan, Philos. Mag. B **55**, 735 (1987).

[74] P.J.Grunthaner, M.H.Hecht, F.J.Grunthaner, and N.M.Johnson, J. Appl. Phys. **61**, 629 (1987).

[75] F.J.Himpsel, F.R.McFeely, A.Taleb-Ibrahimi, J.A.Yarmoff, and G.Hollinger, Phys. Rev. B **38**, 6084 (1988).

[76] C.Balasingh, A.Abuhasan, and P.K.Predecki, Powder Diffraction, **6**, 16 (1991).

[77] T.H.DeKeijser, J.I.Langford, E.J.Mittemeijer, and A.P.B. Vogels, J. Appl. Crystallogr. **15**, 308 (1982).

[78] C. Kittel, *Introduction to Solid State Physics*, 6th. ed. (John Wiley & Sons, New York, 1986).

[79] W.H.McMaster, N.Kerr Del Grande, J.H.Mallett, and J.H.Hubbell, *Compilation of X-ray Cross Sections*, (National Technical Information Service, Springfield, VA, 1969).

[80] J.K.D.S.Jayanetti, S.M.Heald, and Z.tan, in *Structure & Properties of Interfaces in Materials*, edited by W.A.T.Clark, C.L.Briant, U.Dahman, MRS Symposiam Proceedings, No. 238 (MRS, Pittsburgh, 1992).

[81] E.Sevillano, H.Meuth, and J.J Rehr, Phys. Rev. B **20**, 4908 (1979).

[82] B.A.Bunker, Ph.D. Thesis, University of Washington, (1980).

[83] Einstein temperatures, Θ_E, for the given semiconductors were determined using the experimentally obtained EXAFS Debye-Waller factors, reported in [84].

[84] P.Boolchand and C.C.Koch, J. Mater. Res. **7**, 2876 (1992).

[85] S.M.Heald, S.Jayanetti and K.I.Pandya, Jpn. J. Appl. Phys. (in press).